

NASA/CR-2011-217057



Development and Validation of a Multidisciplinary Tool for Accurate and Efficient Rotorcraft Noise Prediction (MUTE)

*Yi Liu, Phuriwat Anusonti-Inthra, and Boris Diskin
National Institute of Aerospace, Hampton, Virginia*

February 2011

NASA STI Program . . . in Profile

Since its founding, NASA has been dedicated to the advancement of aeronautics and space science. The NASA scientific and technical information (STI) program plays a key part in helping NASA maintain this important role.

The NASA STI program operates under the auspices of the Agency Chief Information Officer. It collects, organizes, provides for archiving, and disseminates NASA's STI. The NASA STI program provides access to the NASA Aeronautics and Space Database and its public interface, the NASA Technical Report Server, thus providing one of the largest collections of aeronautical and space science STI in the world. Results are published in both non-NASA channels and by NASA in the NASA STI Report Series, which includes the following report types:

- **TECHNICAL PUBLICATION.** Reports of completed research or a major significant phase of research that present the results of NASA programs and include extensive data or theoretical analysis. Includes compilations of significant scientific and technical data and information deemed to be of continuing reference value. NASA counterpart of peer-reviewed formal professional papers, but having less stringent limitations on manuscript length and extent of graphic presentations.
- **TECHNICAL MEMORANDUM.** Scientific and technical findings that are preliminary or of specialized interest, e.g., quick release reports, working papers, and bibliographies that contain minimal annotation. Does not contain extensive analysis.
- **CONTRACTOR REPORT.** Scientific and technical findings by NASA-sponsored contractors and grantees.
- **CONFERENCE PUBLICATION.** Collected papers from scientific and technical conferences, symposia, seminars, or other meetings sponsored or co-sponsored by NASA.
- **SPECIAL PUBLICATION.** Scientific, technical, or historical information from NASA programs, projects, and missions, often concerned with subjects having substantial public interest.
- **TECHNICAL TRANSLATION.** English-language translations of foreign scientific and technical material pertinent to NASA's mission.

Specialized services also include creating custom thesauri, building customized databases, and organizing and publishing research results.

For more information about the NASA STI program, see the following:

- Access the NASA STI program home page at <http://www.sti.nasa.gov>
- E-mail your question via the Internet to help@sti.nasa.gov
- Fax your question to the NASA STI Help Desk at 443-757-5803
- Phone the NASA STI Help Desk at 443-757-5802
- Write to:
NASA STI Help Desk
NASA Center for AeroSpace Information
7115 Standard Drive
Hanover, MD 21076-1320

NASA/CR-2011-217057



Development and Validation of a Multidisciplinary Tool for Accurate and Efficient Rotorcraft Noise Prediction (MUTE)

*Yi Liu, Phuriwat Anusonti-Inthra, and Boris Diskin
National Institute of Aerospace, Hampton, Virginia*

National Aeronautics and
Space Administration

Langley Research Center
Hampton, Virginia 23681-2199

Prepared for Langley Research Center
under Contract NNL07AA31C

February 2011

Available from:

NASA Center for AeroSpace Information
7115 Standard Drive
Hanover, MD 21076-1320
443-757-5802

Abstract

A physics-based, systematically coupled, multidisciplinary prediction tool (MUTE) for rotorcraft noise was developed and validated with a wide range of flight configurations and conditions. MUTE is an aggregation of multidisciplinary computational tools that accurately and efficiently model the physics of the source of rotorcraft noise, and predict the noise at far-field observer locations. It uses systematic coupling approaches among multiple disciplines including Computational Fluid Dynamics (CFD), Computational Structural Dynamics (CSD), and high-fidelity acoustics. Within MUTE, advanced high-order CFD tools are used around the rotor blade to predict the transonic flow (shock wave) effects, which generate the high-speed impulsive noise. Predictions of the blade-vortex interaction noise in low speed flight are also improved by using the Particle Vortex Transport Method (PVTM), which preserves the wake flow details required for blade/wake and fuselage/wake interactions. The accuracy of the source noise prediction is further improved by utilizing a coupling approach between CFD and CSD, so that the effects of key structural dynamics, elastic blade deformations, and trim solutions are correctly represented in the analysis. The blade loading information and/or the flow field parameters around the rotor blade predicted by the CFD/CSD coupling approach are used to predict the acoustic signatures at far-field observer locations with a high-fidelity noise propagation code (WOPWOP3). The predicted results from the MUTE tool for rotor blade aerodynamic loading and far-field acoustic signatures are compared and validated with a variation of experimental data sets, such as UH60-A data, DNW test data and HART II test data.

Table of Contents

Lists of Figures	IV
Abbreviations	VIII
Acknowledgements	IX
Chapter I Introduction and Background	1
Chapter II CFD Coupled with CSD for Accurate Noise Prediction	4
2.1 CFD and CSD Coupling Procedure	4
2.2 Rotorcraft Wake Capturing/Modeling Method Studies	6
2.3 High-order Near-Blade CFD Algorithm Studies	21
2.4 CFD/CSD Coupled Method for DNW High-speed Noise Predictions	26
2.5 Simulations for HART Baseline Low-speed BVI Case.....	28
Chapter III Particle Vortex Transport Method for Accurate Wake Modeling.....	31
3.1 UH60 Simulations Using Coupled CII/TURNS/PVTM Method	32
3.2 HART II Simulations Using Coupled CII/TURNS/PVTM Method	39
Chapter IV Improved and Efficient Interfaces with Acoustic Propagation Codes	45
4.1 DNW High-speed Noise Prediction.....	46
4.2 HART II BVI Noise Prediction	54
Chapter V Concluding Remarks	58
References	60

List of Figures

Figure 1.1: MUTE Tool Structure	1
Figure 2.1: CFD/CSD Coupling Procedures between TURNS/Free-Wake and CII	5
Figure 2.2: Overset Grid (near body grid + background grid).....	7
Figure 2.3: CFD+Overset Grid Method: Convergence History (c8534)	8
Figure 2.4: CFD+Overset Grid Method: Uh60-A High-speed case (c8534) Total Normal Force Comparisons.....	9
Figure 2.5: CFD+Overset Grid Method: Uh60-A High-speed case (c8534) Pitch Moment Comparisons.....	9
Figure 2.6: CFD+Overset Grid Method: Uh60-A Low-speed case (c8513) Convergence History	10
Figure 2.7: CFD+Overset Grid Method: Uh60-A Low-speed case (c8513) Total Normal Force Comparison	11
Figure 2.8: CFD+Overset Grid Method: Uh60-A Low-speed case (c8513) Pitch Moment Comparisons	11
Figure 2.9: CFD+Overset Grid Method: Uh60-A Dynamic Stall Case (c9017) Convergence History	12
Figure 2.10: CFD+Overset Grid Method: Uh60-A Dynamic Stall Case (c9017) Total Normal Force Comparisons	13
Figure 2.11: CFD+Overset Grid Method: Uh60-A Dynamic Stall Case (c9017) Pitch Moment Comparisons	13

Figure 2.12: CFD+Free-Wake Method: Convergence History (c8534)	16
Figure 2.13: CFD+Free-Wake Method:	
Normal Force and Pitch Moment Comparison at $r/R = 55\%$ (c8534)	16
Figure 2.14: CFD+Free-Wake Method:	
Normal Force and Pitch Moment Comparison at $r/R = 96.5\%$ (c8534)	17
Figure 2.15: CFD+Free-Wake Method: Convergence History (c8513)	18
Figure 2.16: CFD+Free-Wake Method:	
Normal Force and Pitch Moment Comparison at $r/R = 55\%$ (c8513)	18
Figure 2.17: CFD+Free-Wake Method:	
Normal Force and Pitch Moment Comparison at $r/R = 96.5\%$ (c8513)	19
Figure 2.18: CFD+Free-Wake Method: Convergence History (c9017)	20
Figure 2.19: CFD+Free-Wake Method:	
Normal Force and Pitch Moment Comparison at $r/R = 55\%$ (c9017)	20
Figure 2.20: CFD+Free-Wake Method:	
Normal Force and Pitch Moment Comparison at $r/R = 96.5\%$ (c9017)	21
Figure 2.21: High-Order CFD Scheme provides sufficient spatial and temporal accuracy .	21
Figure 2.22: Normal Force and Pitch Moment Comparison (High-order scheme 55%)	24
Figure 2.23: Normal Force and Pitch Moment Comparison (High-order scheme 96.5%) ...	25
Figure 2.24: The Overset Grid for DNW High-Speed Simulations.....	26
Figure 2.25: The Convergence History for DNW High-speed Case	27
Figure 2.26: Normal Force and Pitch Moment Comparison at $r/R = 55\%$ (DNW).....	27
Figure 2.27: Normal Force and Pitch Moment Comparison at $r/R = 96.5\%$ (DNW).....	28
Figure 2.28: The Convergence History for HART II Low-Speed Case	29

Figure 2.29: The Blade Loading Comparison at 87% Span for HART II Case	29
Figure 2.30: The CFD+Free-wake Method Grid	30
Figure 2.31: The CFD+Free-wake Blade Loading Predictions for HART II Case	30
Figure 3.1: Gridless PVTM prescribes and preserves evolution of wake from rotor system	31
Figure 3.2: UH60 Blade Grid for Near Body CFD Calculation	33
Figure 3.3: (a) UH60 Blade Profiles and (b) Blade Twist Distribution.....	33
Figure 3.4: Schematic of PVTM Grid with Multi-resolution Zones for c8534.....	34
Figure 3.5: Convergence History for Rotor Trim Parameters (UH60A c8534)	34
Figure 3.6: Convergence History for Rotor Thrust (UH60A c8534).....	34
Figure 3.7: Normal Force Comparison (UH60A c8534).....	35
Figure 3.8: Converged Vorticity Field (UH60A c8534).....	36
Figure 3.9: Convergence History of Thrust and Trim Parameters (UH60A c8513)	36
Figure 3.10: Comparison of Normal Force (UH60A c8513).....	37
Figure 3.11: Comparisons of Normal Forces (UH60A c8513).....	38
Figure 3.12: Converged Vorticity Field (UH60A c8513).....	38
Figure 3.13: HART II Blade Grid.....	40
Figure 3.14: HART II Blade Twist Profile	40
Figure 3.15: Trim Convergence History (HART II: BL, low resolution)	40
Figure 3.16: Comparison of Blade Normal Force (HART II: BL, low Res.).....	41
Figure 3.17: Comparison of Blade Normal Force at $r/R = 0.87$ (HART II: BL, low res)	41
Figure 3.18: Converged Vorticity Field (HART II: BL, low res).....	42
Figure 3.19: Schematic of PVTM grid with Multi-resolution zones	42
Figure 3.20: Trim Convergence History (HART II: BL, high resolution)	42

Figure 3.21: Comparison of Blade Normal Force (HART II: BL, high res.)	43
Figure 3.22: Comparison of Blade Normal Force at $r/R = 0.87$	43
Figure 3.23: Comparison of Blade Normal Force	44
Figure 3.24: Comparison of Blade Normal Force	44
Figure 4.1: Noise Propagation from the Rotorcraft to Observer Locations.....	45
Figure 4.2: The Acoustic Experimental Set-up for DNW High-speed Case	46
Figure 4.3: The Sound Pressure of Microphone 1	47
Figure 4.4: The Sound Pressure of Microphone 7	47
Figure 4.5: The Sound Pressure Comparison for Microphone 1 (Impermeable Surface)	49
Figure 4.6: The Sound Pressure Comparison for Microphone 7 (Impermeable Surface)	49
Figure 4.7: The Sound Pressure Comparison for Microphone 1 (Pressure Surface).....	50
Figure 4.8: The Sound Pressure Comparison for Microphone 7 (Pressure Surface).....	50
Figure 4.9: Acoustic Data Surface (BL surface vs. Grid 1).....	51
Figure 4.10: Acoustic Data Surface (BL surface vs. Grid 2).....	51
Figure 4.11: Acoustic Data Surface (BL surface vs. Grid 3).....	52
Figure 4.12: WOPWOP3 Predictions for Different Acoustic Data Surface Grids	52
Figure 4.13: The Sound Pressure Comparison for Microphone 1	53
Figure 4.14: The Sound Pressure Comparison for Microphone 7	53
Figure 4.15: Experiment BVI SPL Contour (HART II BL Case)	55
Figure 4.16: BVI SPL Contour with CFD+Overset Grid Method.....	55
Figure 4.17: BVI SPL Contour with CFD+Free-wake Method.....	56
Figure 4.18: BVI SPL Contour with CFD+PVTM Low Resolution Wake Method	56
Figure 4.19: BVI SPL Contour Comparisons with PVTM Method	57

Abbreviations

2D	Two Dimensional
3D	Three Dimensional
ADS	Acoustic Data Surface
ARL	Army Research Laboratory
BVI	Blade Vortex Interaction
CAMRAD	Comprehensive Analytical Model of Rotorcraft Aerodynamics and Dynamics
CII	CAMRAD II
CFD	Computational Fluid Dynamics
CSD	Computational Structure Dynamics
DLR	German Aerospace Center
HART	Higher Harmonic Control Aero-acoustic Rotor Test
NASA	National Aeronautics and Space Administration
NIA	National Institute of Aerospace
PVTM	Particle Vortex Transport Method
RANS	Reynolds Averaged Navier-Stokes
VTM	Vortex Transport Method

Acknowledgements

The financial support for this research from the NASA Fundamental Aeronautic Program Subsonic Rotary Wing Project under Contract NNL07AA31C, with Dr. Doug Nark as a technical monitor, is gratefully acknowledged. The authors are also grateful for the financial support for the initial investigation prior to this research at NIA from another NASA contract NAS1-2117, Task Order NNL04AA96T (Rotorcraft Aeromechanics), with Dr. Mark Nixon (ARL) as a technical monitor.

The authors would like thank Dr. Doug Nark, Dr. Ken Brentner, Ms. Casey Burley, Dr. Doug Boyd, Dr. Jayanarayanan Sitaraman, and Dr. Wayne Johnson for their valuable technical guidance, support and suggestions.

Chapter I

Introduction & Background

MUTE is a systematic combination of multidisciplinary analysis tools that accurately and efficiently models the physics of the source of the rotorcraft noise, and predicts the noise at far-field observer locations. MUTE uses a systematic coupling approach among multiple disciplines including Computational Fluid Dynamics (CFD) with high-fidelity wake modeling, Computational Structural Dynamics (CSD), and high-fidelity acoustics. Figure 1.1 illustrates MUTE with its multidisciplinary analysis tools.

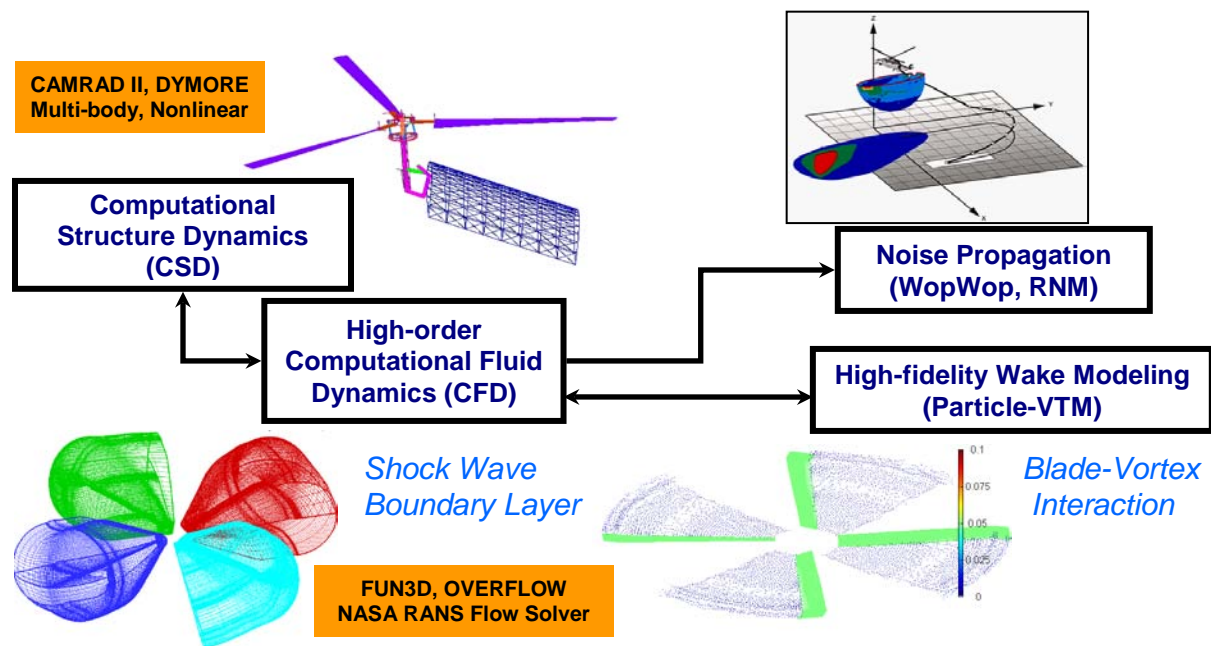
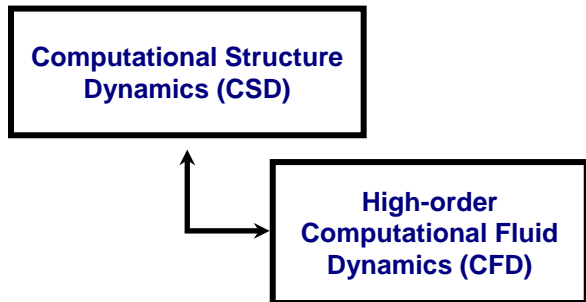


Figure 1.1: MUTE uses a systematic coupling approach among multiple disciplines, to accurately and efficiently predict rotorcraft noise.

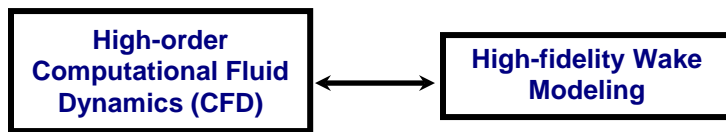
The objective of developing the MUTE tool is to accurately model the physics of the noise source, and to understand the basis of the noise generation from rotorcraft in a wide range of flight regimes. Within MUTE, advanced high-order CFD tools are used around the rotor blade to predict the transonic flow (shock wave) effects, which generate the high-speed impulsive noise. Predictions of the blade-vortex interaction noise in low speed flight are also

improved by using the Particle Vortex Transport Method (PVTM), which preserves the wake flow details required for blade/wake and fuselage/wake interactions. The accuracy of the source noise prediction is further improved by utilizing a coupling approach between CFD and CSD, so that the effects of key structural dynamics, elastic blade deformations, and trim solutions are correctly represented in the analysis.

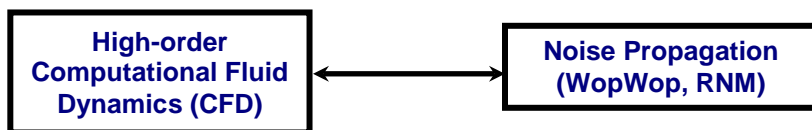
To efficiently and successfully develop the MUTE tool, the project was divided into 3 major tasks. Within each of them, an essential element of the MUTE tool was developed and validated during the first two years. The integration of these elements and the validation of the whole MUTE tool were undertaken in the third year of the project.



The purpose of the first task (task 1) was to develop high order near blade CFD algorithms coupled with CSD for accurate source noise prediction. In this task, the effect of high-order CFD algorithms on the prediction of rotor blade loading was investigated. The effect of conventional wake modeling/capturing methods, such as free-wake and CFD with overset-grid methods, on the prediction of rotor blade loading were also studied and compared with the new PVTM method.



The second task (task 2) was to apply and validate the Particle Vortex Transport Method (PVTM) for accurate wake modeling. In this task, predictions from the PVTM method developed by the Co-I were compared with the UH60-a blade loading test data, and the BVI loading data from the HART II test.



The purpose of the final task (task 3) was to develop an improved and efficient interface

with the acoustic propagation code (WOPWOP 3). A python based control script was developed

to control the coupling processes among CFD, CSD and WOPWOP 3. For acoustic predictions, both permeable surface and impermeable surface methods were implemented in the coupling process. The acoustic prediction results were compared with the DNW high-speed test case, and the HART II BVI noise case.

Chapter II

CFD Coupled with CSD for Accurate Source Noise Prediction

2.1 Computational Fluid Dynamics (CFD) / Computational Structural Dynamics (CSD) Coupling Procedure

Aerodynamic/structural analysis of helicopter rotors is a challenging problem that requires multidisciplinary methods to predict the rotor performance. In general, a finite element computational structural dynamics (CSD) analysis can predict blade motions and structural dynamics accurately if correct surface aerodynamic loadings are provided. However, due to the overwhelming complexity of the comprehensive analysis, the aerodynamic components inside a CSD analysis are based on lower-order lifting line theory with wake/inflow models and two-dimensional airfoil tables. These cannot physically model some complicated phenomena such as unsteady, three-dimensional viscous flow-fields, transonic flow with shocks, reverse flow and dynamic stall. On the other hand, computational fluid dynamics (CFD) analysis will provide high fidelity, nonlinear aerodynamics if the elastic rotor motions can be obtained from a CSD analysis. Thus, combining CFD and CSD as a systematic rotorcraft analysis tool is getting more and more attention.

Coupling between CFD and CSD can be accomplished in two ways. The first method is loose (weak) coupling methodology, where information is transferred on a one per revolution, periodic basis between CFD and CSD. The second is tight (strong) coupling, where the CFD and CSD are coupled at every time step and marched forward in time simultaneously. Although tight coupling is more rigorous and can solve both steady and unsteady problems, the choice of algorithm is not trivial and many issues have to be carefully considered. On the other hand, the loose coupling approach is more mature and has been widely used in predicting blade loadings at different steady flight conditions.

Currently, a Reynolds averaged Navier-Stokes CFD code (TURNS) [2.1] and a rotorcraft comprehensive analysis/CSD code (CAMRAD II) [2.2] have been coupled for all of the following simulation results. The loose coupling approach has been used for these validation cases since they are all under steady and periodic flight conditions.

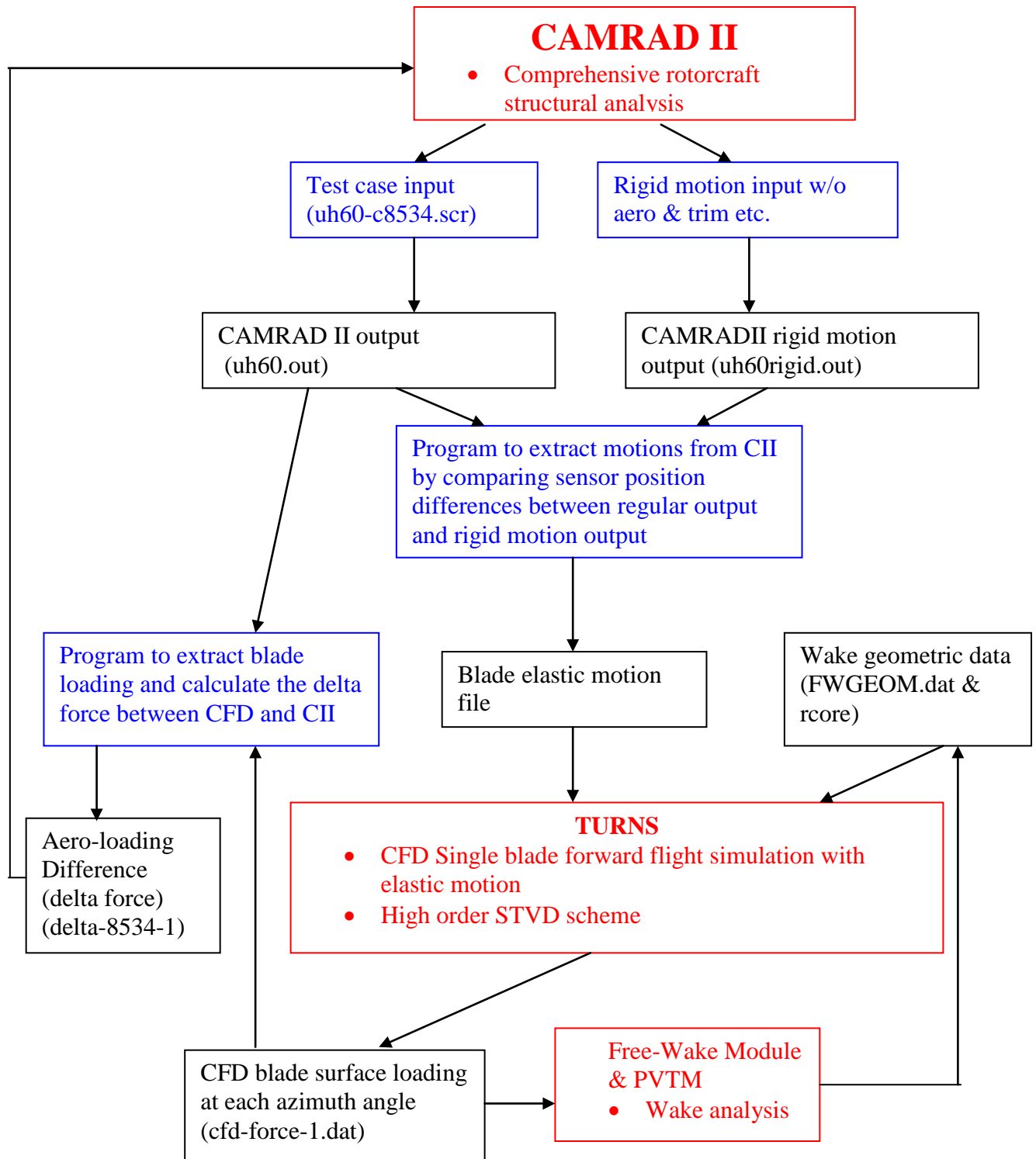


Figure 2.1 CFD/CSD Coupling Procedures between TURNS/Free-Wake and CAMRAD
 (Red Box --- Main CFD, CSD and Wake Analysis Solvers)
 (Blue Box --- Interface codes for CFD/CSE coupling iterations)
 (Black Box --- Data/Information exchanged between these main solvers)

As shown in Figure 2.1, during the coupling procedure, a CAMRAD II blade motion file is first generated with the position of the un-deflected blade quarter chord and the relative displacement of three translations and three rotations of the deflected quarter chord as a function of the radial location and azimuth angle. TURNS reads this file as input, deforms the grid, and computes the results for the next revolution with these motions. To improve convergence, a “delta” method has been used to feed back the loading into CAMRAD II. The blade loading increment, ΔF , is updated from the difference between the CFD loads and the comprehensive analysis calculations,

$$\Delta F_i^{CSD} = \Delta F_{i-1}^{CSD} + (F_{i-1}^{CFD} - F_{i-1}^{CSD}) . \quad (1)$$

In this manner, it is not necessary to separate out the lifting line analysis embedded inside the comprehensive analysis code (CAMRAD II). CAMRAD II uses this delta force file as input for the next iteration. The coupling iterations repeat the above procedure until the predicted loading between two iterations is converged.

2.2 Rotorcraft Wake Capturing/Modeling Methods Studies

For rotorcraft aeromechanics simulation, correctly capturing the wake effects is very important under many flight conditions. Traditionally, there are two ways to capture/model rotorcraft wake effect for CFD simulations. First is the free-wake method, which is based on potential flow theory and is dependent on empirical inputs. The second is the CFD overset grid methodology, where a large background grid is used with CFD to directly capture the wake effect from the blade. This is a physics based, high resolution wake capturing method. However, the results are heavily dependent on the background grid resolution, thus are limited by the available computational resources. Additionally, the numerical dissipation embedded in the algorithm may diffuse the tip vortex too rapidly.

A new Particle Vortex Transport Method (PVTM) [2.3] has been developed under another NRA contract (NNL07AA32C). This is also a physics based high-fidelity wake modeling method, where the incompressible vortex transport equation is solved using a Lagrangian approach.

In task 1, the first two wake capturing/modeling methods, overset grid and free-wake, were investigated and validated with UH60a experimental data to assess the advantages and limitations of these approaches during different flight conditions. Then, the overset grid methodology was applied to the DNW high-speed case and HART II baseline BVI case, to obtain more accurate noise source prediction for further acoustic analysis.

In task 2, the PVTM method was utilized and validated against the same experimental data to assess the model limitations and to improve the accuracy and efficiency of the approach.

2.2.1 CFD with overset grid methodology simulation results and discussions for UH60a high-speed level flight, low-speed level flight and dynamic stall flight conditions

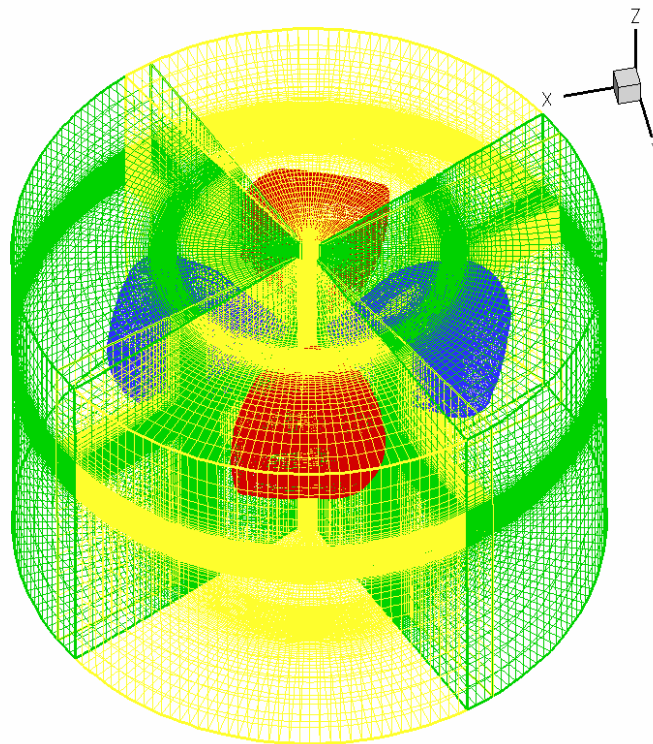


Figure 2.2 Overset Grid (near body grid + background grid)

In the overset grid method, the full grid around the rotor was divided into two parts, a very fine near-body grid to simulate the flowfield around the blade and a large cylindrical background grid to capture the wake effects. The RANS solver was used for both grids, thus this method can provide physics based high-fidelity flow simulations. A typical overset grid used by TURNS is shown in Figure 2.2, where the near-body grid has 3.2 million grid points and the

background grid has 2.2 million grid points. This method is also used by NASA with the OVERFLOW CFD code.

The first set of experimental/flight test data used in this project was for a UH-60A helicopter in level flight. The data were obtained during the NASA/Army UH-60A Airloads program. Currently, the database provides the aerodynamic pressure, rotor forces and moments etc. at 9 span locations $r/R = 0.225, 0.40, 0.55, 0.675, 0.775, 0.865, 0.92, 0.965,$ and 0.99 , for three level flight conditions, allowing for the validation of the aerodynamic models. These three flight conditions are: a high-speed level flight (counter no. 8534) with an advance ratio 0.368 , a low-speed level flight (counter no. 8513) with an advance ratio 0.149 , and a high-thrust dynamic stall flight (counter no. 9017) with an advance ratio 0.237 . The blade loading predictions from CFD with overset grid coupled with CSD are compared with these test data and are discussed in the following sections for all three flight conditions.

2.2.1.1 UH-60A High-speed Level Flight Results and Discussions (c8534)

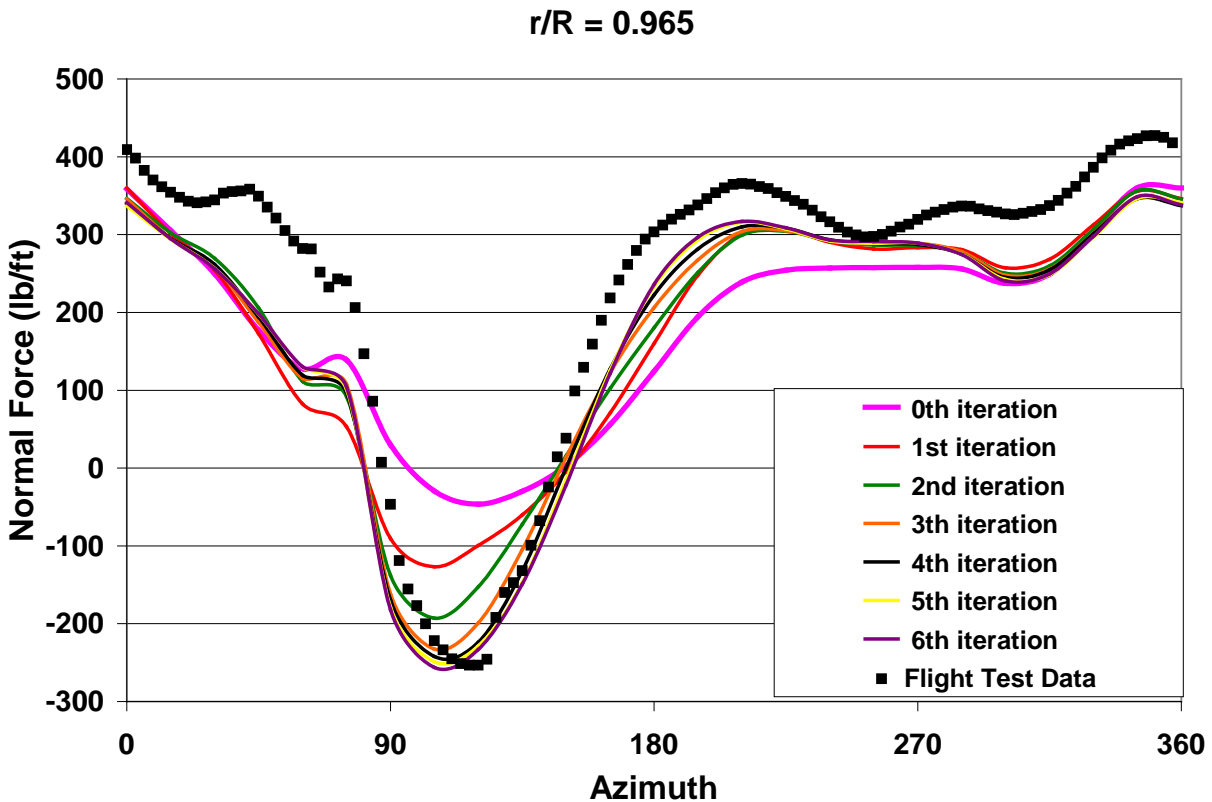


Figure 2.3 Convergence History (Blade Loading Prediction by TURNS at 96.5% Span)

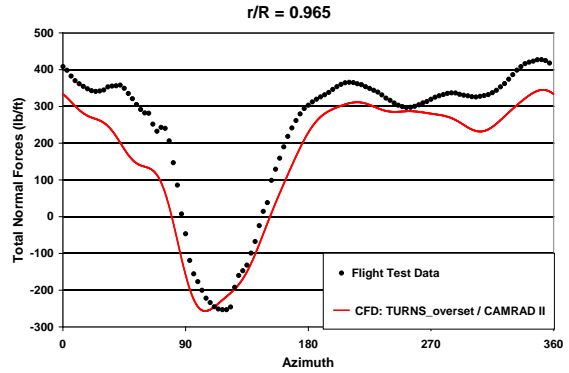
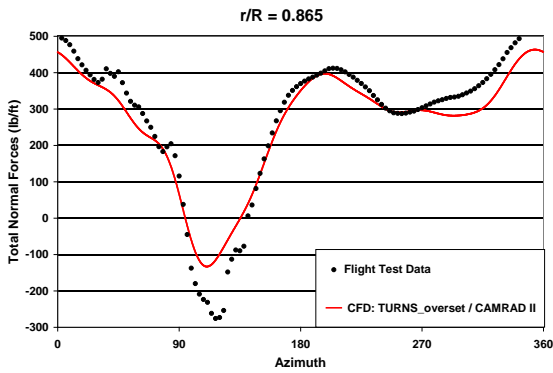
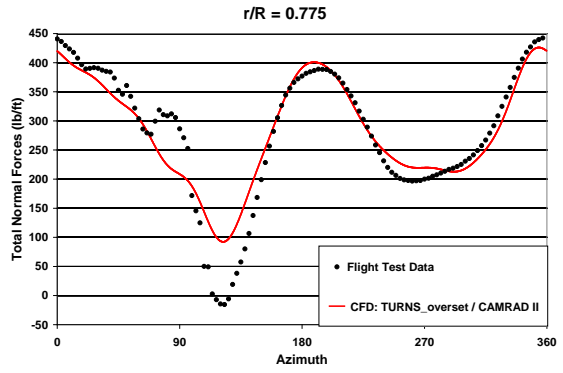
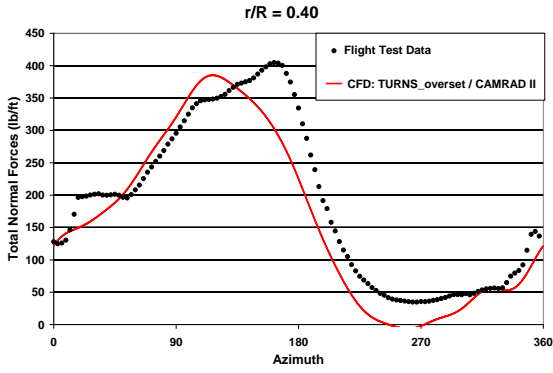


Figure 2.4 Total Normal Force Comparisons with Flight Test Data

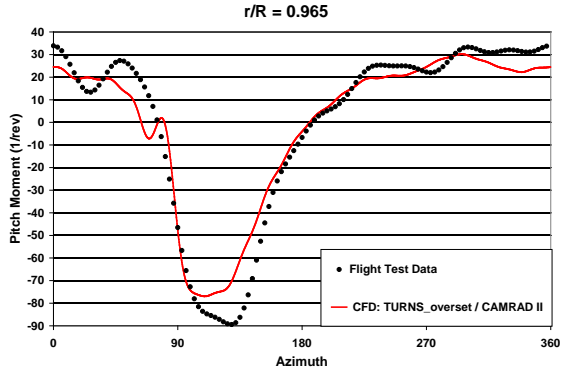
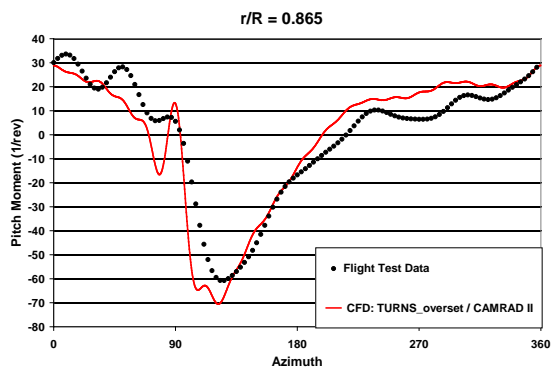
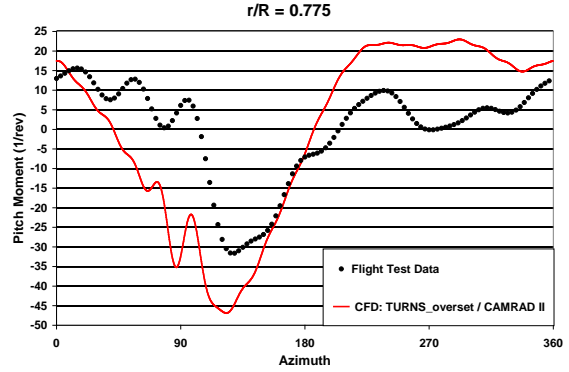
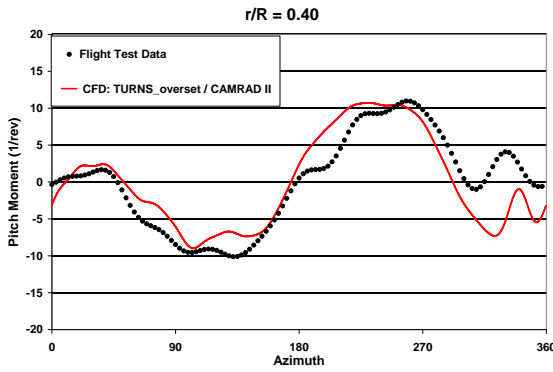


Figure 2.5 Pitch Moment Comparisons with Flight Test Data

For the UH-60A test, flight test counter number 8534, is a high-speed level flight case, where the advance ratio is 0.368. The rotor speed is 258 RPM, with a tip Mach number 0.6415. The trimmed thrust is at $C_T/\sigma = 0.08433$. As shown in Figure 2.3, it takes 7 CFD/CSD coupling iterations to get a converged result for this case. As shown in Figures 2.4 and 2.5, the total normal forces and pitch moments are in good agreement with the flight test data. Especially in the tip region, the near-body CFD solver has accurately captured the transonic flow phenomena and the shock wave interaction at the advancing side. This is important for the improved prediction of these forces and moments in the tip region compared to the comprehensive analysis simulation.

2.2.1.2 UH-60A Low-speed Level Flight Results and Discussions (c8513)

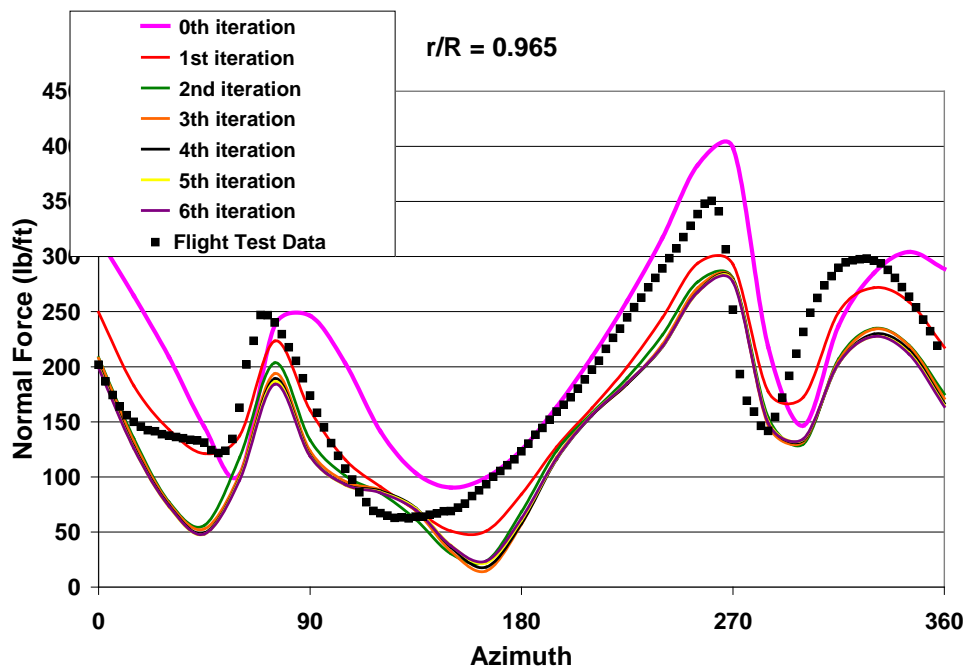


Figure 2.6 Convergence History (Blade Loading Prediction by TURNS at 96.5% Span, c8513)

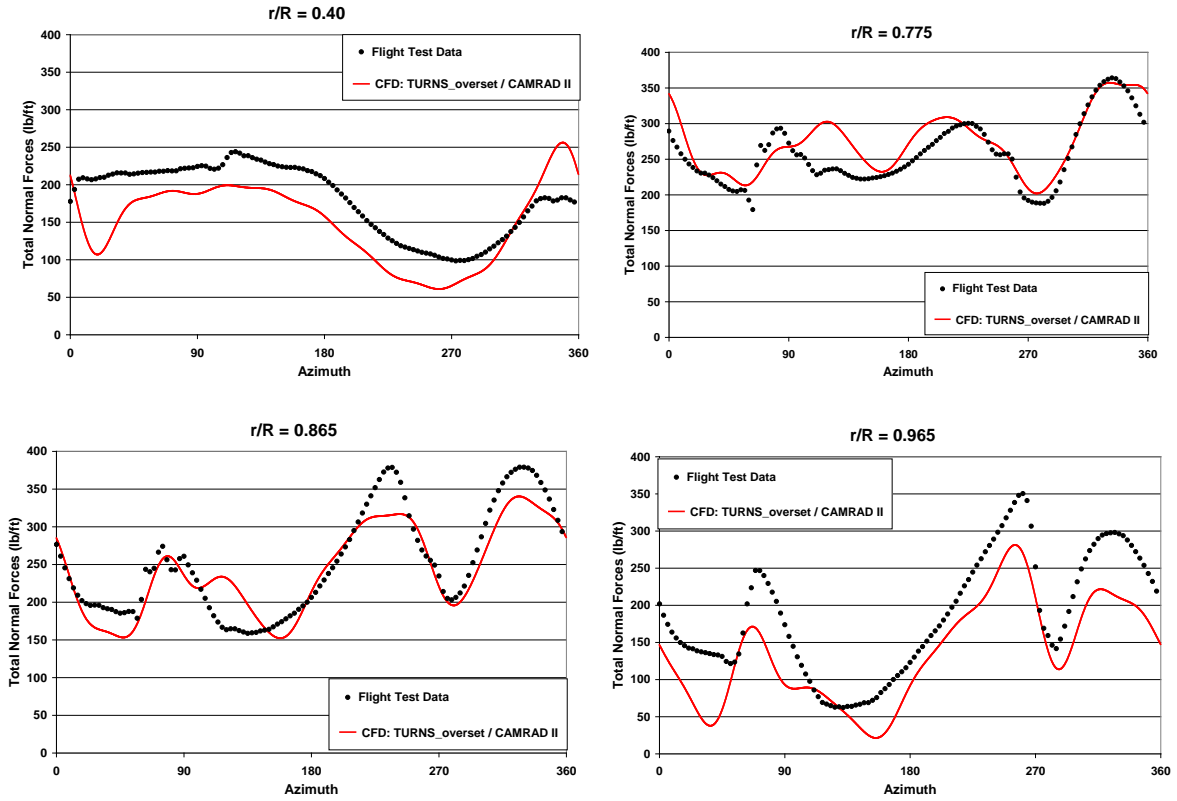


Figure 2.7 Total Normal Force Comparison with Flight Test Data (c8513)

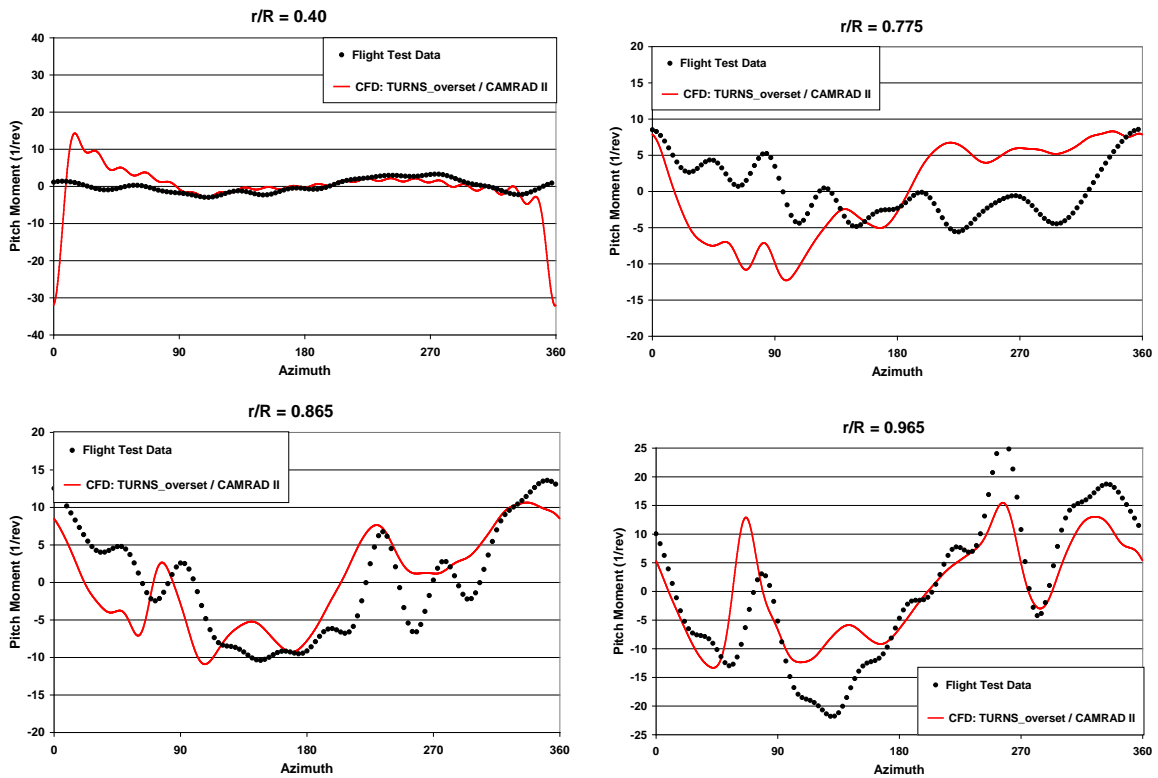


Figure 2.8 Pitch Moment Comparison with Flight Test Data (c8513)

The flight test counter number 8513 is a low-speed level flight case with an advance ratio of 0.149. The rotor speed is also 258 RPM, with a tip Mach number 0.6646. The trimmed thrust is slightly lower than c8534, at $C_T/\sigma = 0.0763$. As shown in Figure 2.6, it also takes 7 CFD/CSD coupling iterations to get a converged result for this case. However, because of the low free-stream velocity, the CFD requires two revolutions per iteration to obtain a periodic solution. In general, the total normal forces and pitch moments are also in good agreement with the experimental data as shown in Figures 2.7 and 2.8. Since this is a low-speed level flight case, the blade vortex interaction is not dominant. It can be seen from the test data that there are no high-frequency BVI effects on the blade loading. However, the tip vortex wake effect from the preceding blade is still represented by low-frequency blade loading variations, which are just fairly predicted by the CFD oversight method. Some of the tip vortex effects from the preceding blade are diffused by the oversight methodology, and improvement of the low-speed CFD predictions was investigated with the PVTM method.

2.2.1.2 UH-60A High-thrust Dynamic Stall Flight Results and Discussions (c9017)

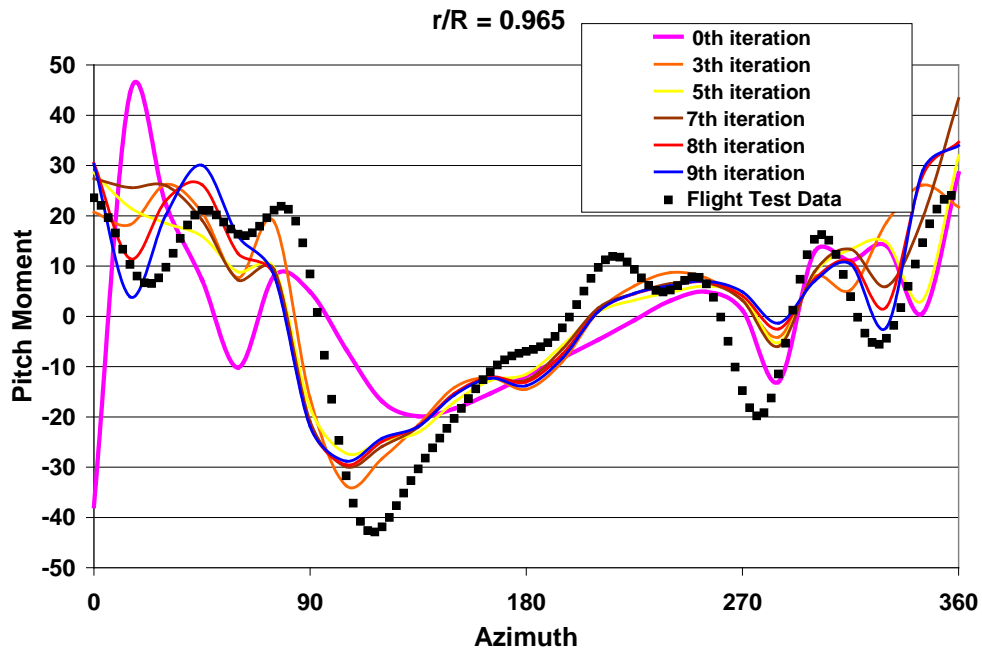


Figure 2.9 Convergence History (Blade Loading Prediction by TURNS at 96.5% Span, c9017)

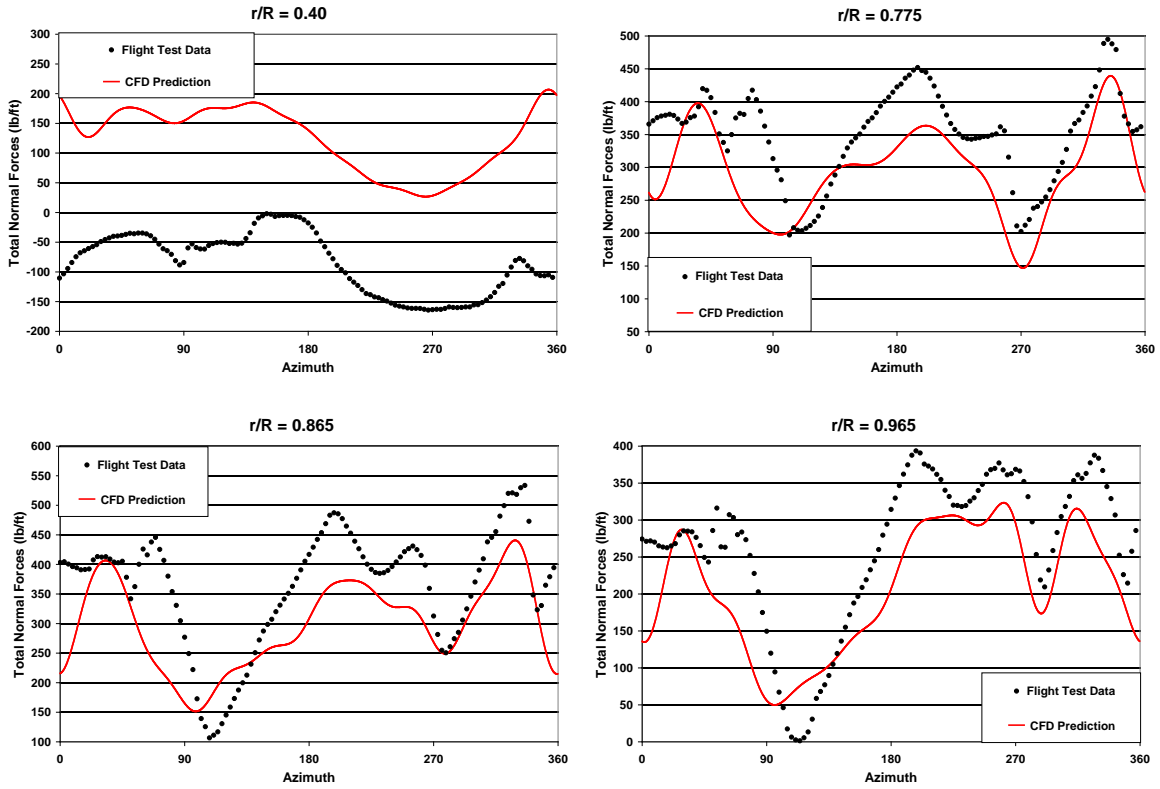


Figure 2.10 Total Normal Force Comparison with Flight Test Data (c9017)

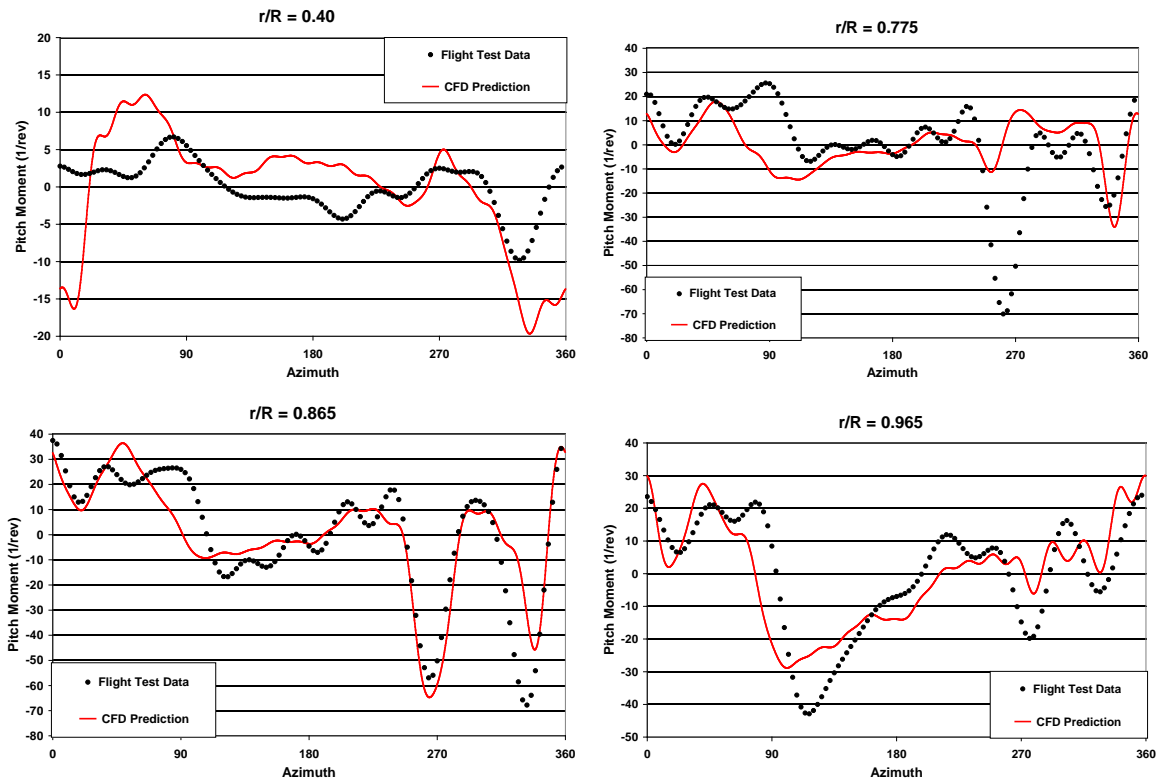


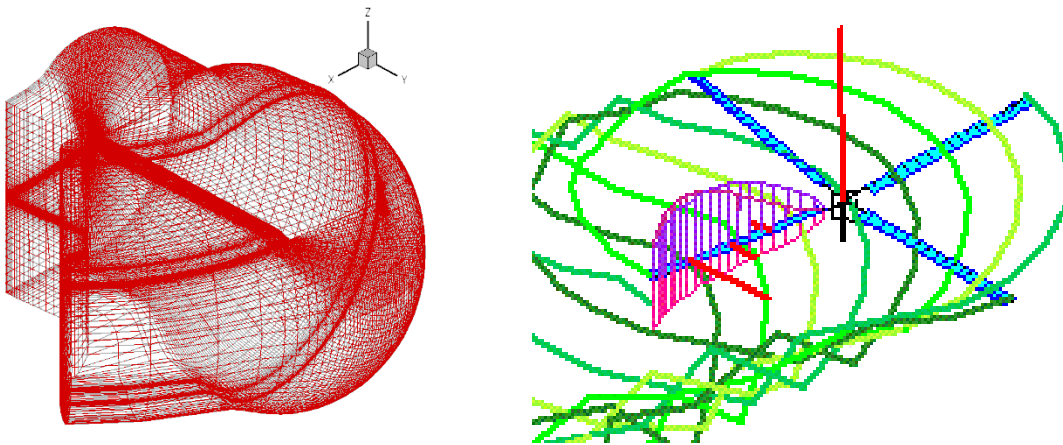
Figure 2.11 Pitch Moment Comparison with Flight Test Data (c9017)

The flight test c9017 is an intermediate speed case with advance ratio of 0.237, high thrust with C_T/σ at 0.129, and level flight test point flown at 17,000 ft. This is a challenging rotorcraft test case due to the wide effects of unsteady flow conditions, especially the dynamic stall effects, with noticeable wake interactions.

As shown in Figure 2.9, it takes 9 iterations to get a fairly converged result for this case. It is difficult to obtain a converged result at the tip region on the retreating side due to the strong unsteady effects from the dynamic stall. As for the forces and moments comparison, as shown in Figures 2.10 and 2.11, reasonable agreement is still reached between the CFD predictions and the flight test data. In Figure 2.10, the total normal forces are matched with the experiment, except at the root region, $r/R = 0.40$, where the rotor hub effects are not simulated by CFD. The low-frequency wake effect from the preceding blade is also captured. In Figure 2.11, it can be seen that the two dynamic stall peaks at the tip region in retreating side are also fairly captured by the CFD. It is essential to have a physics based, high-fidelity solver around the near-blade region to capture such unsteady flow characteristics.

2.2.2 CFD with Free-wake method simulations and validation

The following figure shows the typical approach to employing the CFD+Free-wake method. Here, the CFD solver is used for the near-body grid to accurately capture the physics of flow characteristics around the blade, and a free-wake module is used to get the wake geometry and the wake effect quickly. Then, the wake effect is fed back to the CFD solver using a field-velocity approach. Compared to the other two methods, this method can generate results much faster and has great potential for design purposes.



2.2.2.1 UH-60A High-speed Level Flight (c8534)

The UH-60A high-speed case (c8534) has a large advance ratio of 0.368, so the wake effect will be expected to be small. The following figures show the comparison of blade loading predictions (normal forces and pitch moment) from the CFD+Free-wake method with CFD+Overset grid method and the flight test data.

Figure 2.12 shows the convergence history of the CFD+Free-wake method. For this high-speed case, both methods converge very quickly, requiring only 6 iterations to get a fully converged result. Actually, the CFD+Free-wake method converges even faster than the overset grid method, needing only 3-4 iterations to approach a converged result.

The blade loading predictions are compared in Figures 2.13 and 2.14. It can be seen that the CFD+Free-wake method agrees well with both the overset grid predictions and flight test data. Particularly in the root to in-board region (Figures 2.13), the CFD+Free-wake method gives slightly better predictions than the overset-grid method. This is because the free-wake module has a root-wake component, while the overset grid cannot fully capture the root wake due to the

grid resolution in that region. Around the tip region (Figure 2.14), the CFD+Overset grid method gives a slightly better prediction than the free-wake method. This is due to the fact that the full CFD method captures the physics of the transonic effect better than the free-wake approach.

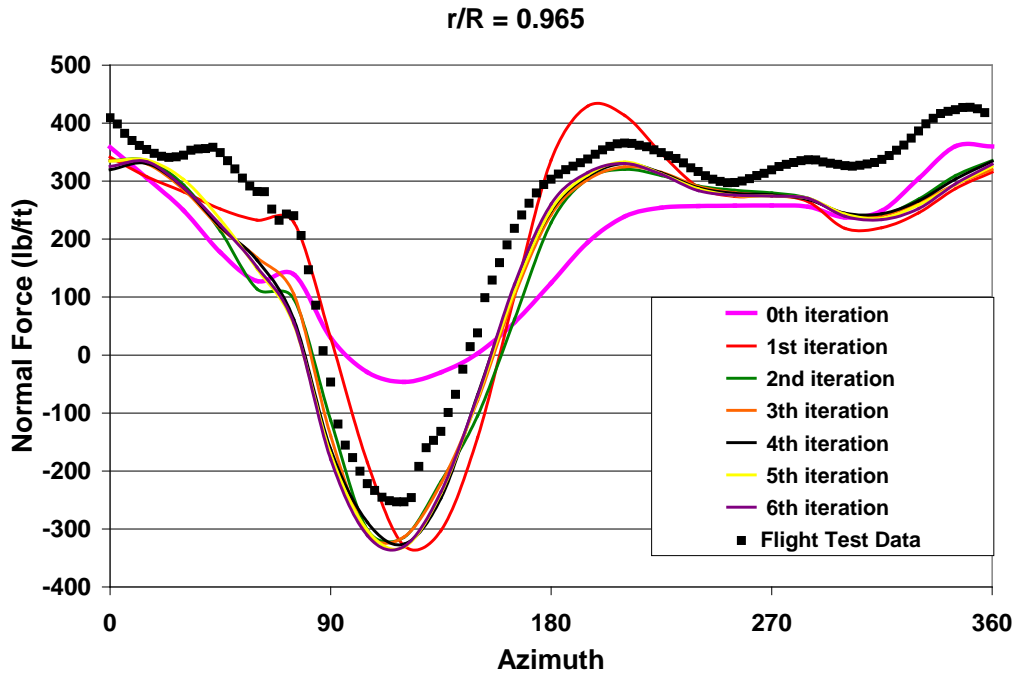


Figure 2.12 Convergence History of CFD+Free-wake
(Blade Loading Prediction by TURNS at 96.5% Span, c8534)

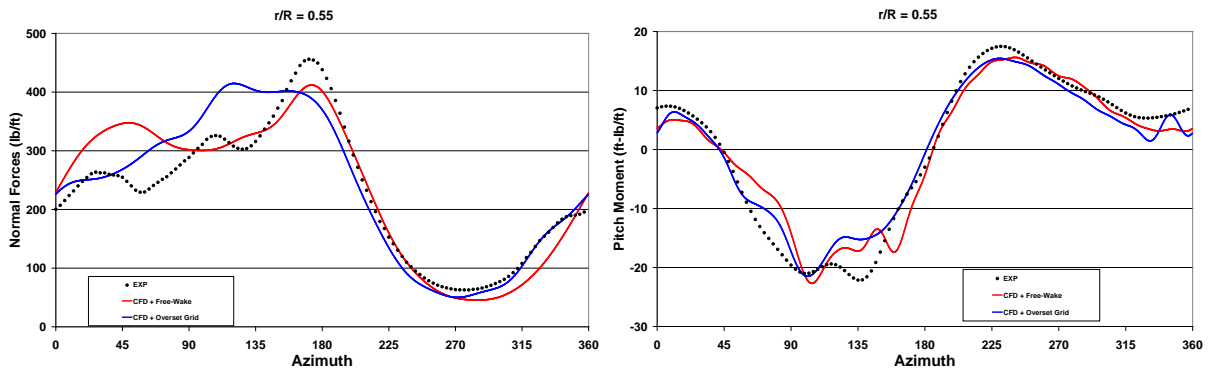


Figure 2.13 Normal Forces and Pitch Moment Comparisons at $r/R = 55\%$ (c8534)

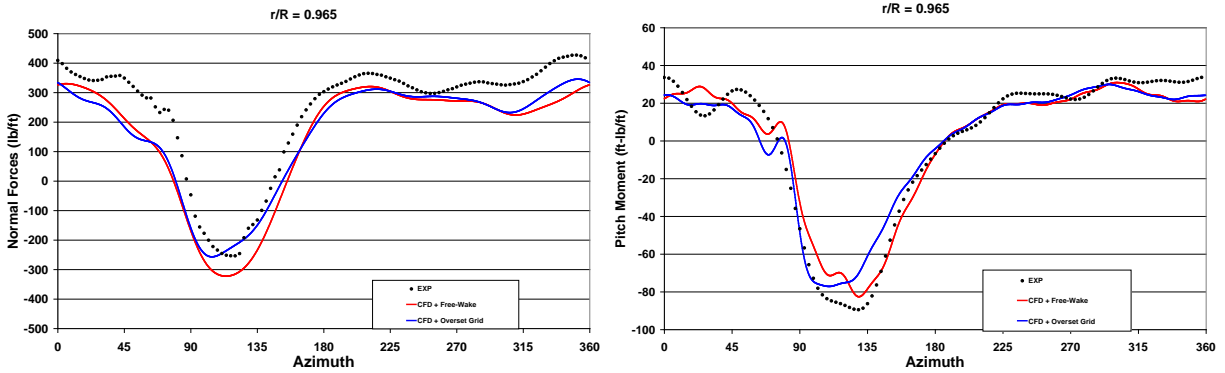


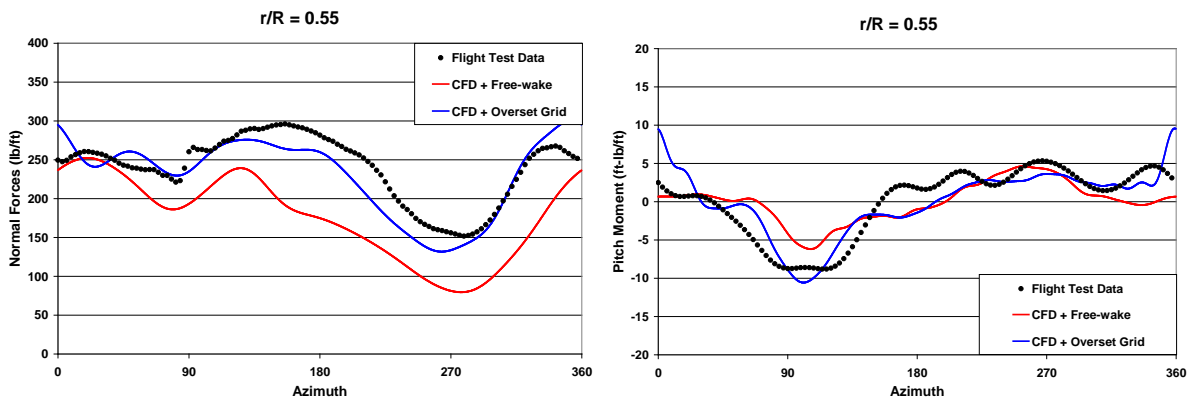
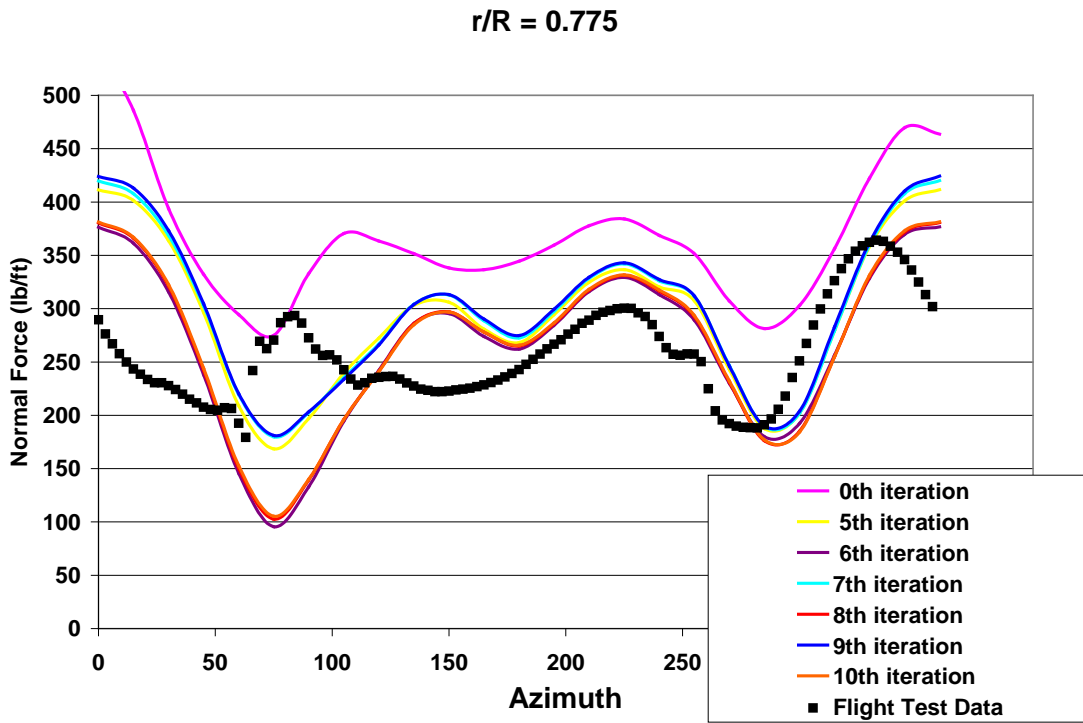
Figure 2.14 Normal Forces and Pitch Moment Comparisons at $r/R = 96.5\%$ (c8534)

2.2.2.2 UH-60A Low-speed Level Flight (c8513)

The UH-60A low-speed case has an advance ratio of 0.149. Since it is a level flight condition, the high-frequency BVI effect is not dominant for this low-speed case, and the force variations are mostly low-frequency.

Figure 2.15 shows the convergence history of the CFD+Free-wake method for this low speed case. It can be seen that for the free-wake method, the CFD/CSD coupling does not converge to a single trimmed value. Eventually, the predictions jump between two values. As shown in the figure, iteration numbers 5, 7, and 9 trend toward the same result, while iteration numbers 6, 8, and 10 converge to another. Thus, the computational results from iteration 9 were selected for the following comparisons since they were slightly closer to the experimental values on the advancing side. However, both results are comparable to each other and the experimental values on the retreating side.

Figures 2.16 and 2.17 show the normal force and pitch moment comparison for iteration number 9 in Figure 2.15. The CFD+Overset grid method gives better predictions for this case on the advancing side of the tip region. However, it is seen that the CFD+Free-wake method also gives reasonable predictions for this low-speed case for most of the blade regions. Therefore, for this kind of low-speed level flight, the CFD+Free-wake is still an appropriate method for fast evaluations.



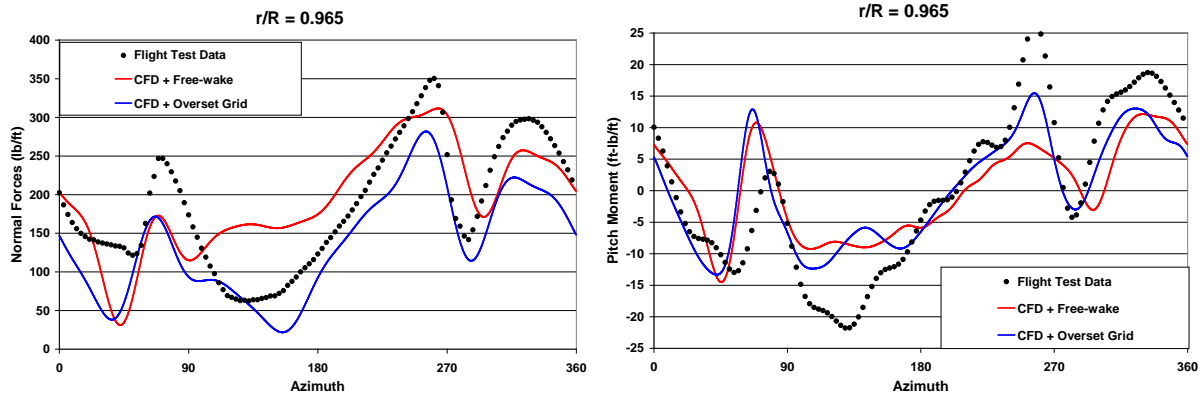


Figure 2.17 Normal Forces and Pitch Moment Comparisons at $r/R = 96.5\%$ (c8513)

2.2.2.3 UH-60A Dynamic Stall Level Flight (c9017)

UH60-A case 9017 is a high-thrust, dynamic-stall case. This is a highly unsteady case, with two wake induced stall regions on the retrieving side. Figure 2.18 shows the convergence history of the CFD+Free-wake predictions. It can be seen that, after 10 iterations, the CFD / CSD coupling almost converges to a single value.

However, the forces predicted by the CFD+Free-wake method do not compare with the measured values as well as those predicted with the CFD+Overset grid method. As shown in the Figure 2.19 and 2.20, the CFD+Free-wake method generally did not capture the two stall regions on the retrieving side, while the CFD+Overset grid method captured most of the stall regions. Thus, for this kind of highly unsteady cases, the CFD+Free-wake method may not be a good choice for fast evaluations.

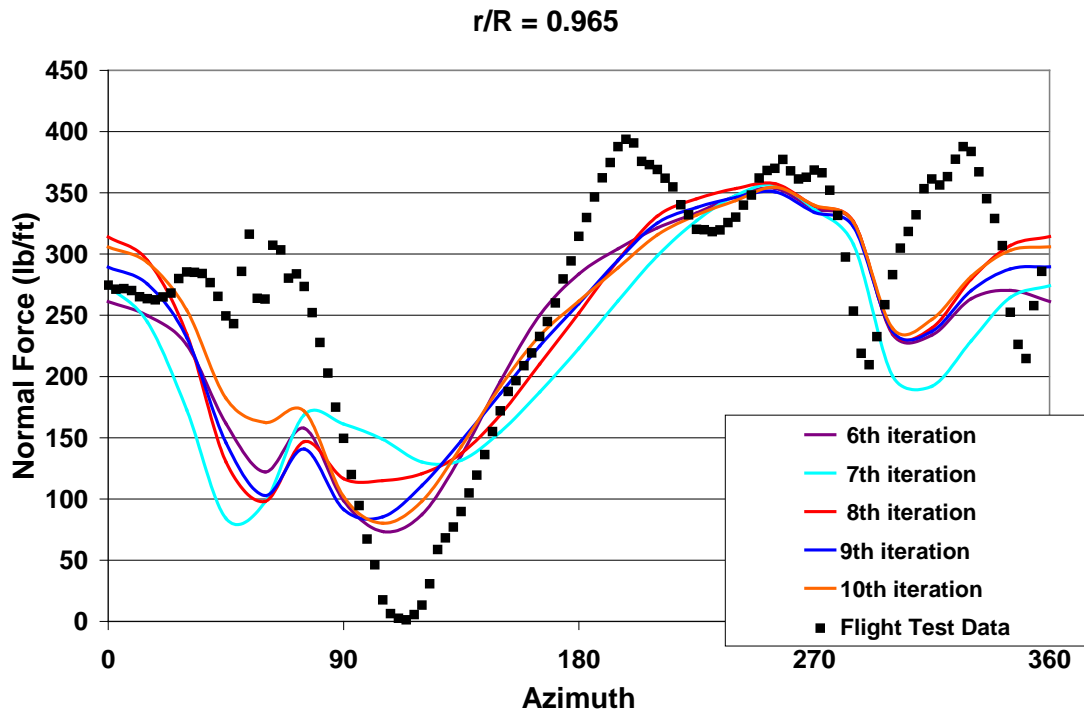


Figure 2.18 Convergence History of CFD+Free-wake Method

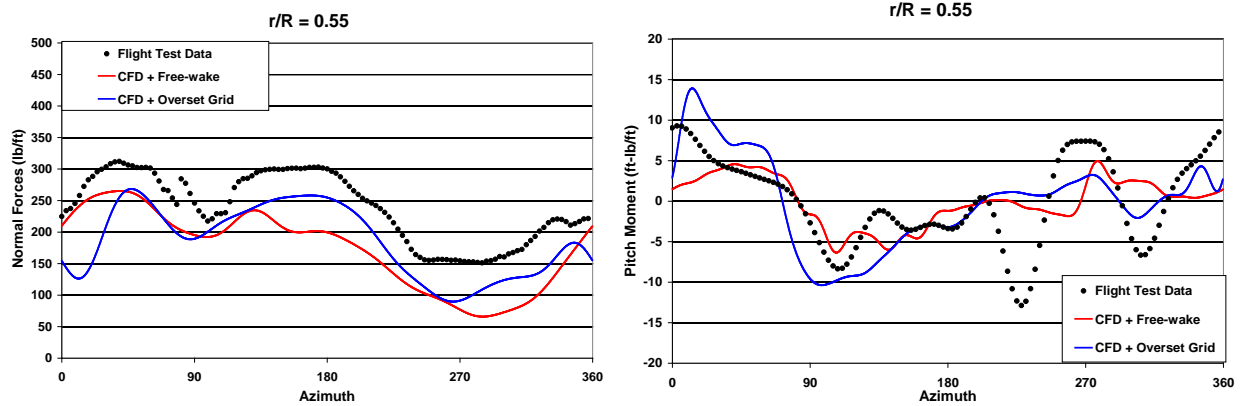


Figure 2.19 Normal Forces and Pitch Moment Comparisons at $r/R = 55\%$ (c9017)

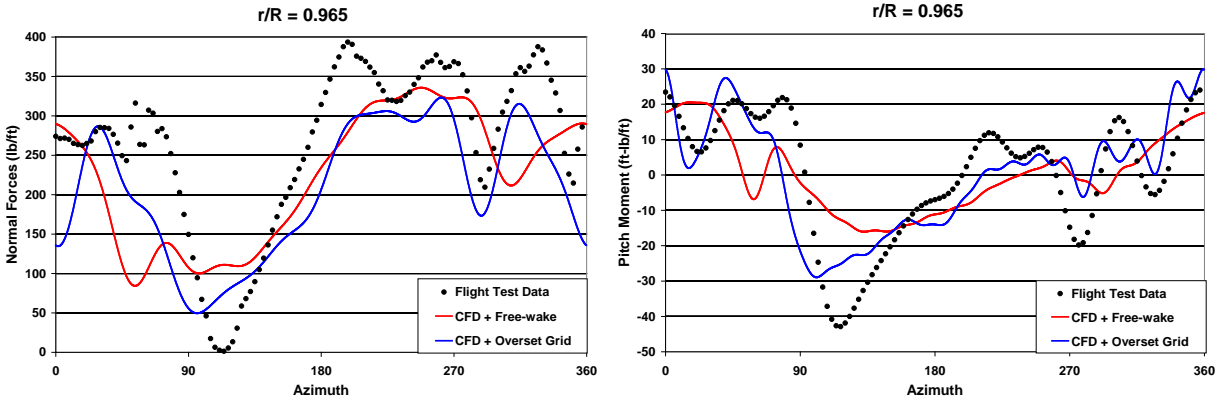


Figure 2.20 Normal Forces and Pitch Moment Comparisons at $r/R = 96.5\%$ (c9017)

2.3 High-order Near-Blade CFD Algorithm Studies for Accurate Source Noise Prediction

For High Speed Impulsive (HSI) noise prediction, the permeable surface (off-surface) Ffowcs Williams – Hawkins (FW-H) equation method (see Figure 2.21), which is dependent on CFD to provide sufficiently accurate, unsteady flow-field data on the acoustic data surface, has become popular. This approach has been proven to give better predictions compared with the traditional impermeable surface (on-surface) method, because the noise generated by the shock wave interaction can be included in this method [2.4]. However, many of these first-principle CFD schemes suffer from numerical dissipation and dispersion errors. Numerical dissipation causes a non-physical gradual decrease in the amplitude of an acoustic wave during its propagation from source to acoustic data surface. Numerical dispersion causes the acoustic waves of different wavelengths to propagate incorrectly at different speeds. Because of these numerical errors, the waves may be distorted in a non-physical manner by the

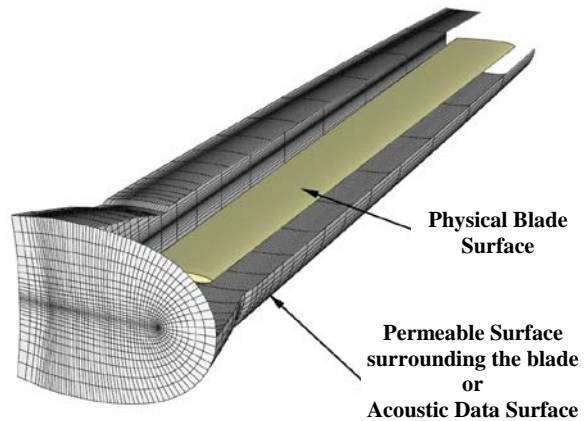


Figure 2.21 High-order CFD scheme provides sufficient spatial and temporal accuracy to propagate acoustic characteristic waves to the acoustic data surface.

time they arrive at the acoustic data surface, so that the accuracy of the flow-field description on the acoustic surface will be reduced. Hence, the far-field propagation based on the permeable surface FW-H equation method will provide non-realistic solutions.

This activity entailed the implementation of the low dispersion and low dissipation Symmetric Total Variation Diminishing (STVD) scheme developed by Helen Yee into the current CFD solver. With a 6th (or even higher 8th order) spatial accuracy algorithm, and with a 2nd order temporal accuracy scheme, the unsteady flow solutions and shock wave interactions can be accurately predicted. Furthermore, this high-order near-blade CFD solver was coupled with the proposed PVTM method, which resolves the transmission of the vortices into the rest of the flow field, to accurately model the physics of the source of BVI noise.

In the baseline TURNS, Roe's approximate Riemann solver [2.5] has been used for the calculation of inviscid fluxes. Considering a cell face at $i+1/2$, in the Roe scheme, the flux $\bar{F}_{i+1/2}$ is computed as:

$$\bar{F}_{i+1/2} = \frac{1}{2} \left[F_i(\vec{q}_L) + F_i(\vec{q}_R) \right] - \frac{1}{2} \left[A(\vec{q}_L, \vec{q}_R) (\vec{q}_R - \vec{q}_L) \right]$$

where the first part $\frac{1}{2} \left[F_i(\vec{q}_L) + F_i(\vec{q}_R) \right]$ is the Physical Flux and the second part $\frac{1}{2} \left[A(\vec{q}_L, \vec{q}_R) (\vec{q}_R - \vec{q}_L) \right]$ is the Numerical Viscosity filter. In the baseline TURNS, the physical flux is solved with the Roe solver, which is second-order. The numerical viscosity filters are 3rd order MUSCL [2.6] (Monotone Upstream-Centered Scheme for the Conservation Laws), and 5th order WENO [2.7] (Weighted Essentially Non-Oscillatory) schemes.

In the low dissipation shock-capturing schemes of Yee et al. [2.8], there are two steps. The first step is the high-order spatial base scheme. The second step is the appropriate characteristic-based filter to improve stability, shock and fine flow structure capturing. Thus, the flux at $i+1/2$, $\bar{F}_{i+1/2}$ can be computed as:

$$\bar{F}_{i+1/2} = \text{Base Scheme} + \text{Numerical Filter Term}$$

For the base scheme, a sixth-order central difference scheme (STVD 6) is currently used:

$$\bar{F}_{i+1/2} = \frac{1}{30} \left[F_{i+3} - 8F_{i+2} + 37F_{i+1} + 37F_i - 8F_{i-1} + F_{i-2} \right] - \frac{1}{2} \left[A(\vec{q}_L, \vec{q}_R) (\vec{q}_R - \vec{q}_L) \right]$$

For the numerical filter term, the MUSCL and WENO schemes included in the baseline TURNS to dissipate the numerical viscosity are already good characteristic-based high-order filters. Therefore, in the second step of STVD scheme, these numerical filter terms are retained to simplify the implementation.

The results shown below compare combinations of these four different schemes, which are MUSCL+ROE, WENO+ROE, MUSCL+STVD6 and WENO+STVD6.

The test case for the high-order scheme is again the UH60-A high speed level flight. The structural analysis using CAMRAD II was included in the computation and coupling iterations between CSD and CFD were conducted until the blade loading predicted by CFD converged. The CFD code used here was the single blade TURNS code with a free-wake module as described in the previous section. In the future, the free-wake module will be replaced by the PVTM module and the code will be used for both high-speed and low-speed BVI simulations.

Figures 2.22 and 2.23 show the normal force and pitch moment predictions of the four different schemes (MUSCL-ROE, MUSCL-STVD6, WENO-ROE, and WENO-STVD6) compared with experimental data. The results for the WENO and MUSCL schemes are similar. However, the STVD6 scheme gives slightly better predictions than the ROE scheme, particularly when there is a large gradient like that at the tip region where transonic flow effects are present.

From the computational time perspective, for this high speed case, the STVD6 scheme generally takes approximately 3% more time than ROE scheme. However, the WENO scheme takes 24% more time than MUSCL scheme. So the MUSCL-STVD6 scheme was selected for the current simulations.

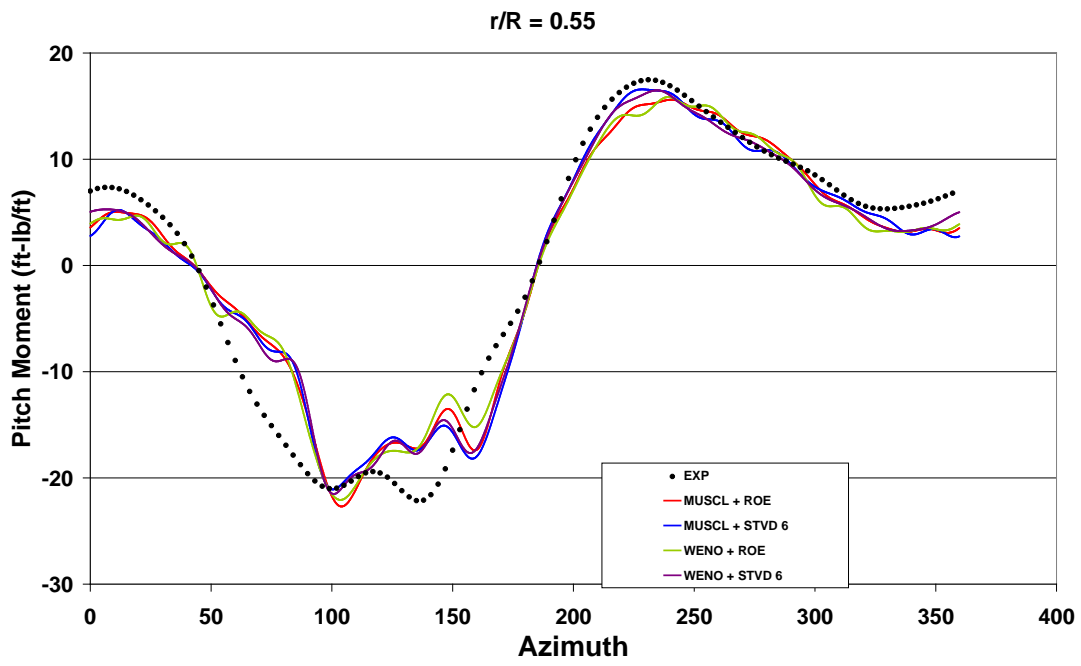
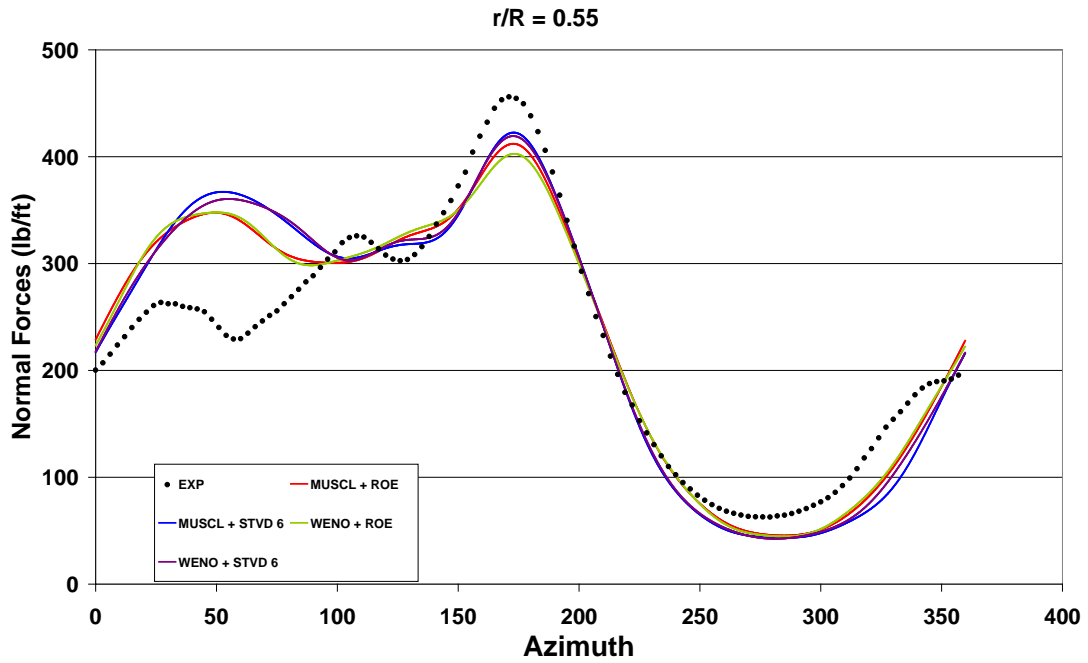


Figure 2.22 Normal Forces and Pitch Moment Comparisons at $r/R = 55\%$ (c8534)

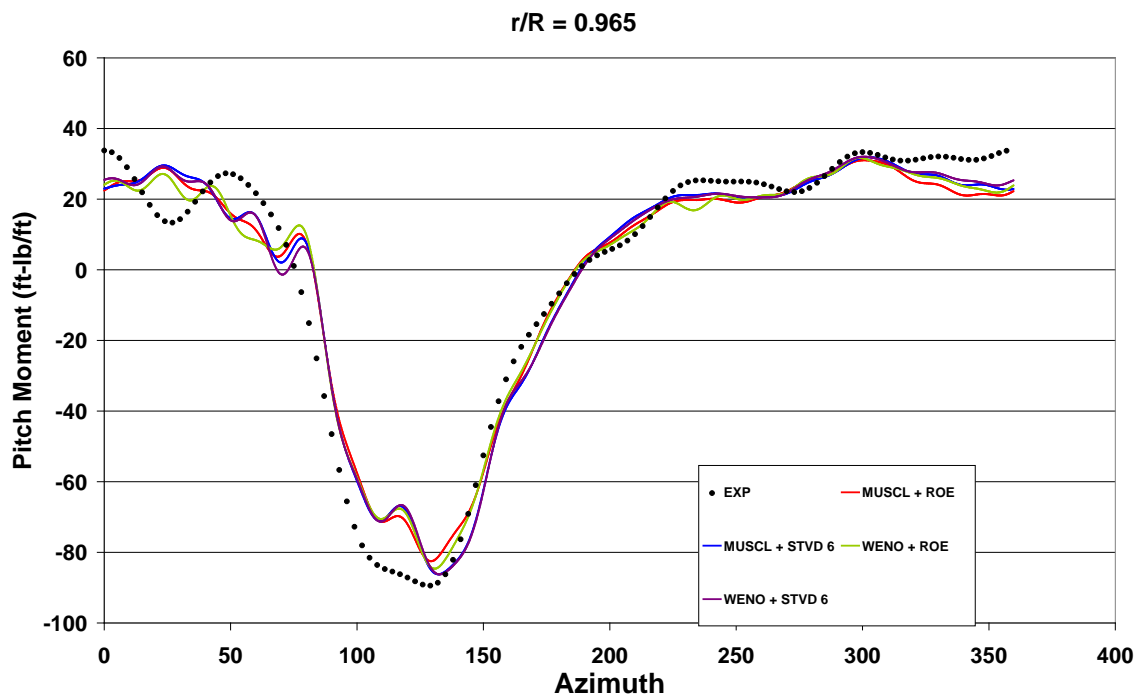
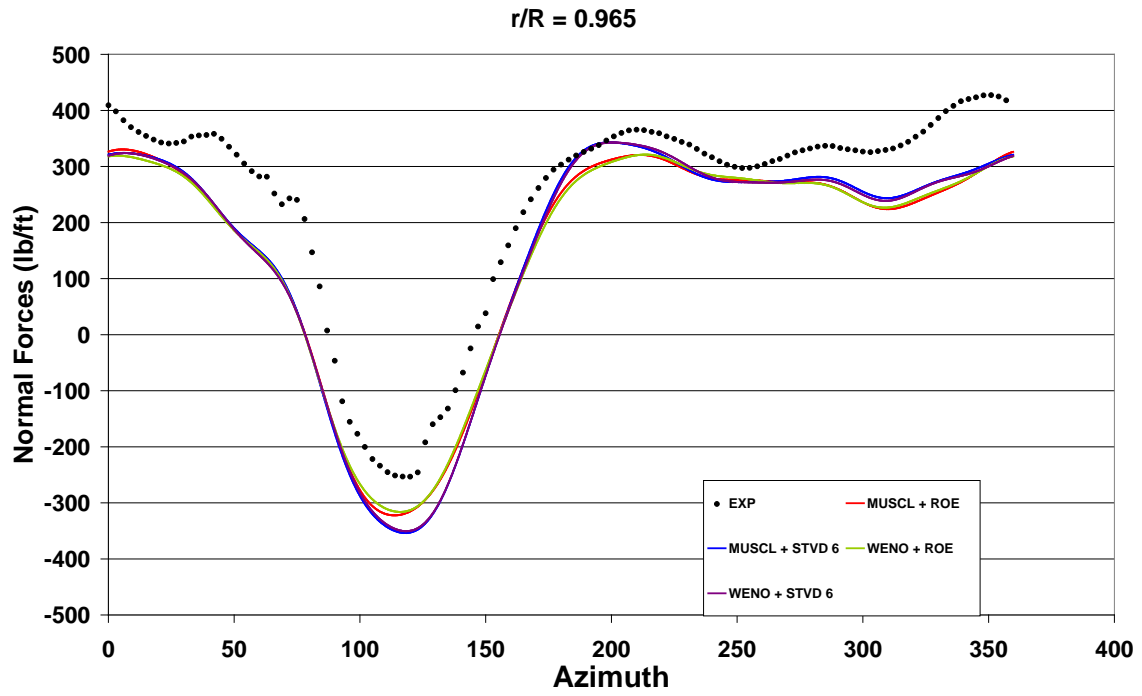


Figure 2.23 Normal Forces and Pitch Moment Comparisons at $r/R = 96.5\%$ (c8534)

2.4 CFD+Overset grid Coupled with CSD for DNW High-speed Source Noise Prediction

For the whole CFD/CSD/Acoustic frame work testing, initial validations were performed using the DNW wind-tunnel test data [2.9, 2.10]. Here, the CFD+Overset grid method was used, and the overset grid is shown in Figure 2.24. Compared to the UH60-A cases, a refined grid was used with 4.82 million near-body grid points ($4 \times 155 \times 139 \times 56$) and 5.69 million back-ground grid points ($4 \times 69 \times 129 \times 160$).

The test case is a high-speed case with advance ratio of 0.310 and advance tip Mach number of 0.873. Figure 2.25 shows the convergence history, where 6 iterations are needed to obtain a converged result.

Comparison of the predicted force and moment coefficients with the experimental data are shown Figures 2.26 and 2.27. It can be seen that for this DNW high-speed case, both the lift and pitch moment coefficient predictions follow trends similar to the measurements. However, the measured data shows some weak BVI effect on the advancing side which is not captured by the CFD predictions with this grid resolution. Conversely, the shock effect on the advancing side for this high-speed case has been captured.

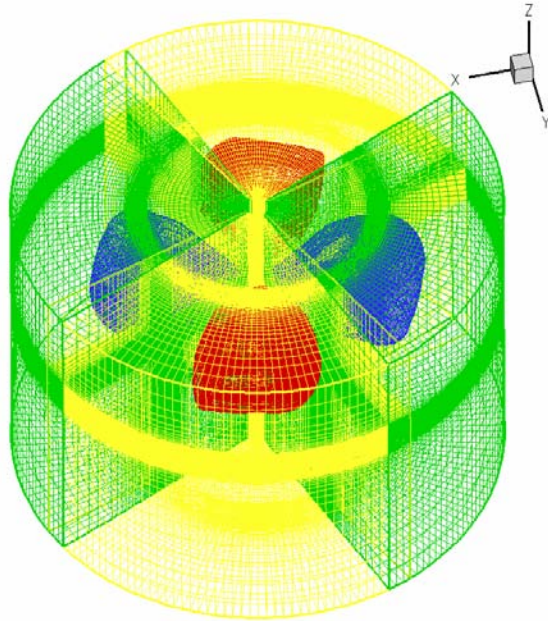


Figure 2.24 The Overset Grid for DNW High-Speed Simulations

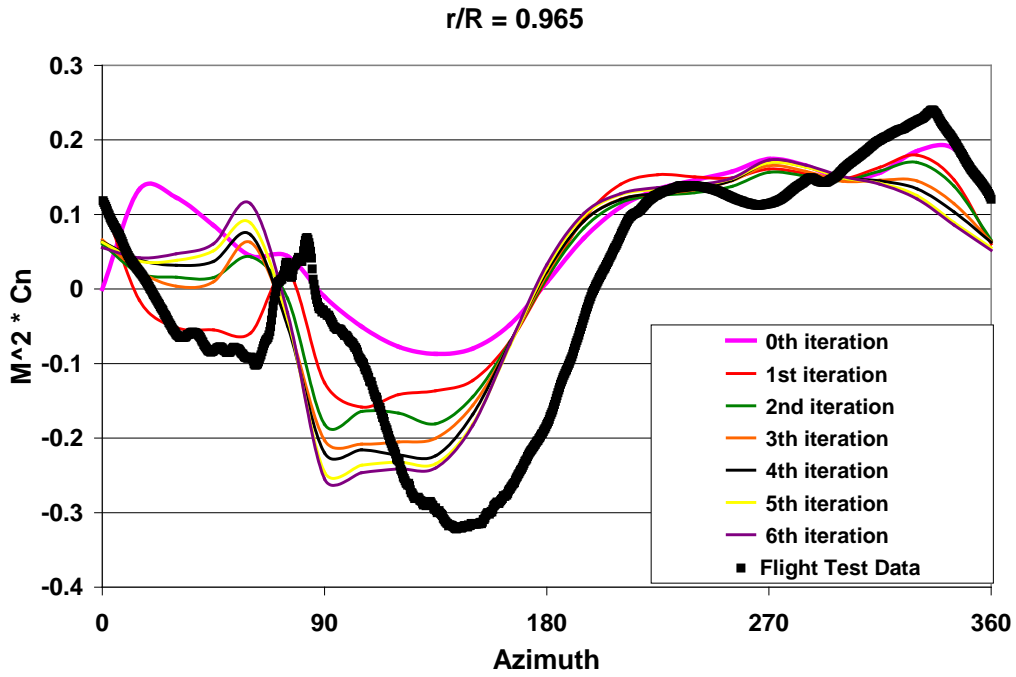


Figure 2.25 The Convergence History for DNW High-Speed Case

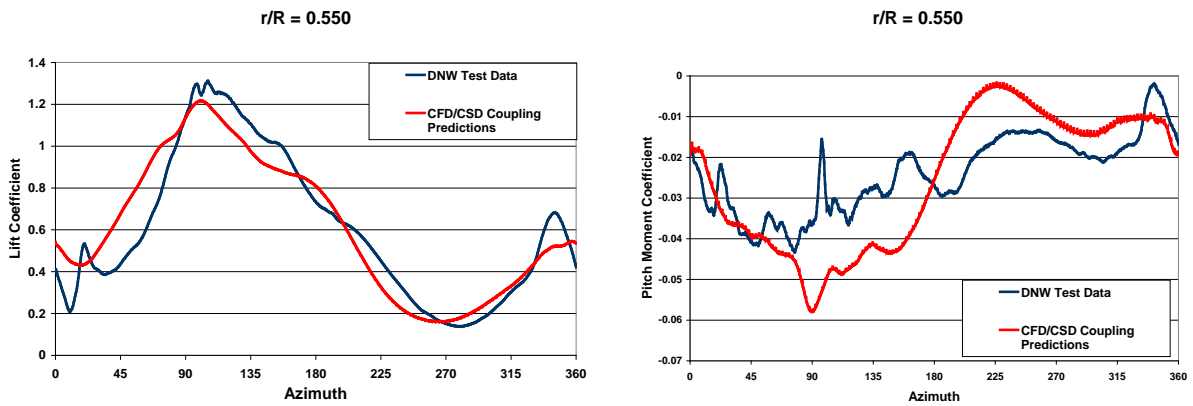


Figure 2.26 Normal Forces and Pitch Moment Comparisons at $r/R = 55\%$ (DNW)

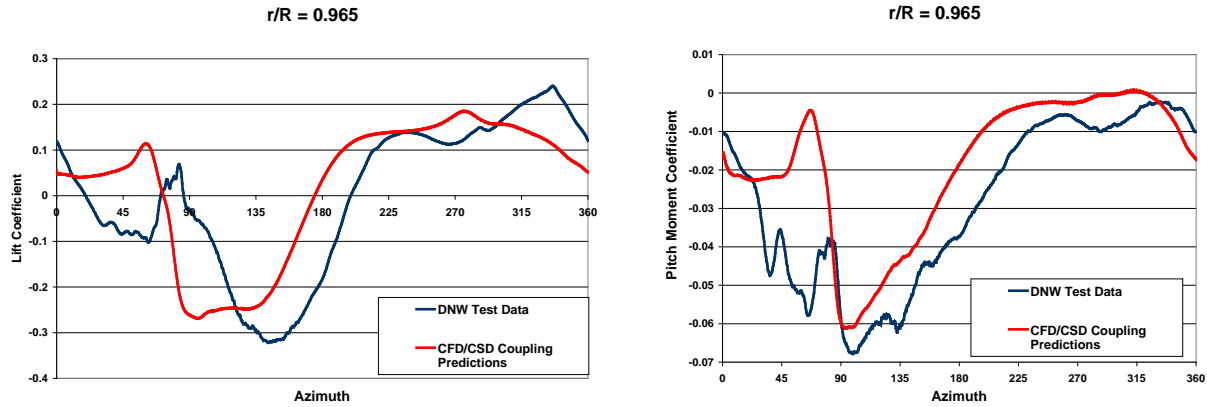


Figure 2.27 Normal Forces and Pitch Moment Comparisons at $r/R = 96.5\%$ (DNW)

2.5 Simulations for HART Baseline Low-speed BVI Case with CFD+Overset and CFD+Free-wake Methods

Simulations have also been performed for the HART low-speed BVI case using the CFD+Overset Grid method. The refined grid was also used with 4.82 million near-body grid points ($4 \times 155 \times 139 \times 56$) and 5.69 million back-ground grid points ($4 \times 69 \times 129 \times 160$).

Figure 2.28 shows the convergence history with the refined grid, illustrating that the code predicts a converged blade loading after 7 iterations with 2 revolutions per iteration. Blade loading comparisons at the 87% span location are shown in the Figure 2.29. Here, the CFD/CSD prediction does not capture the high-frequency BVI variations seen in the experimental data, although the low frequency variations follow similar trends. Thus, it is expected that the BVI noise will not be well predicted by WOPWOP3. For this case, the PVTM method is needed to better capture the wake, or a very fine grid is needed for the overset grid method to capture the far-wake affecting the next blade.

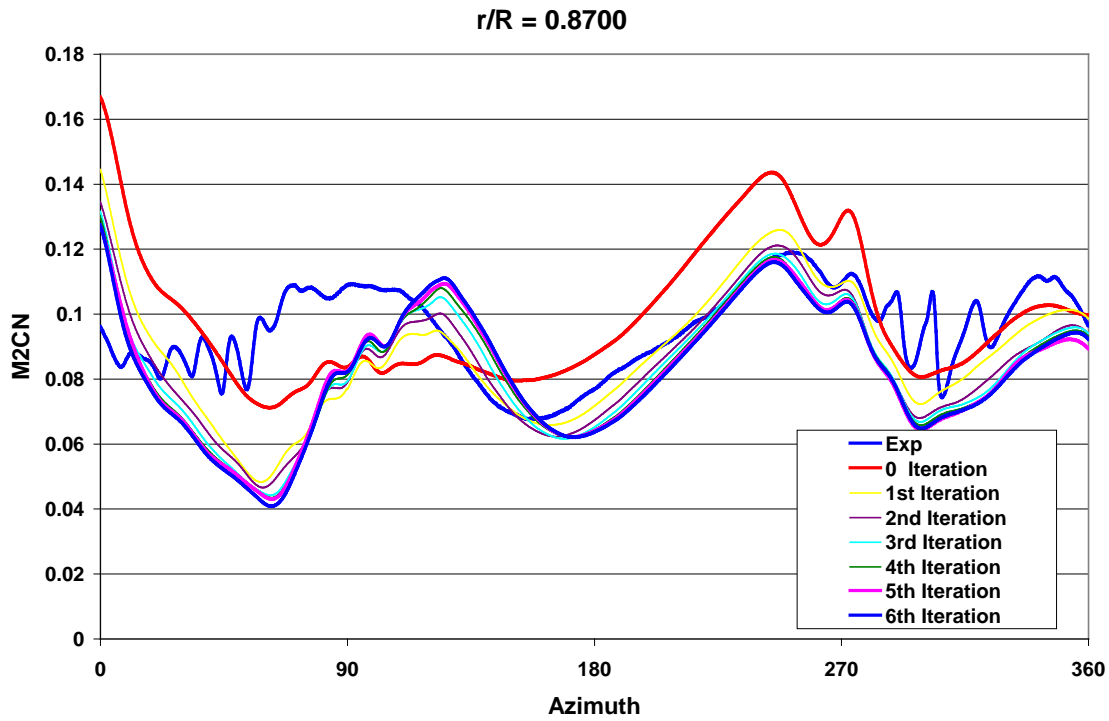


Figure 2.28 Convergence History for the HART low-speed BVI case

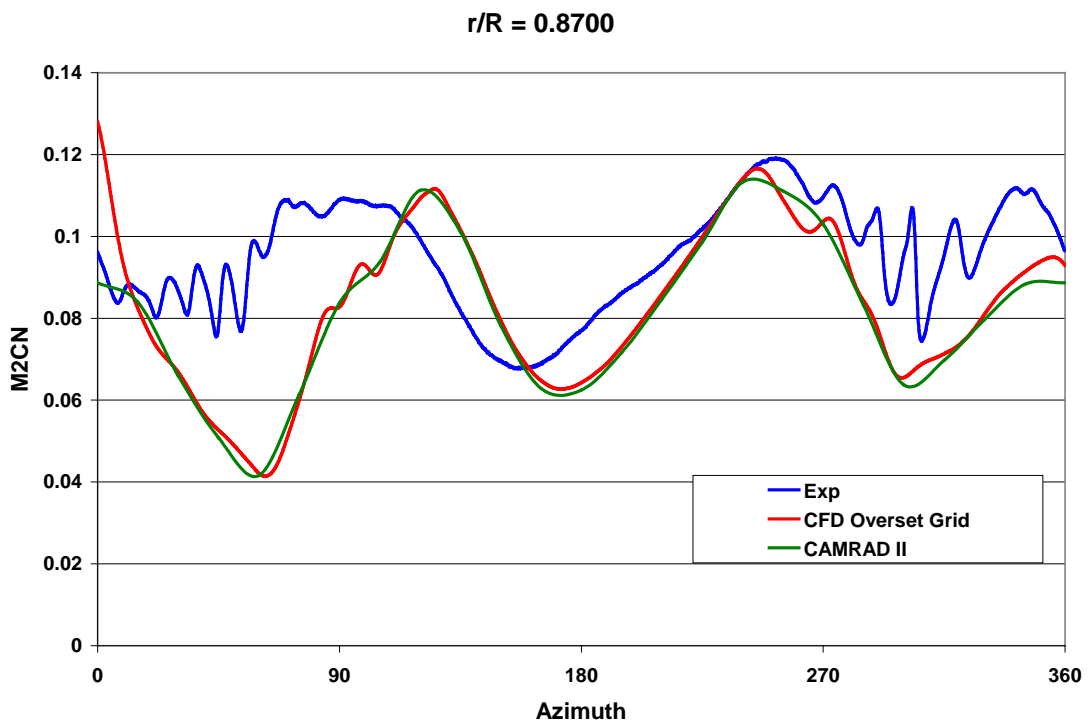


Figure 2.29 The Blade Loading Comparison at 87% Span Location

For this HART case, the CFD+Free-wake method was also used to predict the BVI effects. After a few tests, a refined grid (3.2 million grid points) was used, as shown in Figure 2.30. The coupling iterations with CSD to get trim solutions were converged after 10 revolutions. However, the predicted blade loadings show little of the BVI effects as seen in Figure 2.31.

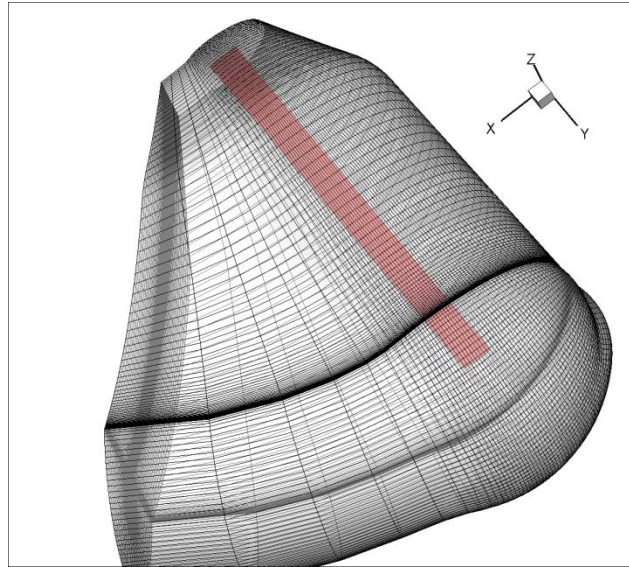


Figure 2.30 The CFD-Freewake Grid

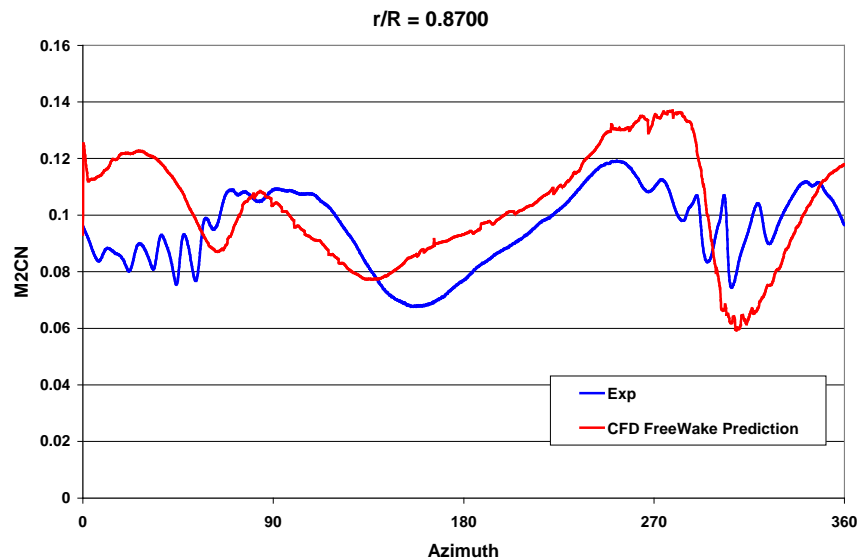


Figure 2.31 The CFD-Freewake Blade Loading Predictions for HART II Baseline Case

Chapter III

Particle Vortex Transport Method (PVTM) for Accurate Wake Modeling

Modeling the highly nonlinear convective wake flow of rotorcraft is challenging. Two major approaches, full CFD overset grid method and free-wake method, were investigated in Task 1 against a variety set of experimental data with different configuration and flight conditions. It has been found that, although the overall blade loading predictions by CFD are in good agreement with the flight test data for a wide range of flight conditions (high-speed, low-speed, and dynamic stall), there are limitations in preserving the wake effects away from the blade for these two methods, such as numerical dissipation and grid dependency.

There is another relatively new method to model the vortex, the Vortex Transport Method (VTM) [3.1], which solves vortex transport equations to determine the evolution of the vorticity field on a uniform Cartesian grid. The approach satisfactorily models the evolution of the vorticity field, but the vortex source used is derived from a simplified 2D aerodynamics model.

The Co-I, Dr. Phuriwat Anusonti-Inthra, developed a combined approach under another NRA contract (NNL07AA32C). This approach uses CFD in the vicinity of the rotor blades to capture the generation of the vortices, and PVTM to resolve the evolution of the vortices in the rest of the flow field (see Figure 3.1). The fully-coupled CFD-PVTM is implemented by appropriate information exchange between CFD and PVTM at every time step. This approach for wake capturing is relatively new and requires further investigation and validation.

In this task work, this fully coupled CFD-PVTM approach was used to model the wake flow from the rotor systems. A series of systematic and comprehensive validations was conducted to assess modeling limitations and to improve the accuracy and efficiency of the approach.

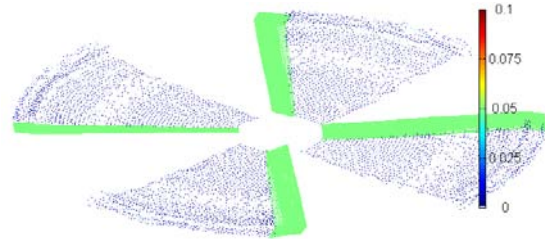


Figure 3.1 Gridless PVTM prescribes and preserves evolution of wake from rotor systems.

3.1 UH60 simulations using coupled CII/TURNS/PVTM method

The coupled CII/TURNS/PVTM methodology was applied to simulate two UH60 cases (c8534 and c8513). The near body grid for UH60 blade used by TURNS is presented in Fig. 3.2. The grid has about 1.6 million points and extends about 1 chord length in all directions, except behind the blade tip where the grid only extends about 0.5 chord. The variations in blade profiles and twist distribution of the UH60 blade grid are shown in Fig. 3.3. The PVTM cell resolution is 0.5 chord. A loose coupling methodology is used to obtain coupled trim solution. More detailed explanations of the PVTM method and the validation results with UH60 forward flight data can be found at Ref. 3.2.

UH60 Case c8534

Simulations for case c8534, $\mu = 0.34$, are obtained using a coarse PVTM grid. The PVTM grid for this case is shown in Fig. 3.4. With the PVTM grid, the finest resolution zone covers about 2 full revolutions of the rotor wake. Nine coupled trim iterations are simulated, and the convergence history of the trim parameters and vehicle trust are presented in Figs. 3.5 and 3.6, respectively. The results are shown using 5 and 20 TURNS sub-iterations. It is observed that the 20 sub-iteration run converge to different trim values. The comparison of the resulting rotor blade normal force and the experimental data at nine radial stations is presented in Fig. 3.7. Overall the correlations of the blade normal force are good for all radial stations. The 20 sub-iteration results provide slightly better correlation than the 5 sub-iteration results. The vorticity field results are shown in Fig. 3.8. Overall, the vorticity fields with 5 or 20 sub-iterations are similar, with only slight differences in the vorticity with the wake age of more than 1 revolution.

UH60 Case c8513

For case c8513, $\mu = 0.1489$, the coupled simulations are obtained using 20 sub-iterations for TURNS and the same PVTM grid system (Fig. 3.4). The convergence history of the thrust and trim parameters are given in Fig. 3.9. The blade normal force correlation between the simulation and experimental data as seen in Fig. 3.10 is generally good, except at a few radial stations. Another comparison of the normal force predicted from CFD/PVTM simulations with full CFD and CFD/free wake results are shown in Fig. 3.11 for completeness. The converged vorticity field results from PVTM in Fig. 3.12 show the presence of super-vortices behind the rotor.

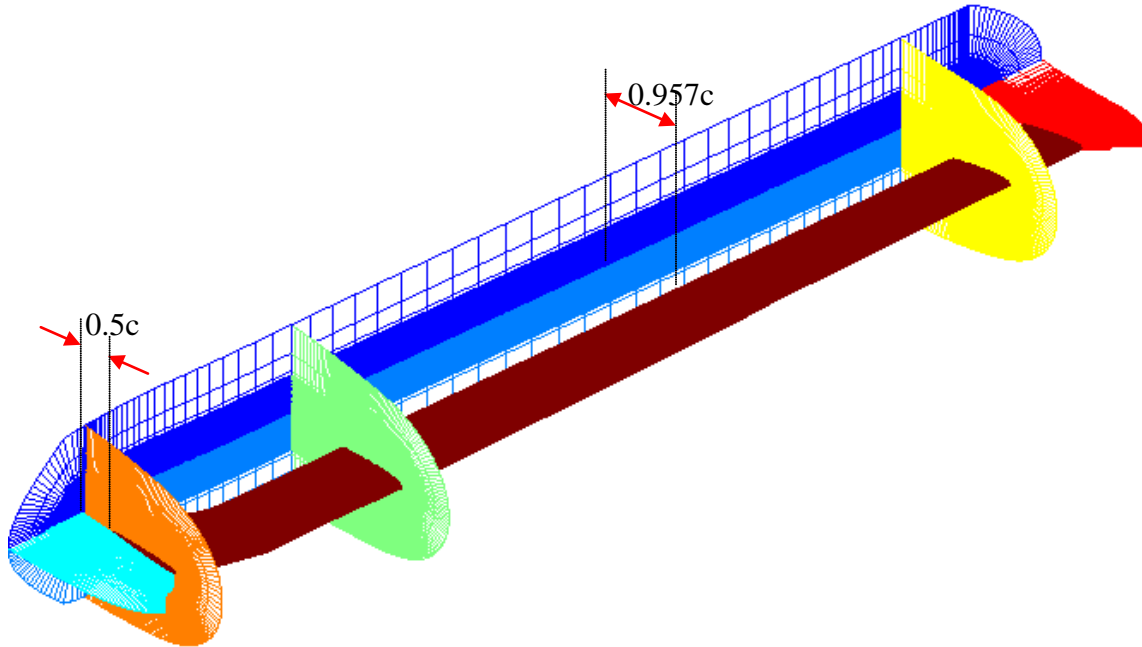


Figure 3.2 UH60 blade grid for near body CFD calculation (Dimension: 219×131×55)

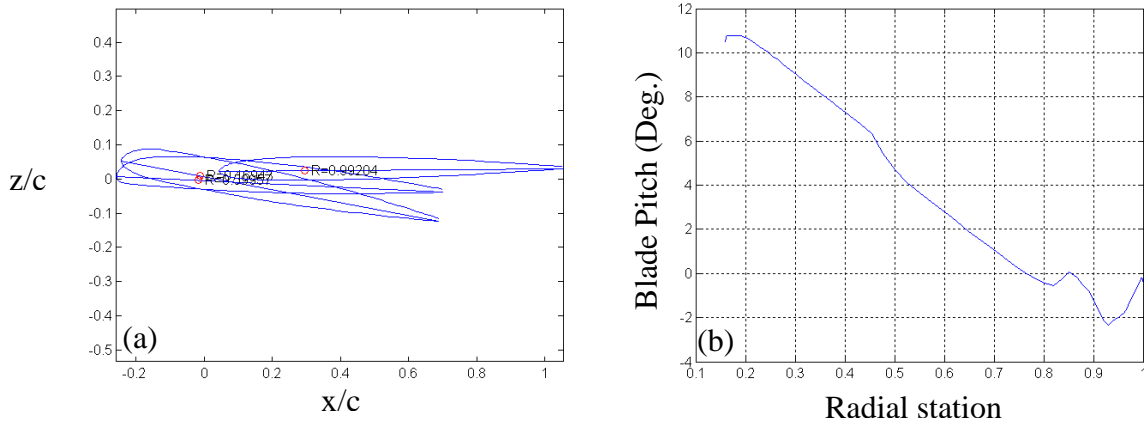


Figure 3.3 (a) UH60 blade profiles and (b) blade twist distribution

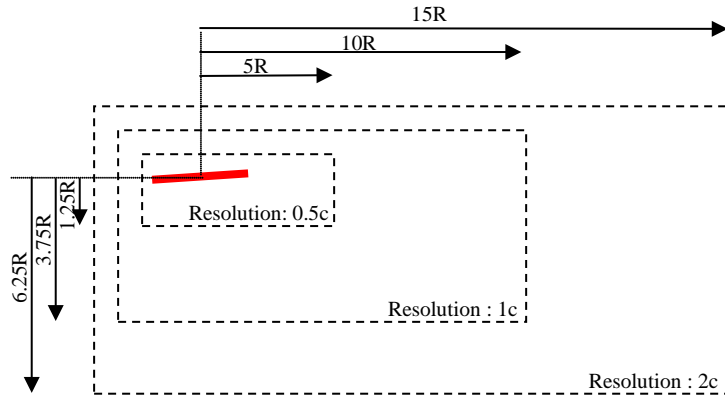
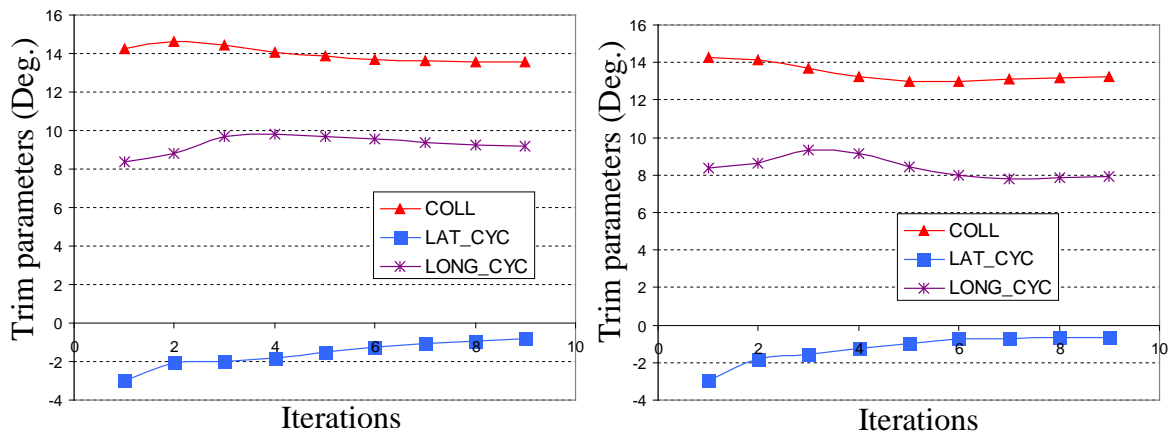


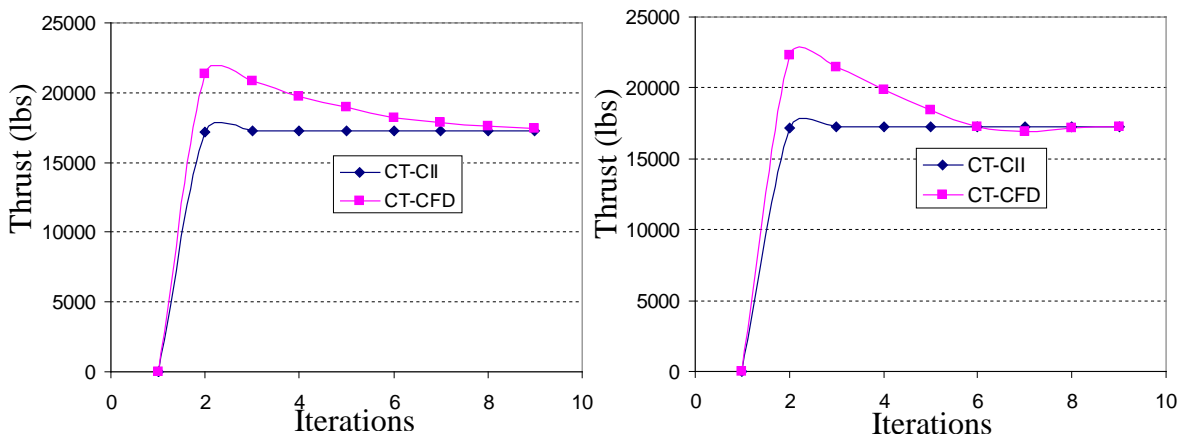
Figure 3.4 Schematic of PVTM grid with multi-resolution zones for c8534



(a) with 5 sub-iterations

(b) with 20 sub-iterations

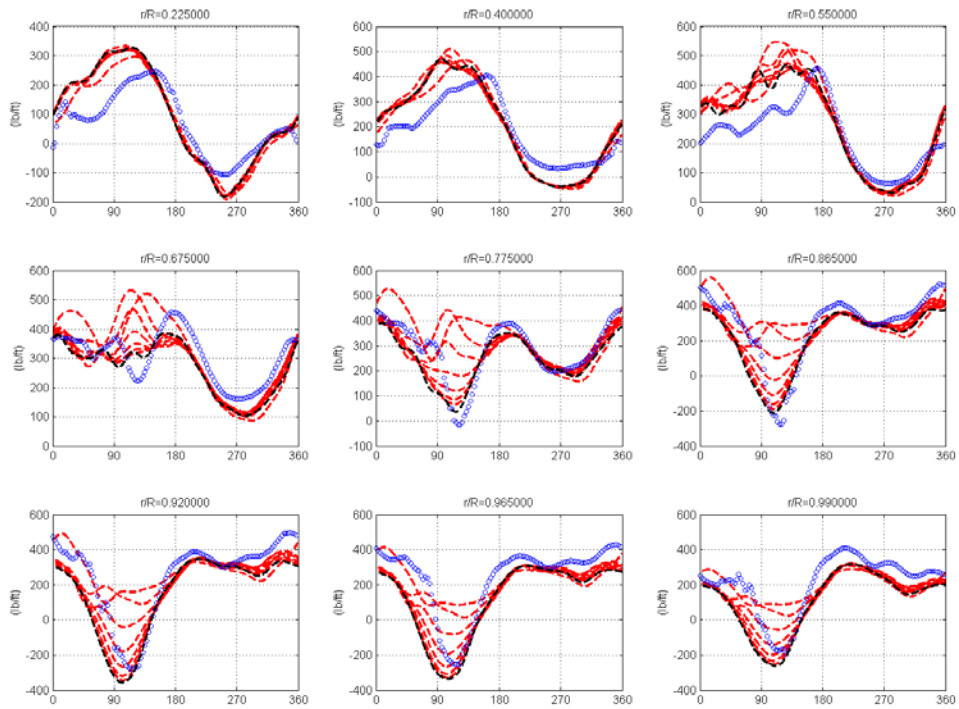
Figure 3.5 Convergence history for rotor trim parameters (UH-60A c8534)



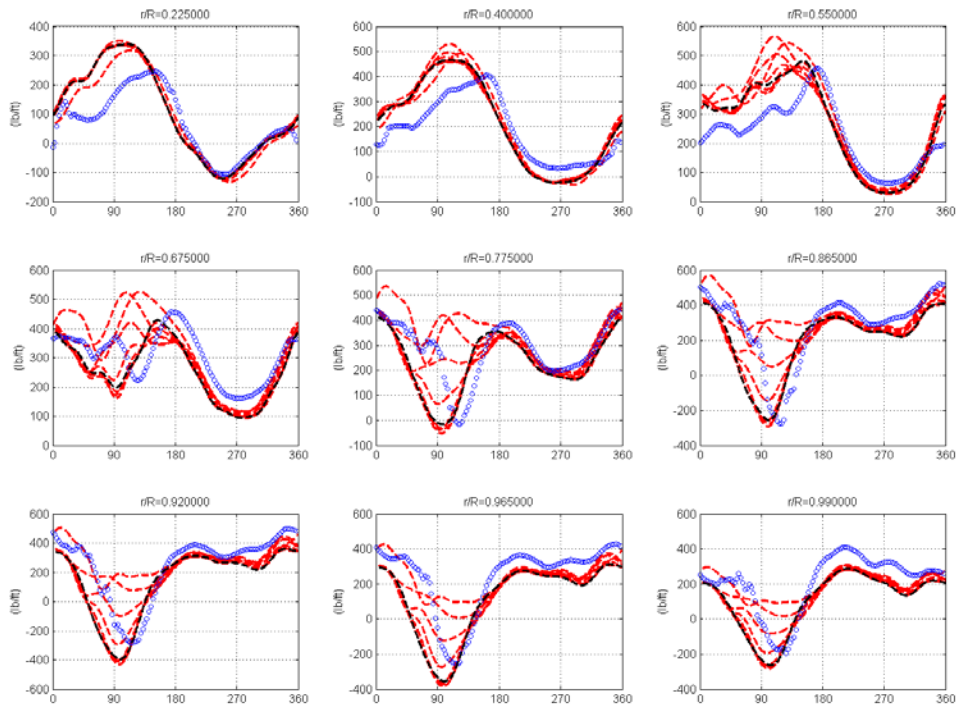
(a) with 5 sub-iterations

(b) with 20 sub-iterations

Figure 3.6 Convergence history for rotor thrust (UH-60A c8534)



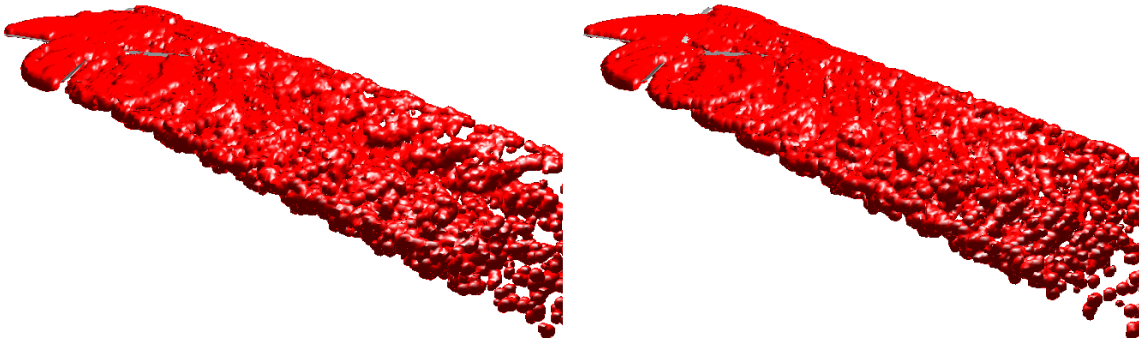
(a) with 5 sub-iterations for TURNS



(b) with 20 sub-iterations for TURNS

Figure 3.7 Normal force comparison (UH-60A c8534)

(o: flight test data, --- intermediate iterations, --- converged CFD/CSD/PVTM solution)



(a) with 5 sub-iterations

(b) with 20 sub-iterations

Figure 3.8 Converged vorticity field (UH-60A c8534)

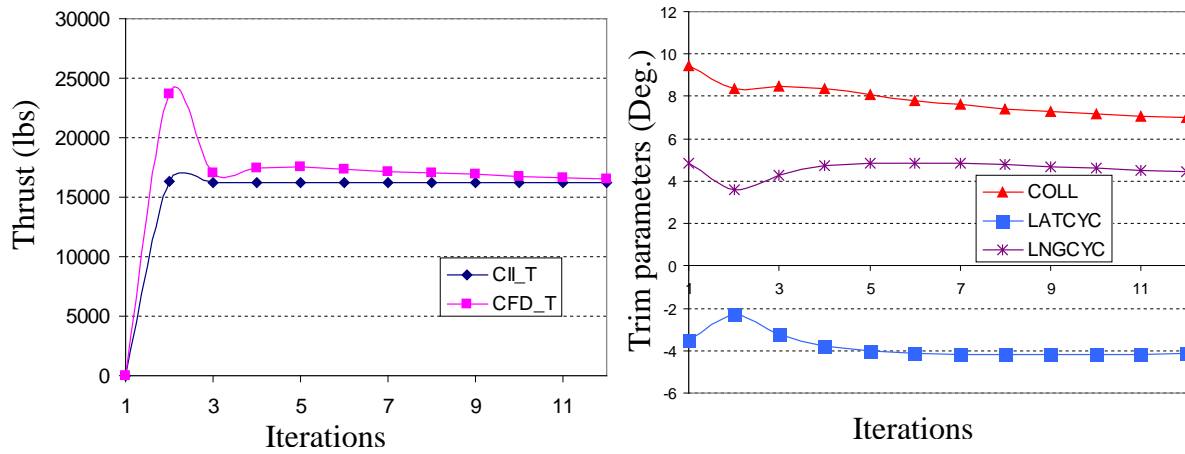
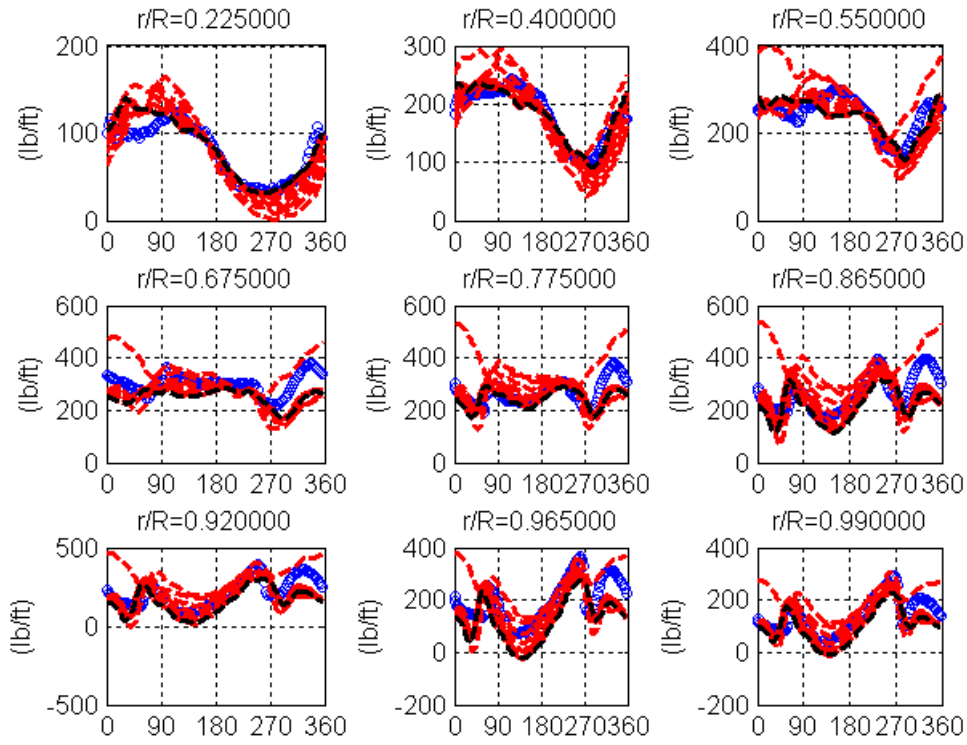
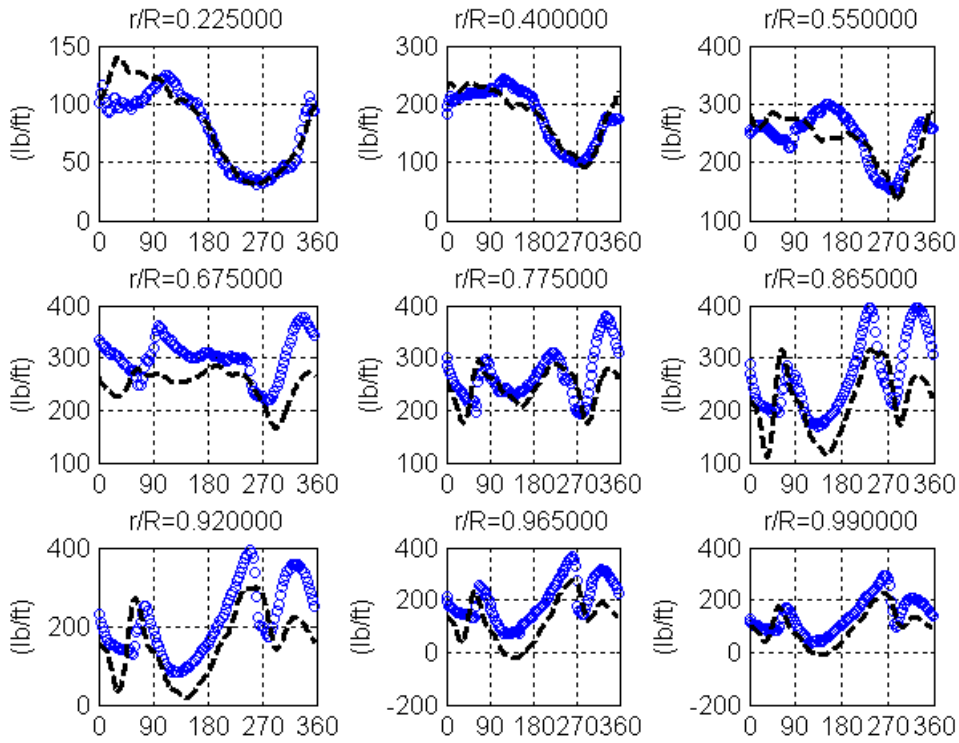


Figure 3.9 Convergence history of thrust and trim parameters (UH-60A c8513)



(a) Intermediate CSD/CFD/PVTM results



(b) Converged CSD/CFD/PVTM results

Figure 3.10 Comparison of normal force (UH-60A c8513)

(o: flight test data, ---: intermediate results, ---: converged CFD/CSD/PVTM result)

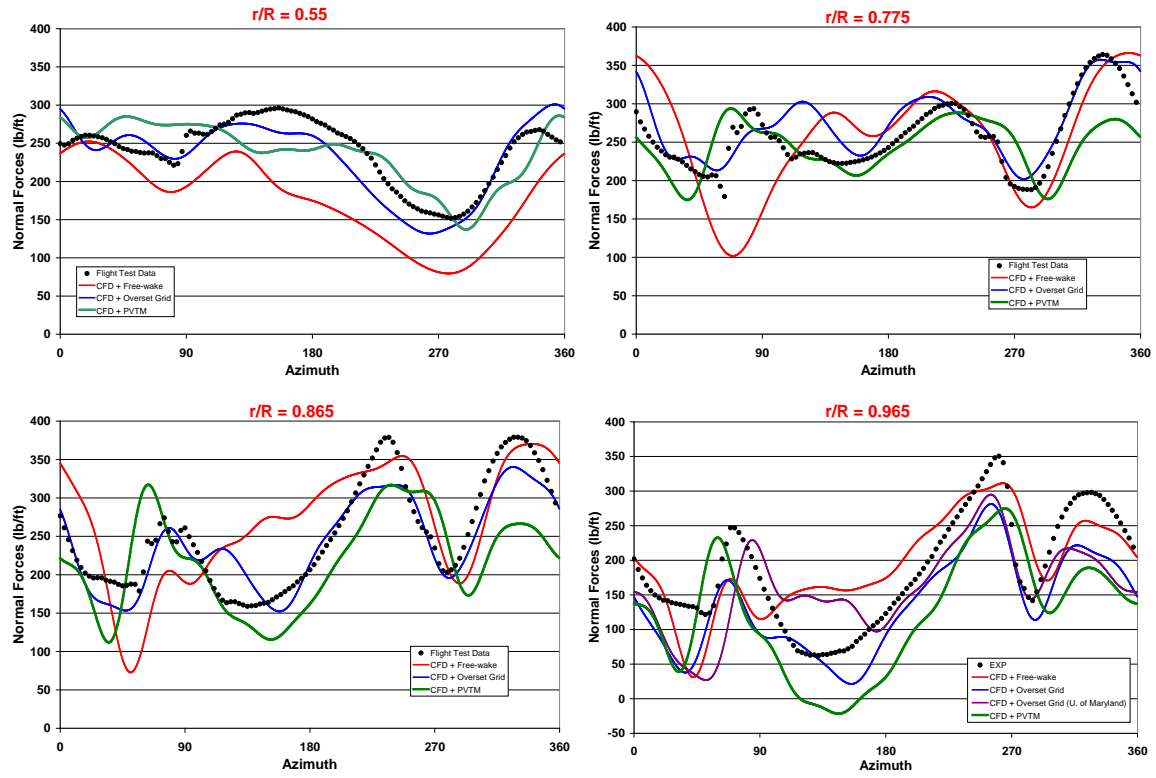


Figure 3.11 Comparisons of normal force (UH-60A c8513)

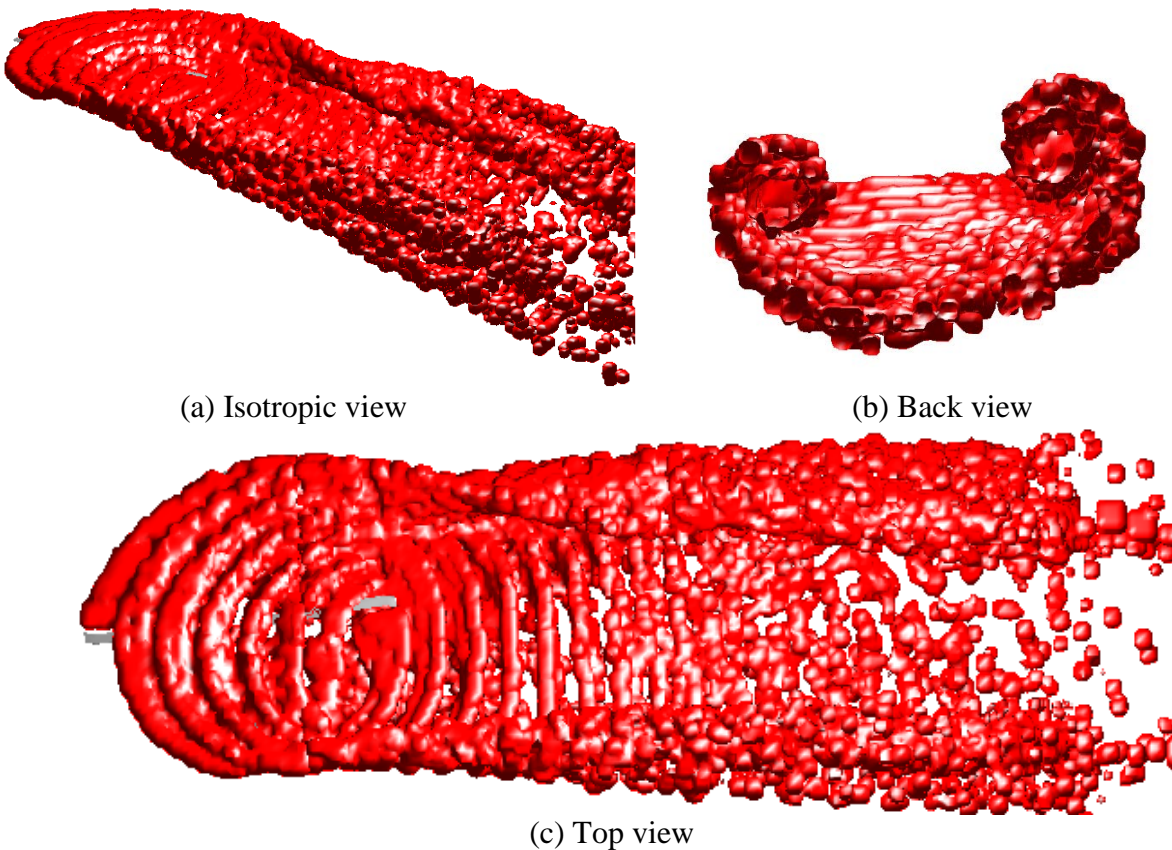


Figure 3.12 Converged vorticity field (UH-60A c8513)

3.2 HART II simulations using coupled CII/TURNS/PVTM method

The coupled CII/TURNS/PVTM method was also used to simulate the HART II baseline case [3.3], descent condition at $\mu = 0.15$. The near body grid for TURNS and the blade twist profile are shown in Figs. 3.13 and 3.14, respectively. A wind tunnel trim is used to simulate the wind tunnel test condition. The TURNS grid has about 1.5 million cells. The case is simulated using low and high PVTM resolutions.

Low Resolution PVTM

The low resolution PVTM cells are similar to the one described in Fig. 3.4. The convergence history of the thrust and trim parameters are shown in Fig. 3.15. The comparisons the normal blade force and the experimental data are given in Figs. 3.16-17. The only experimental data available is for one radial station ($r/R = 0.87$). The correlation of the converged low resolution result is fair. Some BVI events are observed in the first and fourth quadrants for the blade, but the magnitude and duration of the events are very different from the experimental data. Figure 3.18 shows the converged vorticity field for this case. The super-vortices behind the rotor are apparent.

High Resolution PVTM

The high resolution PVTM grid structure is shown in Fig. 3.19. Two sets of high resolution results are presented with different initial conditions: (A) using the converged low resolution wake results as the initial condition, (B) using no initial wake. Figures 3.20-22 show the results from the Case (A). It is seen that the trim variables obtained from the converged low resolution PVTM wake is very different from the required trim for high resolution PVTM wake. However, the high resolution results are still not converged. The normal force comparison is presented in Figs. 3.21-23. Slightly better correlation is seen for the high resolution results than the low resolution results. Case (B) results are presented in Figs. 3.23-24. The converged high resolution results and the acoustic predictions were not available for this final report, but they will be sent for a paper publication in the future.

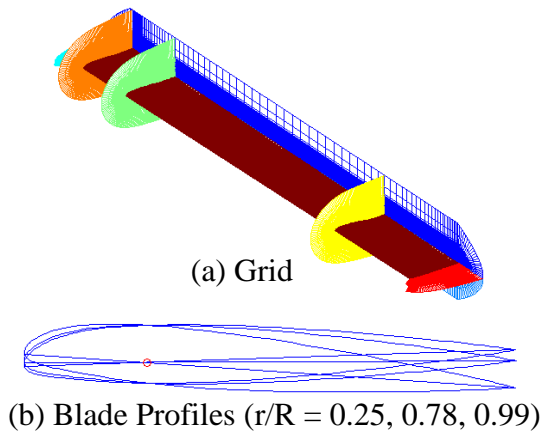


Figure 3.13 HART II blade grid

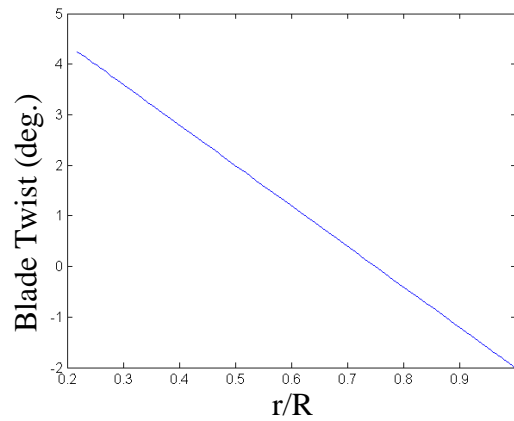


Figure 3.14 HART II blade twist profile

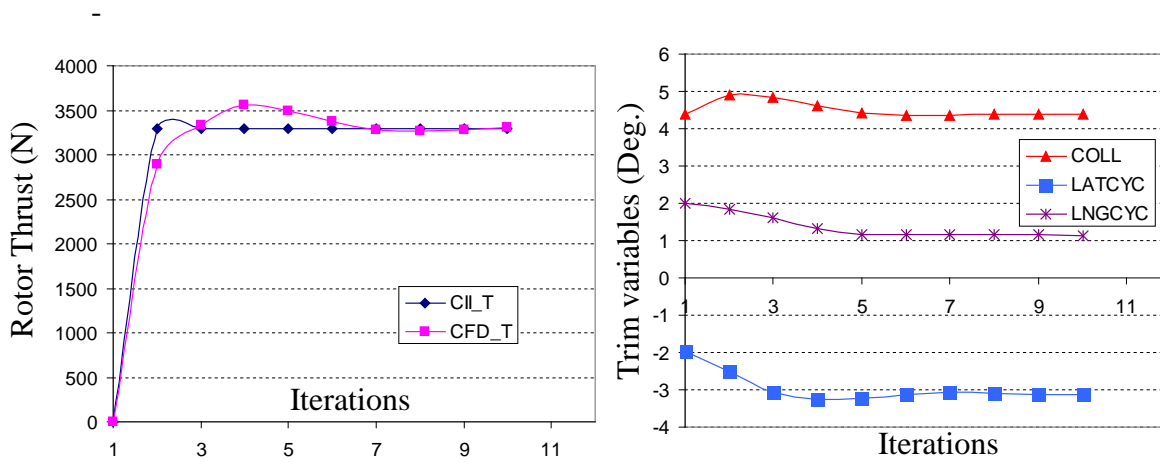


Figure 3.15 Trim convergence history (HART II: BL, low resolution)

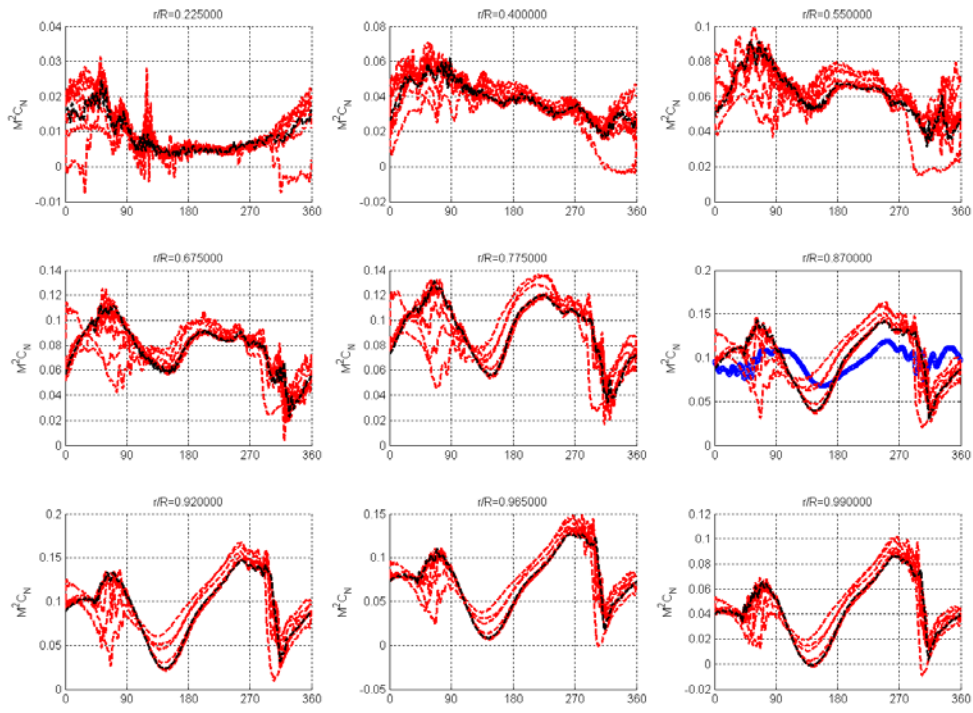


Figure 3.16 Comparison of blade normal force (HART II: BL, low res.)
 (oo: exp. data, ---: intermediate results, ---: converged CFD/CSD/PVTM result)

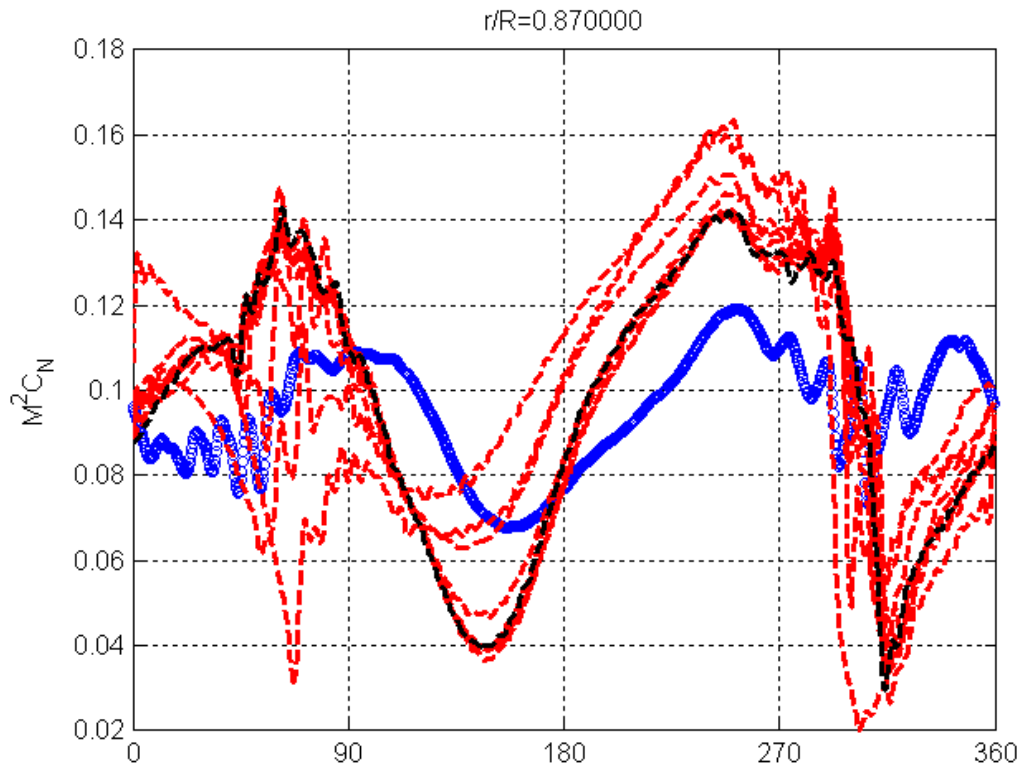
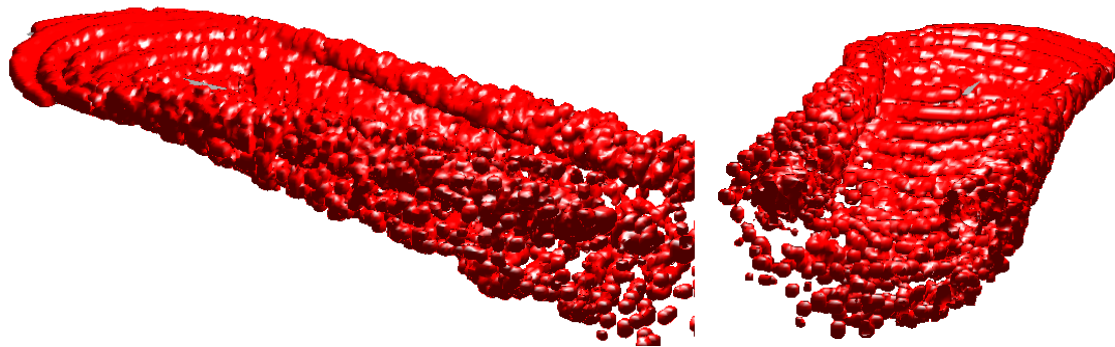


Figure 3.17 Comparison of blade normal force at $r/R = 0.87$ (HART II: BL, low res.)
 (oo: exp. data, ---: intermediate results, ---: converged CFD/CSD/PVTM result)



(a) View from retreating side (b) view from back
Figure 3.18: Converged vorticity field (HART II: BL, low resolution)

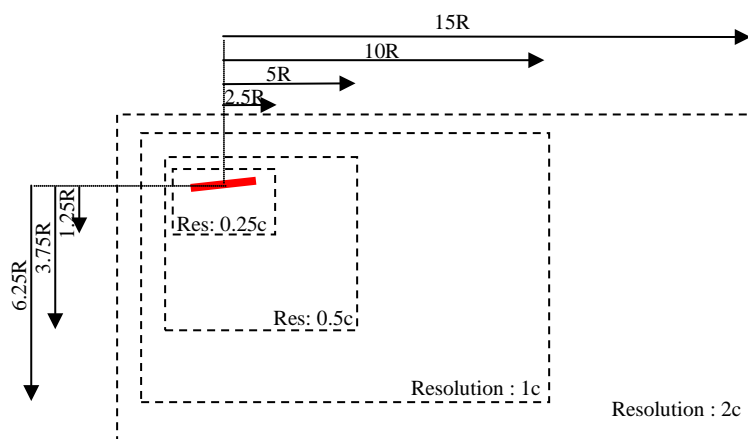


Figure 3.19 Schematic of PVTM grid with multi-resolution zones for HART high resolution results

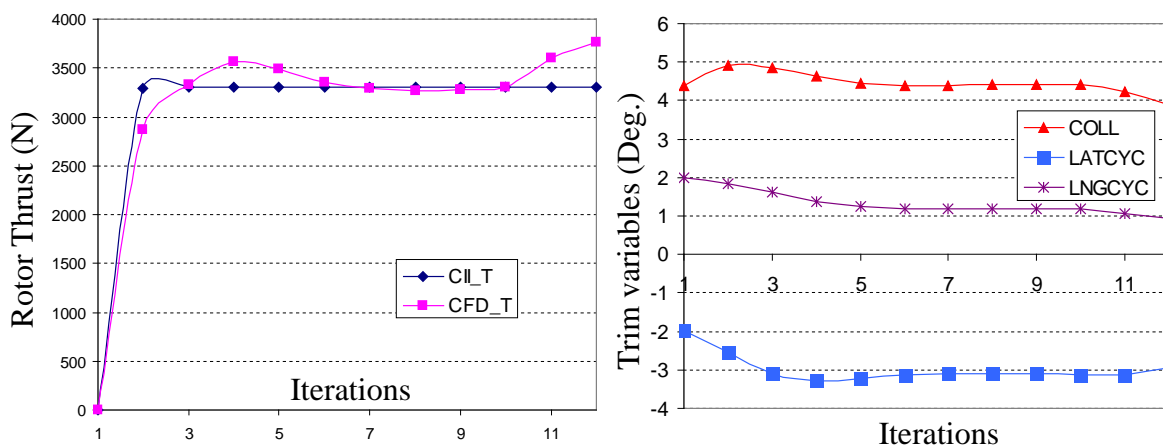


Figure 3.20 Trim convergence history (HART II: BL, high resolution: A)
 (Iteration 1-10: low resolution PVTM, Iterations 11-12: high resolution PVTM)

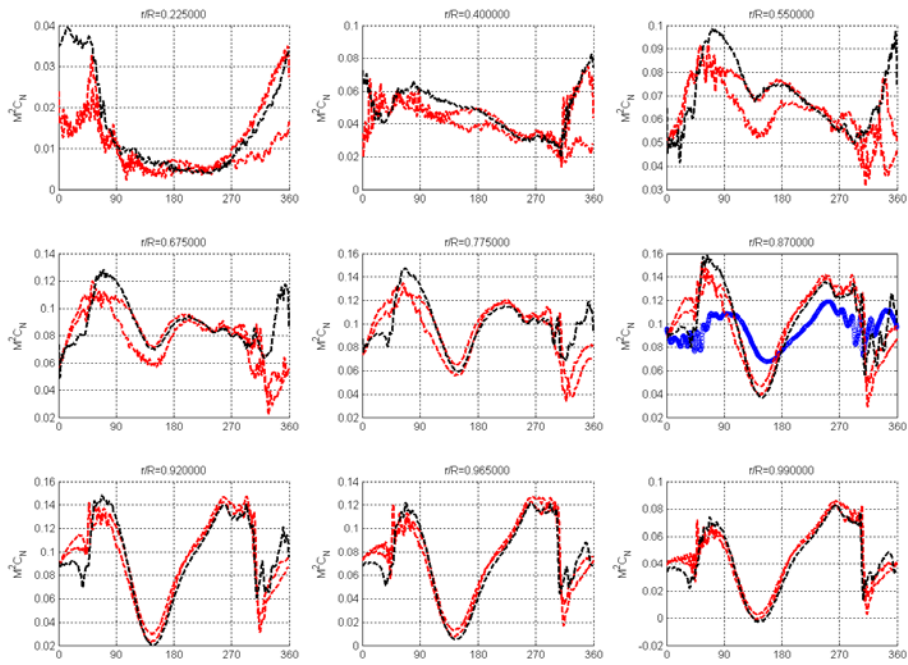


Figure 3.21 Comparison of blade normal force (HART II: BL, high res. A)
 (oo: exp. data, --: intermediate results, - -: last CFD/CSD/PVTM result)

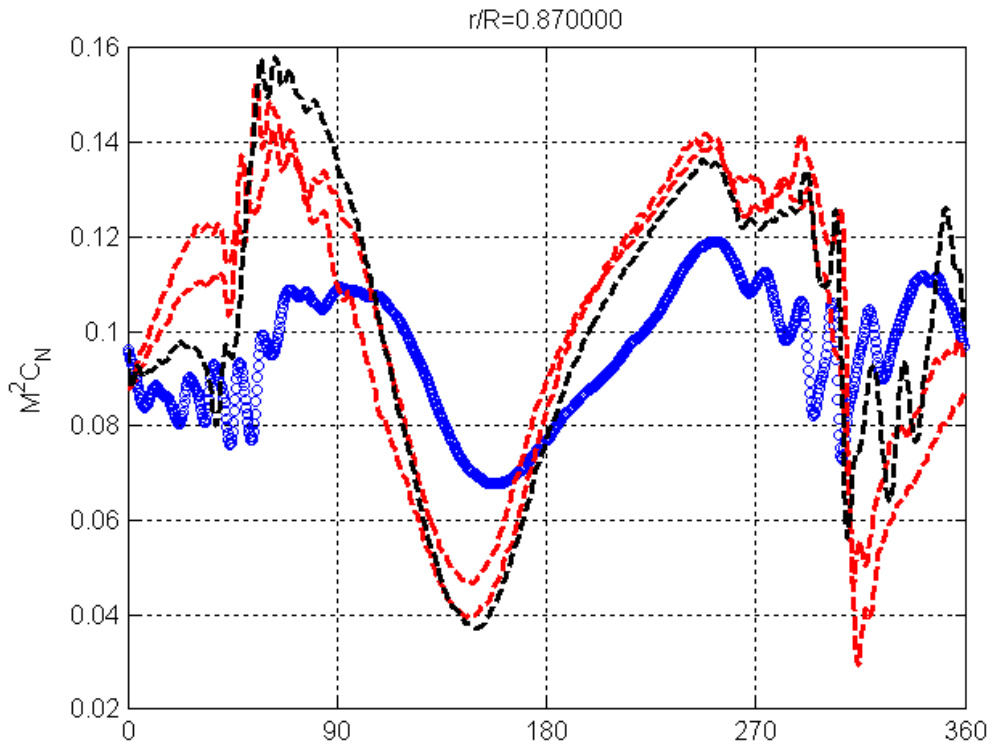


Figure 3.22 Comparison of blade normal force at $r/R = 0.87$ (HART II: BL, high res. A)
 (oo: exp. data, --: intermediate results, - -: last CFD/CSD/PVTM result)

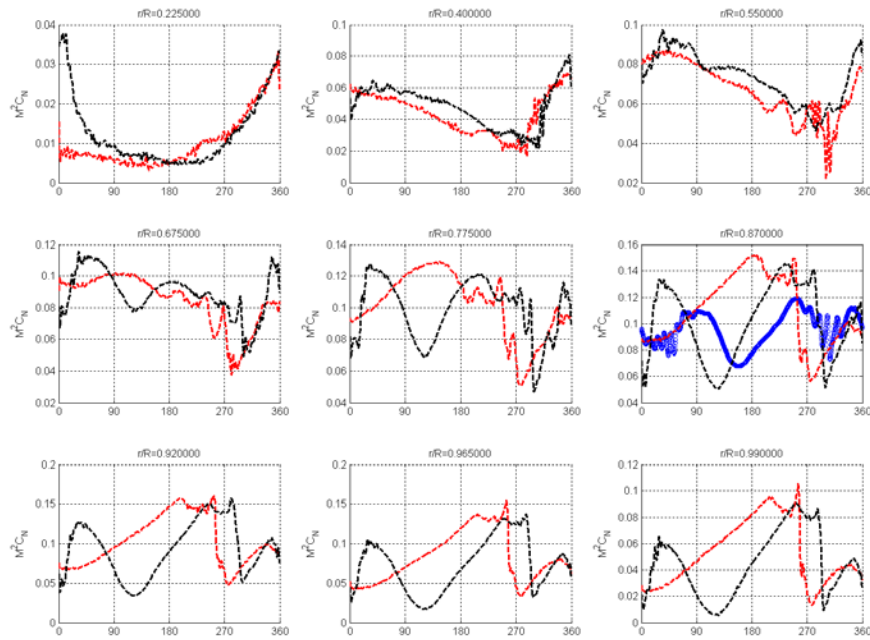


Figure 3.23 Comparison of blade normal force (HART II: BL, high res. B)
 (oo: exp. data, --: intermediate results, -: last CFD/CSD/PVTM result)

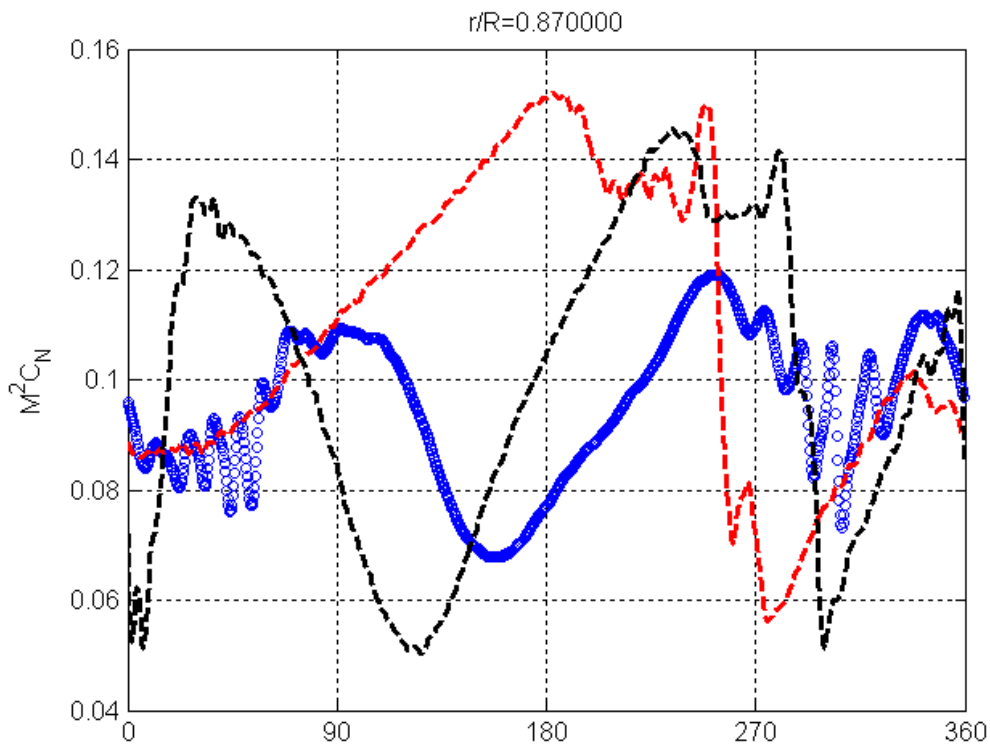


Figure 3.24 Comparison of blade normal force (HART II: BL, high res. B)
 (oo: exp. data, --: intermediate results, -: last CFD/CSD/PVTM result)

Chapter IV

Improved and Efficient Interfaces with Acoustic Propagation Codes

Another essential element in the MUTE tool is the noise prediction code. Currently, WOPWOP3 (also known as PSU-WOPWOP) [4.1] provided by LaRC has been used as the main acoustic propagation code. WOPWOP3 solves Farassat's retarded-time formulation 1A [4.2] of the Ffowcs Williams-Hawkings (FW-H) equation [4.3] and computes the rotorcraft tone noises at given observer locations. These predictions are based on the blade loading on an impermeable surface or the unsteady flow-field description provided by CFD simulations on a permeable surface.

The traditional method of rotor noise propagation uses the rotor blade surface as the acoustic data surface, which is an impermeable surface. The blade loadings provided either by the comprehensive analysis (CAMRAD II) or the CFD (TURNS) are integrated into the FW-H equation as the source term. This method can accurately propagate and calculate the thickness noise and loading noise. However, for high-speed cases when the high-speed impulsive (HSI) noise is dominant, errors are incurred with the impermeable surface method because the quadrupole term from the shock wave interaction is not included in the FW-H equation. Thus, recently, a new method of using the FW-H equation on a permeable surface was developed within WOPWOP3. With the availability of an accurate flow-field description on this permeable acoustic data surface from the CFD, it is expected that this approach would improve the accuracy of the HSI noise prediction.

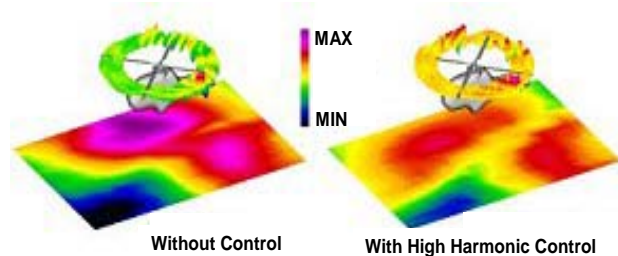


Figure 4.1 Noise propagation from the rotorcraft to observer locations in the far-field.

4.1 DNW High-Speed Noise Prediction with Impermeable Surface Method and Permeable Surface Method

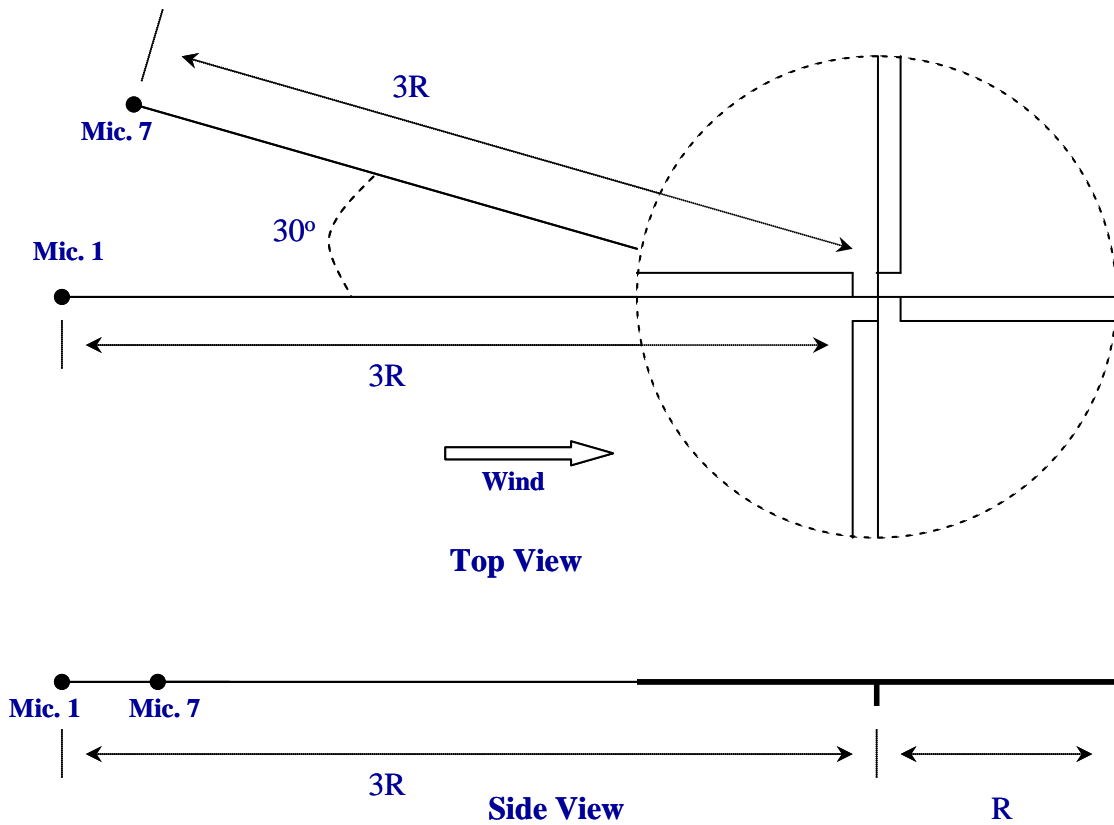


Figure 4.2 The Acoustic Experiments Set-up (Microphone 1 & 7)

In the DNW High-speed data set [4.4], some acoustic measurements are also available for comparison. As seen in Figure 4.2, the acoustic sound pressure from two microphones (Microphone 1 and 7) are recorded. These two microphones are located ahead of the rotor blade and in the same plane as the rotor surface.

Figures 4.3 and 4.4 show the time averaged total sound pressure read by microphones 1 and 7 in the experiments. In these two figures, the high-negative peak is due to compressible flow effects which include the shock wave interactions. The noise due to vortex interactions can also be seen clearly in the experiments

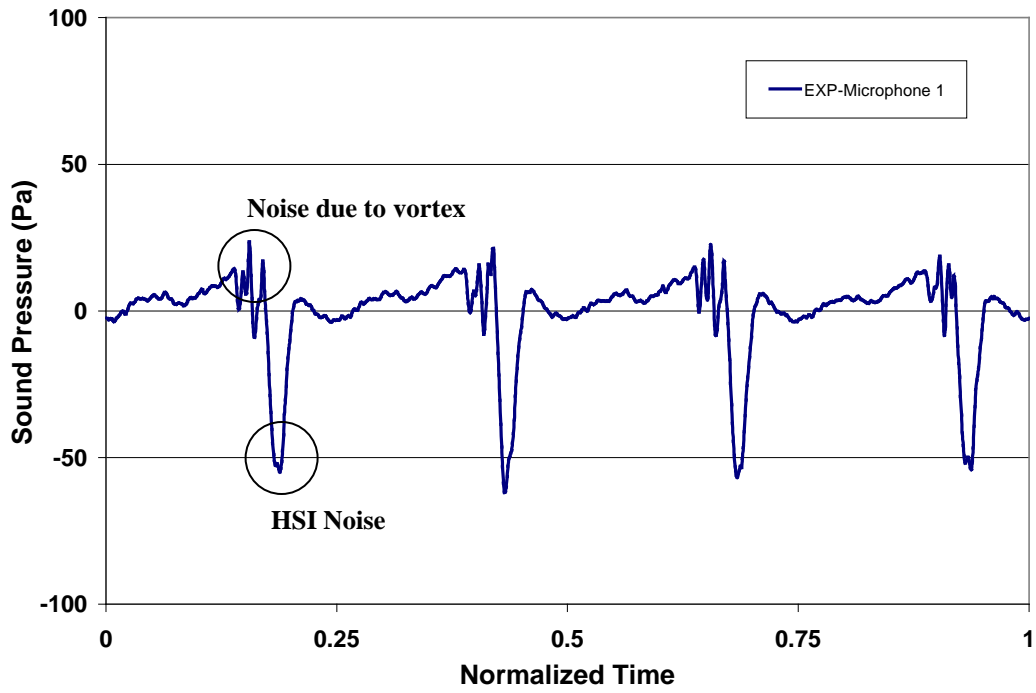


Figure 4.3 The Sound Pressure of Microphone 1

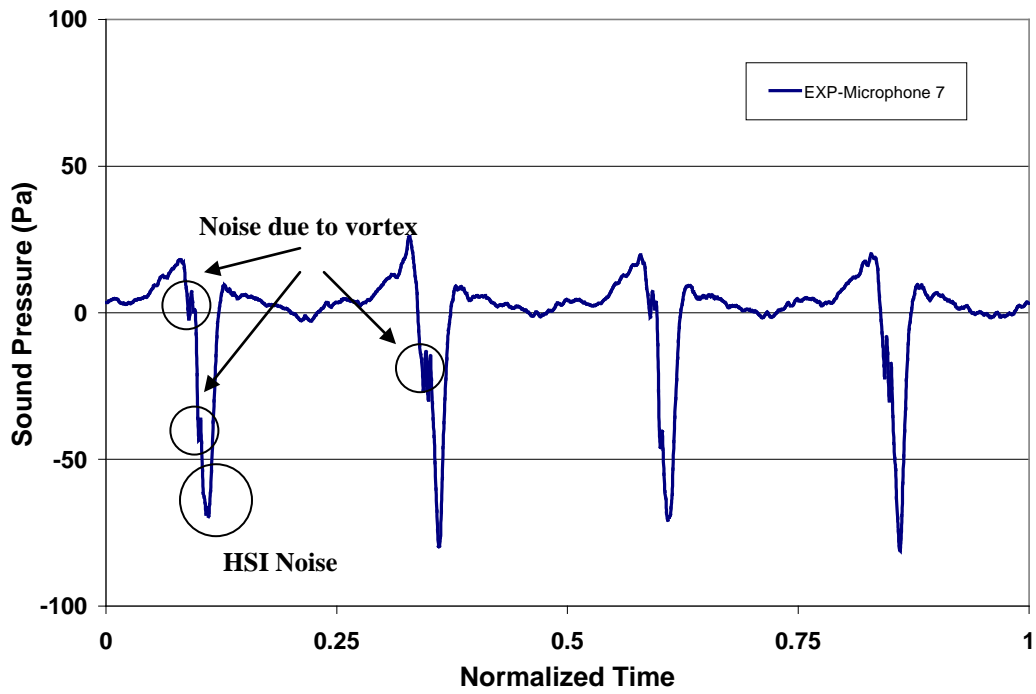


Figure 4.4 The Sound Pressure of Microphone 7

Two acoustic prediction methods were used for the acoustic analysis with WOPWOP3, the impermeable surface method and the permeable surface method. At first, the impermeable surface method with compact loading patches is used, where the blade surface loadings (C_n , C_d and C_m) at each span location are used to obtain the acoustic signature at the observer points. As shown in Figure 4.5 and 4.6 for both Microphone 1 and 7, the impermeable surface method with loading patches did not fully capture the negative peak of the HSI noise, nor did it capture any of the vortex effects. Subsequently, the impermeable surface method with surface pressure as input was used, as shown in Figures 4.7 and 4.8. When using the surface pressure for the impermeable surface method, some improvement of the negative noise peak predictions was obtained. However, it is still below the measured levels and the noise due to the vortex effects was not captured.

For the permeable surface method, four different sized acoustic data surfaces (ADS) were chosen to investigate the effects of the permeable surface size on the acoustic predictions. The first one, referred to as the original surface, was used to verify the accuracy of the interface codes and WOPWOP3 input. The grid index range of the original surface, relative to the near-body CFD grid, is: I from 11 to 123, J from 5 to 125, K from 1 to 43, where I is the chord-wise direction, J span-wise and K normal directions. Three additional ADS grids were extracted from the CFD solutions for comparisons, where for Grid 1, I ranged from 9 to 125, J from 5 to 125 and K from 1 to 44; for Grid 2 I from 8 to 126, J from 5 to 125 and K from 1 to 43; and for Grid 3 I from 10 to 124, J from 5 to 125 and K from 1 to 43. Figures 4.9--4.11 show the comparison of the original grid with the additional grids. The acoustic predictions at Microphone 1 for these four acoustic data surfaces are compared at Figure 4.12. It is seen that the predictions using the original surface and Grids 2 and 3 are quite similar. However, a larger negative peak is predicted with Grid 2 because the aft surface of Grid 2 surface is farther away from the blade trailing edge and can capture more of the shock wave effects. The Grid 1 predictions are the least accurate, owing to the larger distance from the blade surface and therefore greater numerical dissipation of the aerodynamic input.

For the permeable surface method, Figure 4.13 shows the prediction comparisons at Microphone 1. It is clearly seen that the permeable surface method can not only capture the high negative peak due to the shock wave interaction, but can also capture a good deal of the noise due to the vortex interaction. Figure 4.14 shows the comparisons for Microphone 7 predictions.

Here, the predictions for the permeable surface method are much better than those obtained with the impermeable surface method, as the noise due to the vortex interactions is also captured.

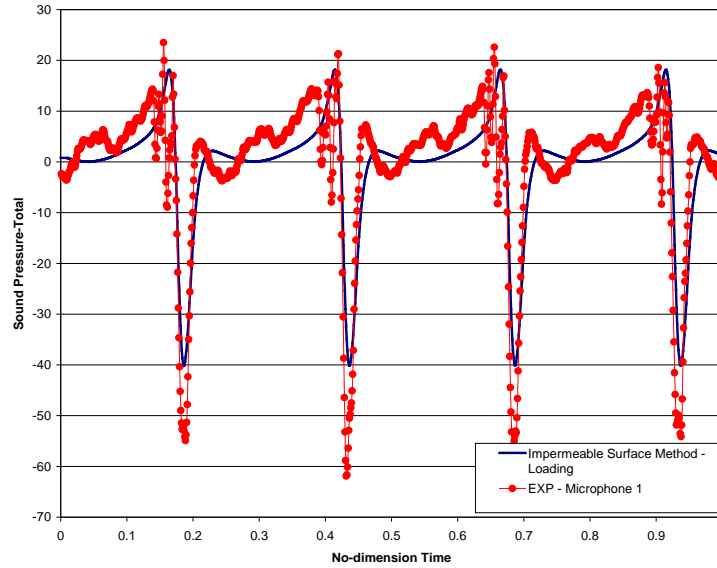


Figure 4.5 The Sound Pressure Comparison for Microphone 1 (Compact Patch Method)

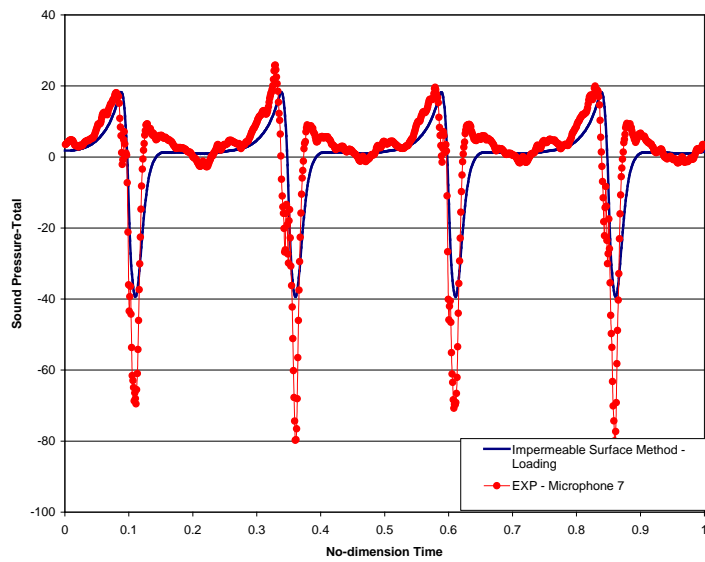


Figure 4.6 The Sound Pressure Comparison for Microphone 7 (Compact Patch Method)

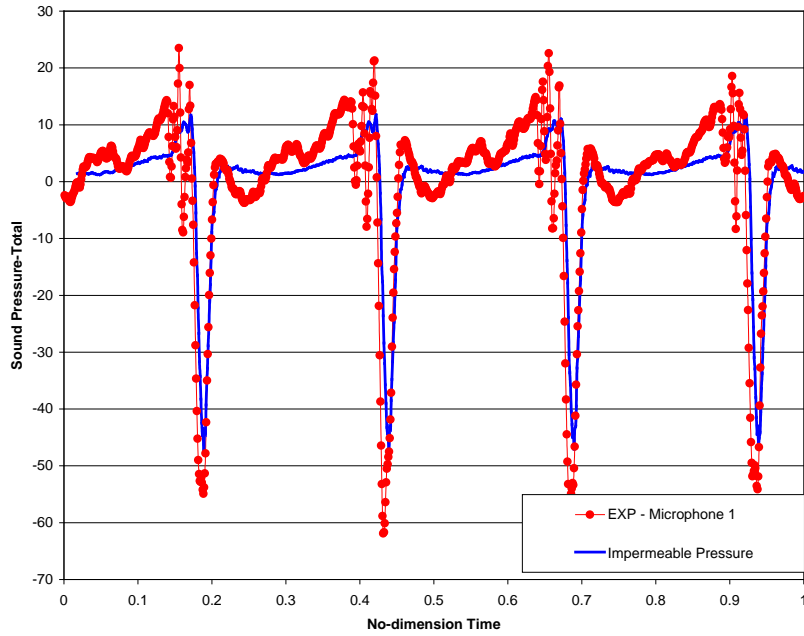


Figure 4.7 The Sound Pressure Comparison for Microphone 1
(Impermeable Surface method with **Surface Pressure as Input**)

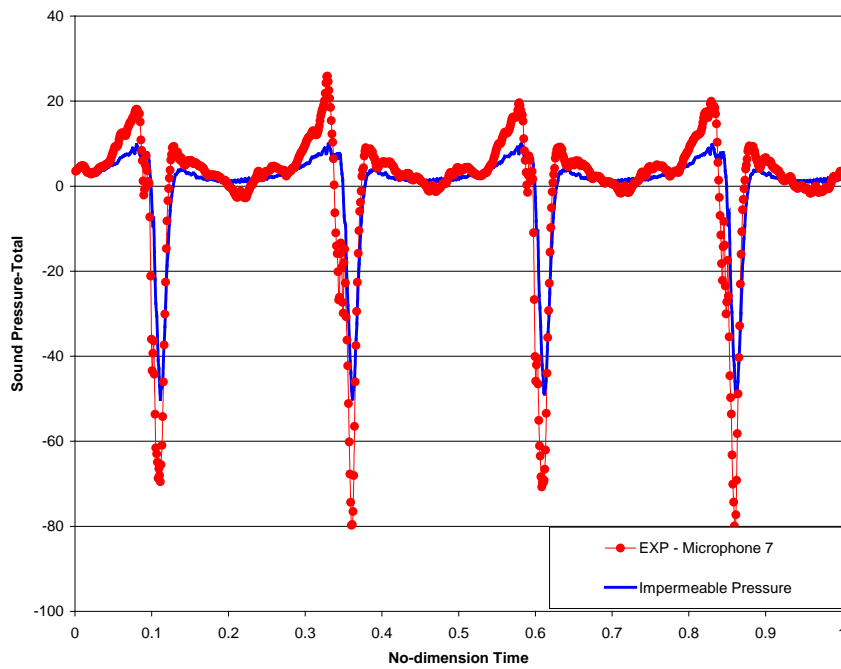


Figure 4.8 The Sound Pressure Comparison for Microphone 7
(Impermeable Surface method with **Surface Pressure as Input**)

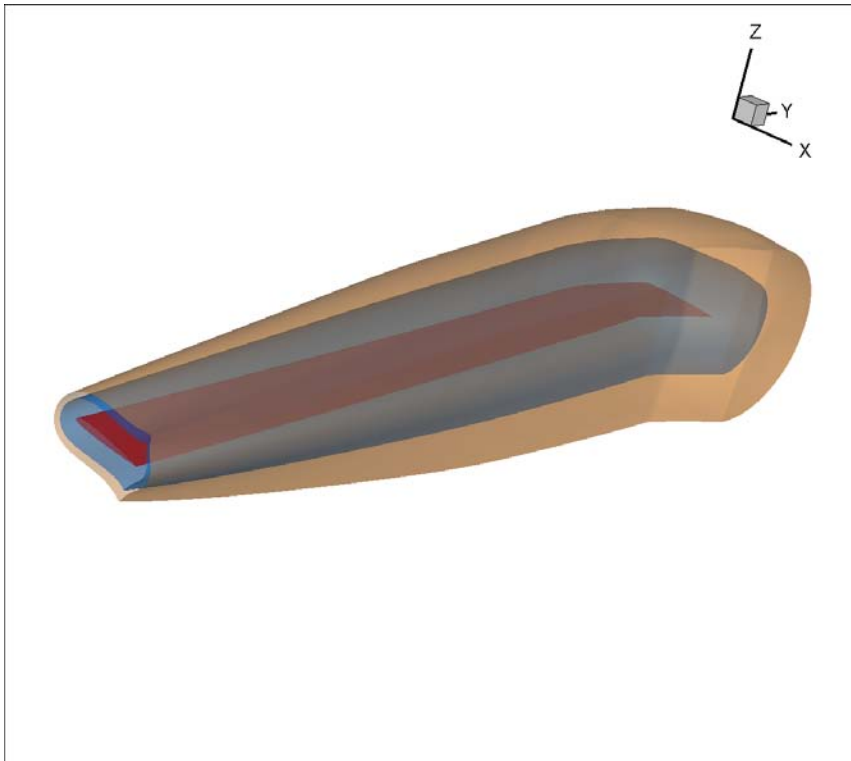


Figure 4.9 Acoustic Data Surface (Baseline-Grid vs. Grid 1)
 (Red – Blade; Blue – Baseline Grid; Yellow – Grid 1)

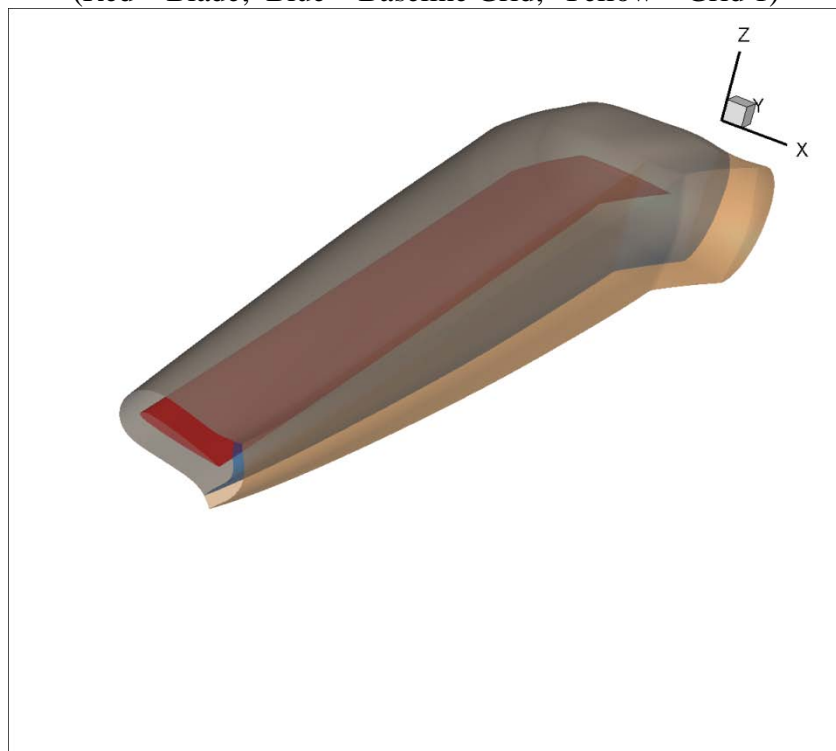


Figure 4.10 Acoustic Data Surface (Baseline-Grid vs. Grid 2)
 (Red – Blade; Blue – Baseline Grid; Yellow – Grid 2)

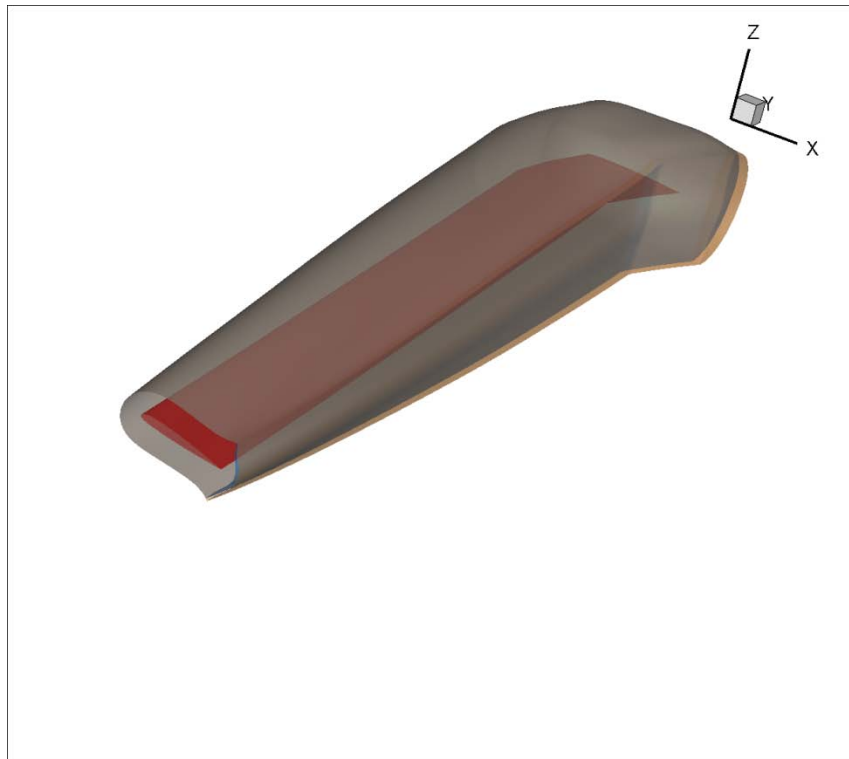


Figure 4.11 Acoustic Data Surface (Baseline-Grid vs. Grid 3)
 (Red – Blade; Blue – Baseline Grid; Yellow – Grid 3)

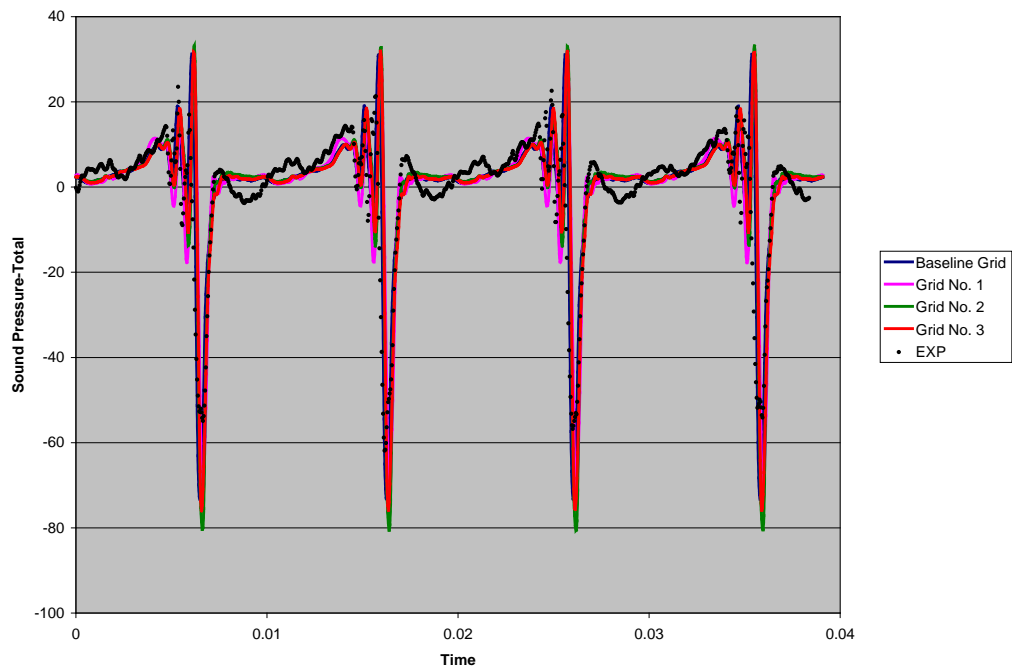


Figure 4.12 WOPWOP3 Predictions for Different Acoustic Surface Grids

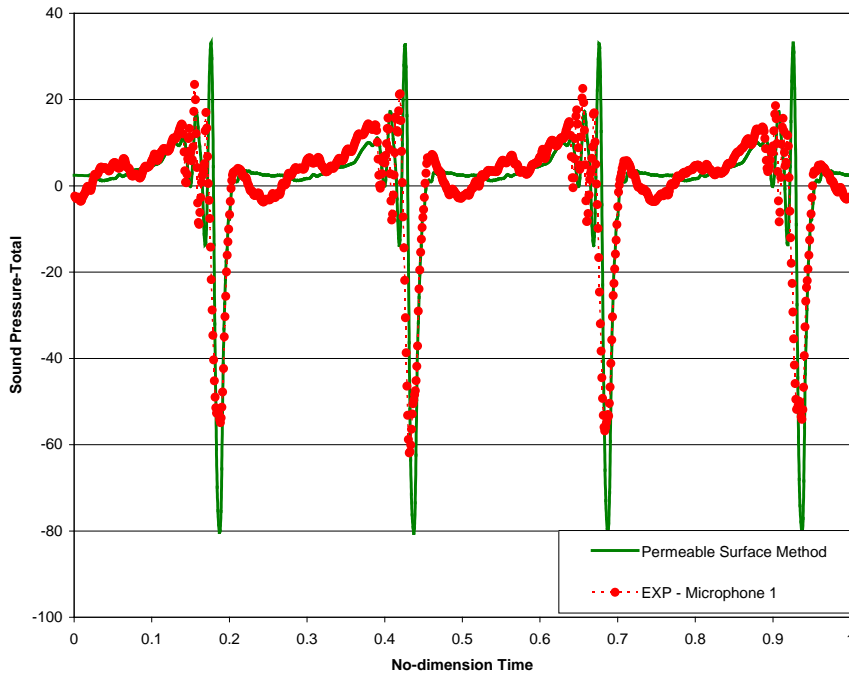


Figure 4.13 The Sound Pressure Comparison for Microphone 1
(Permeable Surface Method)

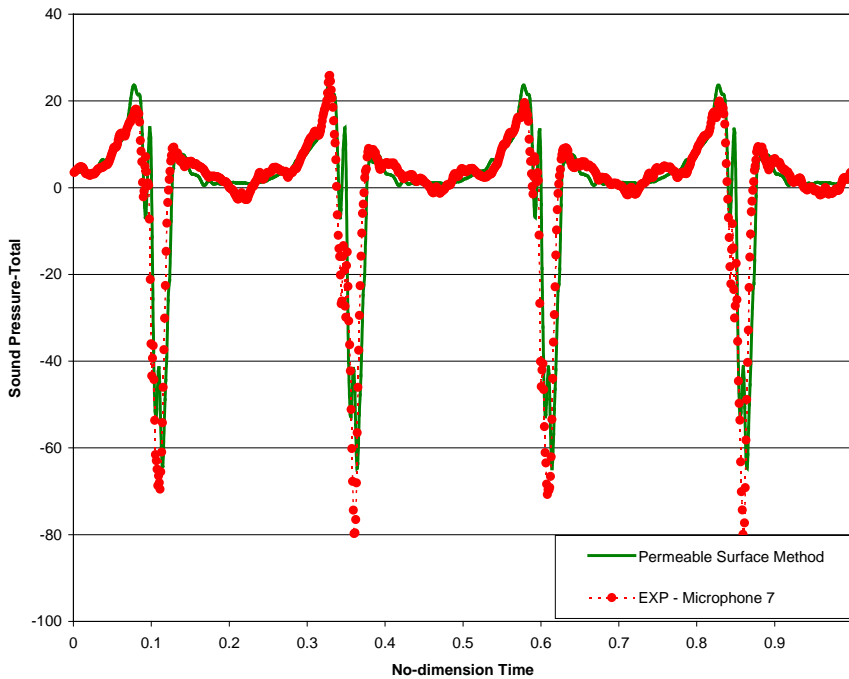


Figure 4.14 The Sound Pressure Comparison for Microphone 7
(Permeable Surface Method)

4.2 HART II BVI Noise Prediction with Impermeable Surface Method

The aerodynamic parameters on the blade surface predicted with the above methods (CFD+Overset grid, CFD+Free-wake method and CFD+PVTM) were used to obtain the acoustic signature on a microphone plane below the rotor disk. Because the BVI noise is mostly generated by the blade surface pressure variation, the impermeable surface method was used to predict the acoustic signature on the microphone plane. As mentioned above, there are two different approaches available in WOPWOP3 for specifying the blade loading for the impermeable surface method. One uses the surface loading compact patch, while the other uses the surface pressure directly. Both of these methods were investigated to check the accuracy of the acoustic predictions.

Figure 4.15 shows the BVI SPL contour from the experiment [4.5], where the two BVI noise peaks on the advancing side and retrieving side are clearly observed. The microphone plane in the experiment, located 2.215 meter below the rotor disk with an area of 8 meter * 5.4 meter, is also presented here.

Figure 4.16 shows the BVI SPL contours from the CFD+Overset Grid method, where 4.16(a) is the acoustic signature obtained using compact patches and (b) is from the pressure. As shown in these figures, the BVI noise predicted with the overset grid method does not generally agree well with the measured data, due at least in part to insufficient grid resolution. Also, the maximum noise predicted with the compact patches is well below the levels obtained using the surface pressure. This indicates that the compact patch method may not be optimal in this case.

Figure 4.17 shows the contours from the CFD+Free-wake method, where the noise peak location also differs from that seen in the experiment. As shown in Figure 4.17(b), two maximum BVI noise peaks are predicted by the CFD+Free-wake method. However, the directivity (*i.e.*, locations of the maximum noise levels) differs from the experiment measurements. Additionally, the predicted maximum BVI noise levels are also lower than the experimental values.

Figure 4.18 shows the contours from the CFD+PVTM method with a low resolution wake. Again, the acoustic prediction using the compact patch approach does not compare well with measured levels as seen in Figure 3.18(a). However, using the surface pressure produces predicted BVI SPL contours that compare much more favorably with measurement for both the

maximum noise level and location on the advancing and retrieving side. Direct comparison with the measured contours is shown in Figure 3.19 for further clarification.

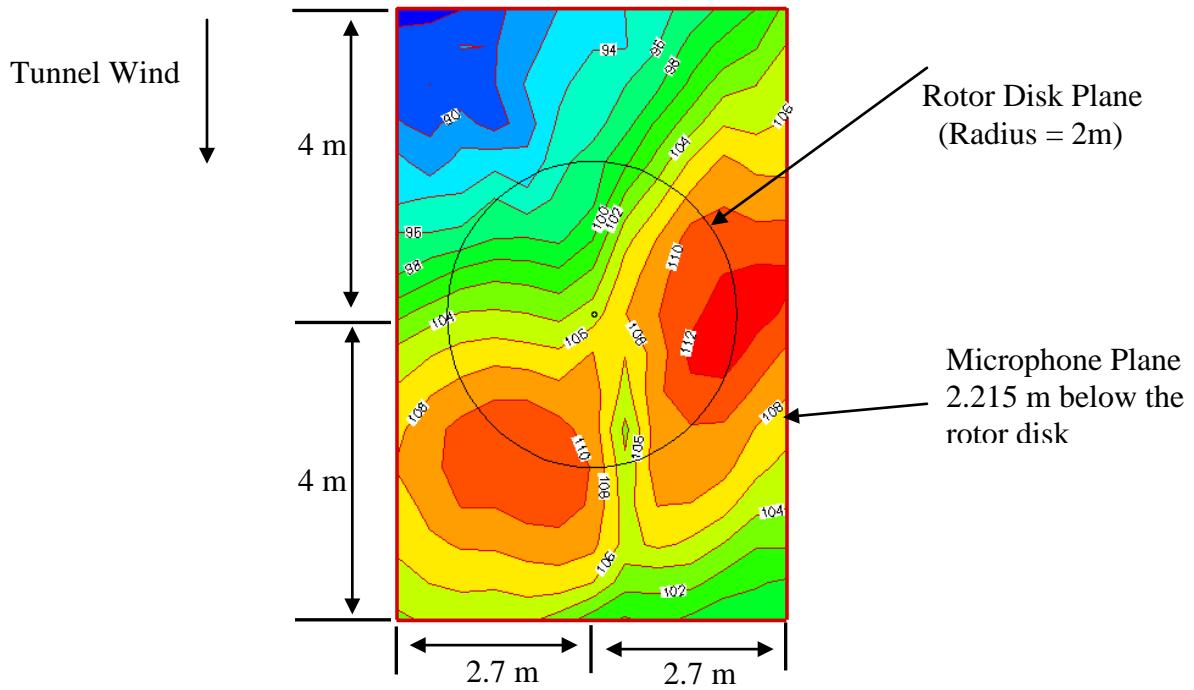
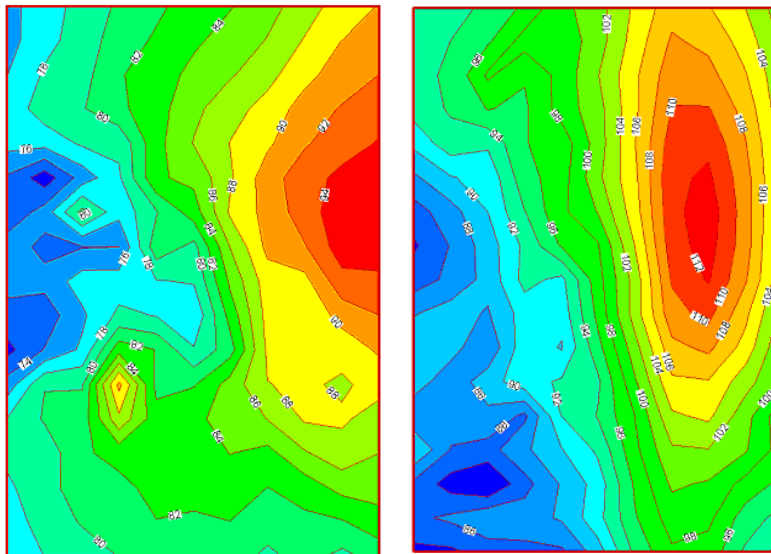


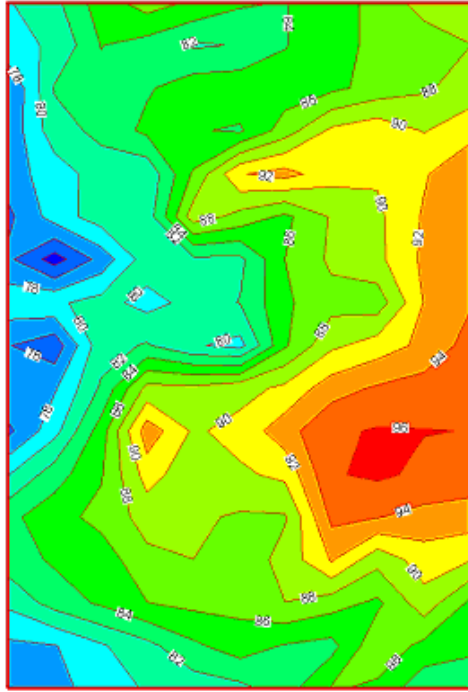
Figure 4.15 Experiment BVI SPL Contour



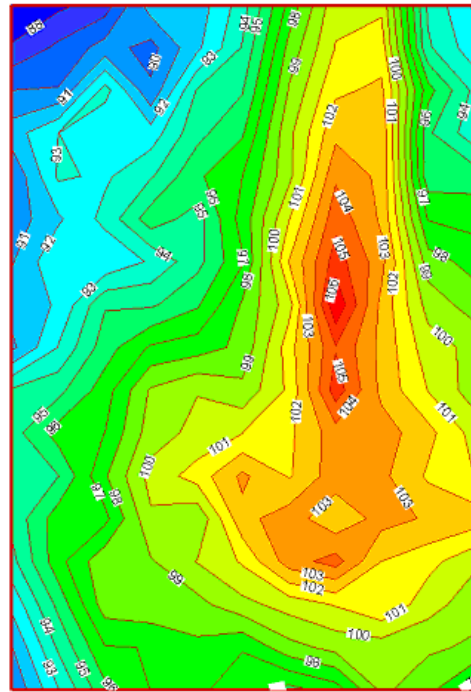
(a) Loading

(b) Pressure

Figure 4.16 BVI SPL Contour with CFD+Overset Grid Method

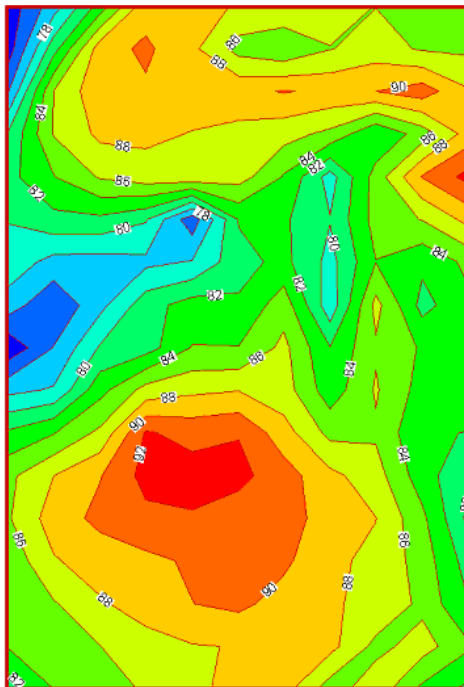


(a) Loading

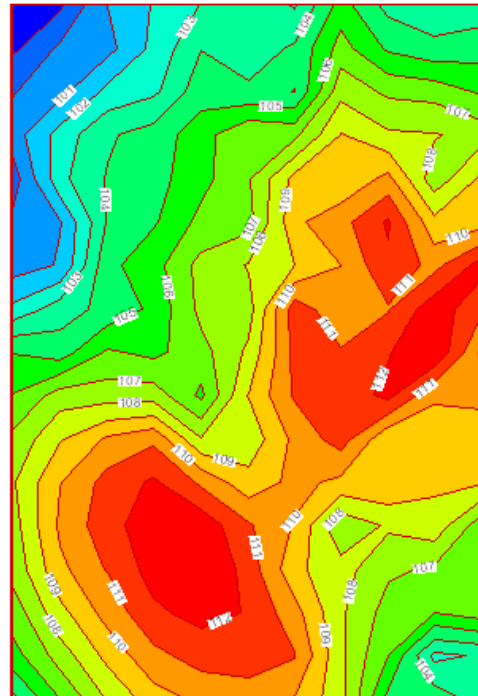


(b) Pressure

Figure 4.17 BVI SPL Contour with CFD+Free-wake Method

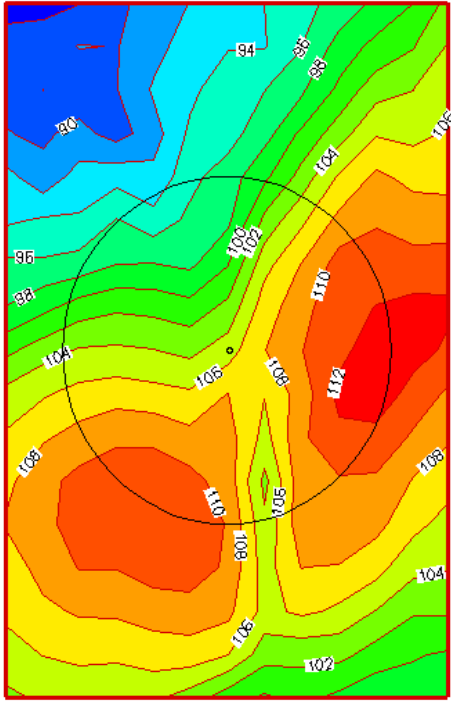


(a) Loading

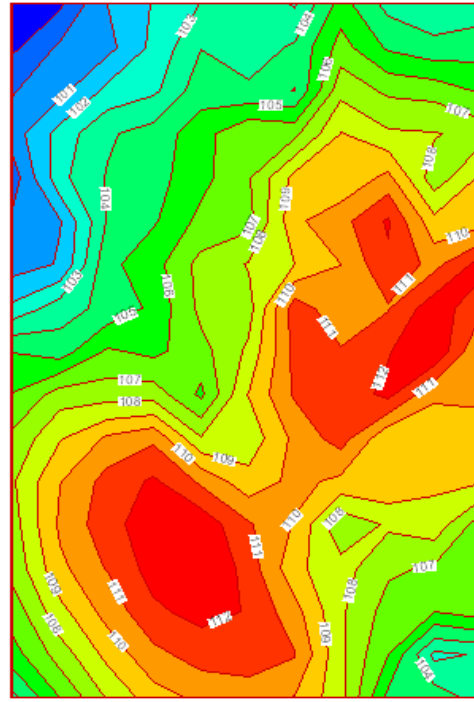


(b) Pressure

Figure 4.18 BVI SPL Contour with CFD+PVTM Low Resolution Wake



(a) Experiments



(b) PVTM_Low_Resolution_Wake

Figure 4.19 BVI SPL Contours Comparison with PVTM Method

Chapter V

Concluding Remarks

This report summarizes the development and validation of a physics-based, high-fidelity, multi-disciplinary tool (MUTE) for accurate and efficient rotorcraft source noise predictions. The MUTE tool uses a systematic coupling of approaches from multiple disciplines. Namely, Computational Fluid Dynamics with high-order near body algorithm (STVD 6), a high-fidelity wake modeling method (PVTM), Computational Structural Dynamics with feedbacks of the rotor blade deformation information and rotorcraft trim solutions, and high-fidelity acoustic propagation analysis are incorporated. This coupled CFD/CSD/Acoustic procedure is very flexible and controlled by a Python script, so that these CFD, CSD or acoustic modules can be easily replaced with other similar codes. The blade loading and acoustic signature predictions from the MUTE tool are compared with several experimental data sets with a wide range of flight conditions.

Three wake modeling/capturing methods were implemented into the MUTE tool for different applications: the free-wake method, the overset grid CFD method, and the PVTM method. The rotor blade aerodynamic loading predictions from these wake modeling methods were validated against the UH60A, DNW and HART II experimental data under high-speed, low-speed, and BVI flight conditions. The results show that, in the absence of strong blade vortex interaction, all wake modeling methods produced reasonable blade loading predictions when the CFD was coupled with CSD to include the blade deformation information (*e.g.*, such as the UH60A level flight test cases).

Compared with the other wake modeling methods investigated, the free-wake method was the fastest for most of the high-speed and low-speed level flight simulations when the blade wake interaction was minimal. The CFD with overset-grid method would generally be the most robust method over the flight conditions considered. This would also be the case for the UH60a dynamic stall condition, provided the CFD background grid resolution was high enough to preserve the far wake traveling inside the computational zone. However, this would require considerably more computational resources. With the limited computational resources employed in this study, the PVTM method was the most efficient way to preserve the wake in the far-field

and accurately predict the rotor wake blade interactions. For the HART II BVI test case, only the PVTM method gave reasonable predictions at coarse resolution.

The acoustic predictions of the MUTE tool were also validated with the DNW high-speed noise experimental data and the HART II BVI noise data. In the acoustic analysis using WOPWOP 3, both the impermeable surface and permeable surface methods were implemented into the MUTE tool. The results show that, to capture the high-speed impulsive noise produced by the shock wave interaction, the permeable surface method gave much better predictions than the impermeable surface method. For the BVI noise prediction, the wake modeling method was very important for the accuracy of the noise predictions, and the PVTM method gave the best results for this case.

The accuracy of the noise prediction was greatly dependent on the accuracy of the blade loading and rotor wake simulation results. Compared to the very fine grid resolution requirements of the CFD overset grid method, the PVTM method has more potential in accurately modeling the rotor blade and wake interactions with reasonable computational resource requirements. Improvements of the PVTM computational efficiency may significantly improve the correlations and further reduce the computational costs in the future.

References

Chapter II

- [2.1] Srinivasan, G. R., and Baeder, J. D., "TURNS: A Free-wake Euler/Navier-Stokes Numerical Method for Helicopter Rotors," AIAA Journal Vol. 31, No. 5, 1993, pp. 959-962.
- [2.2] Johnson, W., "Rotorcraft Aerodynamic Models for a Comprehensive Analysis," Proceedings of the American Helicopter Society Annual Forum, Washington DC, 1998.
- [2.3] Anusonti-Inthra, P., "Developments and Validations of Fully Coupled CFD and Particle Vortex Transport Method for High-Fidelity Wake Modeling in Fixed and Rotary Wing Applications," NASA CR-2010-21669.
- [2.4] Lee, S., Brentner, K. S., Hennes, C. C., Flynt, B. T., Theron, J. N., and Duque, E. P. N., "Investigation of the Accuracy Requirements for Permeable Surfaces Used in Rotor Noise Prediction," Proceeding of American Helicopter Society 62nd Forum, Phoenix, AZ, May, 2006.
- [2.5] Roe, P. L. "Approximate Riemann Solvers, Parameter Vectors and Difference Schemes," J. of Computational Physics, vol. 42, pp. 357-372, 1981
- [2.6] Van Leer, B. "Towards the Ultimate Conservation Difference Scheme, V: A Second-Order Sequel to Godunov's Method," J. of Computational Physics, vol. 32, pp. 101-136, 1979.
- [2.7] Jiang, G., and Shu, C.-W., "Efficient Implementation of Weighted ENO Schemes," J. of Computational Physics, vol.126, pp202-228, 1996
- [2.8] Yee, H. C., Sandham, S. D., and Djomehri, M. J., "Low Dissipative High-order Shock-capturing Method Using Characteristic Based Filters," J. of Computational Physics, vol. 150, pp.199-238, 1999.
- [2.9] Lorber, P. F., "Aerodynamic Results of a Pressure-Instrumented Model Rotor Test at the DNW," *Journal of the American Helicopter Society*, Vol. 36, No. 4, 1991, pp. 66-76.
- [2.10] Lorber, P. F., Stauter, R. C., and Landgrebe, A. J., "A Comprehensive Hover test of the Airloads and Airflow of an Extensively Instrumented Model Helicopter Rotor," American Helicopter Society 45th Annual Forum, Boston, MA, May, 1989.

Chapter III

- [3.1] Brown, R. E., “Rotor Wake Modeling for Flight Dynamic Simulation of Helicopters,” *AIAA Journal*, Vol. 38, No. 1, pp.57-63, 2000.
- [3.2] Anusonti-Inthra, P. “Validations of Coupled CSD/CFD and Particle Vortex Transport Method for Rotorcraft Applications: Hover, Transition, and High Speed Flights” Proc. 66th AHS Forum, Phoenix, AZ, 2010.
- [3.3] van der Wall, B. G., Junker, B., Burley, C. L., Brooks, T. F., Yu, Y., Tung, C., Raffel, M., Richard, H., Wagner, W., Mercker, E., Pengel, K., Holthusem, H., Beaumier, P., and Delrieux, Y., “The HART II Test in the LLF of DNW – a Major Step towards Rotor Wake Understandings,” 28th European Rotorcraft Forum, Bristol, England, 2002.

Chapter IV

- [4.1] Brentner, K. S., Perez, G., Bres, G. A., and Jones, H. E., “Maneuvering Rotorcraft Noise Predictions,” *Journal of Sound and Vibration*, Vol. 39, No. 3-5, August, 2003, pp. 719-738.
- [4.2] Farassat, F. and Succi, G. P., “The Prediction of Helicopter Discrete Frequency Noise,” *Vertica*, Vol. 7, No. 4, 1983, pp. 309-320.
- [4.3] Ffowcs Williams, J. E., and Hawkings, D. L., “Sound Generated by Turbulence and Surfaces in Arbitrary Motion,” *Philosophical Transactions of the Royal Society*, Vol. A264, No. 1151, 1969, pp. 321-342.
- [4.4] Visintainer, J. A., Marcolini, M. A., Burley, C. L., and Liu, S. R., “Acoustic Predictions Using Measured Pressure from a Model Rotor in the DNW,” *Journal of American Helicopter Society*, Vol. 38, No. 3, 1993, pp.35-44.
- [4.5] Boyd, D. D., Burley, C. L., and Conner, D. A., “Full Scale Rotor Acoustic Predictions and the Link to Model Scale Rotor Data,” AHS 4th Decennial Specialist’s conference on Aeromechanics, San Francisco, CA, Jan. 2004.

REPORT DOCUMENTATION PAGE

*Form Approved
OMB No. 0704-0188*

The public reporting burden for this collection of information is estimated to average 1 hour per response, including the time for reviewing instructions, searching existing data sources, gathering and maintaining the data needed, and completing and reviewing the collection of information. Send comments regarding this burden estimate or any other aspect of this collection of information, including suggestions for reducing this burden, to Department of Defense, Washington Headquarters Services, Directorate for Information Operations and Reports (0704-0188), 1215 Jefferson Davis Highway, Suite 1204, Arlington, VA 22202-4302. Respondents should be aware that notwithstanding any other provision of law, no person shall be subject to any penalty for failing to comply with a collection of information if it does not display a currently valid OMB control number.
PLEASE DO NOT RETURN YOUR FORM TO THE ABOVE ADDRESS.

1. REPORT DATE (DD-MM-YYYY) 01-02-2011			2. REPORT TYPE Contractor Report		3. DATES COVERED (From - To) February 2007 - April 2010	
4. TITLE AND SUBTITLE Development and Validation of a Multidisciplinary Tool for Accurate and Efficient Rotorcraft Noise Prediction (MUTE)					5a. CONTRACT NUMBER NNL07AA31C	
					5b. GRANT NUMBER	
					5c. PROGRAM ELEMENT NUMBER	
6. AUTHOR(S) Liu, Yi; Anusonti-Inthra, Phuriwat; Diskin, Boris					5d. PROJECT NUMBER	
					5e. TASK NUMBER	
					5f. WORK UNIT NUMBER 877868.02.07.07.04.01	
7. PERFORMING ORGANIZATION NAME(S) AND ADDRESS(ES) NASA Langley Research Center Hampton, VA 23681-2199				8. PERFORMING ORGANIZATION REPORT NUMBER		
9. SPONSORING/MONITORING AGENCY NAME(S) AND ADDRESS(ES) National Institute of Aerospace 100 Exploration Way Hampton, VA 23666				10. SPONSOR/MONITOR'S ACRONYM(S) NASA		
				11. SPONSOR/MONITOR'S REPORT NUMBER(S) NASA/CR-2011-217057		
12. DISTRIBUTION/AVAILABILITY STATEMENT Unclassified - Unlimited Subject Category 71 Availability: NASA CASI (443) 757-5802						
13. SUPPLEMENTARY NOTES Langley Technical Monitor: Douglas M. Nark						
14. ABSTRACT A physics-based, systematically coupled, multidisciplinary prediction tool (MUTE) for rotorcraft noise is developed and validated with a wide range of flight configurations and conditions. MUTE is an aggregation of Computational Fluid Dynamics (CFD), Computational Structural Dynamics (CSD), and high-fidelity acoustics tools. Predictions of the blade-vortex interaction noise in low speed flight are also improved by using the Particle Vortex Transport Method (PVTM), which preserves the wake flow details required for blade/wake and fuselage/wake interactions. The accuracy of the source noise prediction is further improved by utilizing a coupling approach between CFD and CSD, so that the effects of key structural dynamics, elastic blade deformations, and trim solutions are correctly represented in the analysis. The blade loading information and/or flow field parameters around the rotor blade predicted by the CFD/CSD coupling approach are used to obtain the acoustic signatures at far-field observer locations. Blade aerodynamic loadings and far-field acoustic predictions are compared and validated with a variation of experimental data sets.						
15. SUBJECT TERMS Computational fluid dynamics; Computational structural dynamics; Particle Vortex Transport Method; Rotary wing aircraft; Acoustics; Noise prediction; Blade-vortex interaction						
16. SECURITY CLASSIFICATION OF:			17. LIMITATION OF ABSTRACT	18. NUMBER OF PAGES	19a. NAME OF RESPONSIBLE PERSON	
a. REPORT	b. ABSTRACT	c. THIS PAGE			STI Help Desk (email: help@sti.nasa.gov)	
U	U	U	UU	74	19b. TELEPHONE NUMBER (Include area code) (443) 757-5802	